UNIVERSITY OF AGDER

Stabilization of Hydraulically Actuated Boom Using Pressure Feedback

- Theoretical and Experimental Investigation

CONFIDENTIAL

Thomas Børseth
Christian Høgeli Solvik

Supervisor:
Morten Kjeld Ebbesen

University of Agder, 2015
Faculty of Engineering and Science
Department of Engineering Sciences

Abstract

In hydraulic systems pressure compensated proportional control valves is often used as they serve a flow that is independent to the load and proportional to the valve opening. However, combining a pressure compensated valve with counterbalance valves, which is a necessary safety in systems with heavy suspending loads, is well known to be oscillatory by nature for negative loads. In this thesis a method for stabilizing the system using pressure feedback is investigated.

A hydraulically actuated boom has been designed by the project supervisors and build to test the method. A simulation model of the test rig is made on the basis on analytic equations for the hydraulic and mechanical system, where the boom is modeled as a lumped model making it flexible for more realistic simulations. Furthermore, the simulation model is verified by comparison of simulation results to the physical test rig results.

Stability analysis proofs the instability in the uncompensated system. Using a high pass filtered pressure feedback the system is proven stable analytically for a linear system, numeric for a dynamic system and by testing on the physical model. The tests from the physical rig gave the best results by choosing a filter frequency around the natural frequency of the system, without compromising the cylinder velocity.

Preface

This Master's Thesis is written as a part of the Master's Programme in Mechatronics at the University of Agder. The thesis represents the end of a five year long education that we have carried out at the university. During this thesis we have been working with many of the interesting disciplines in the field of mechatronics.

We would like to thank the staff at the university for guiding us through the challenges during the last five years. We would also like to thank the staff at the university's workshop for assistance during the assembly of the test rig used in this project. We are grateful for the support and guidance from our supervisor, Associate Professor Morten Kjeld Ebbesen.

Thomas Børseth

Christian Høgeli Solvik

Grimstad, May 20, 2015

Contents

Nomenclature

Parameters are constant values, e.g. values found in data sheets, gravitational acceleration etc.
Variables are calculated values (which can be constant).

List of Parameters

Parameter	Description	Value	Unit
b_1	Distance between the center of the joint and the inner end of the lower beam	50	mm
b_2	Distance between the end of the lower mounting bracket and the bolt hole	76	mm
b_3	Distance between the bottom of the lower mounting bracket and the bolt hole	58	mm
b_4	Distance between the end of the upper mounting bracket and the bolt hole	76	mm
b_5	Distance between the bottom of the upper mounting bracket and the bolt hole	58	mm
b_6	Distance between the center of the joint and the bottom of the upper beam	75	mm
b_7	Distance between the center of the joint and the inner end the upper beam	80	mm
b_8	Distance between the center of the joint and the top of the lower beam	1115	mm
$C_{p,Bak}$	Bak's pressure friction coefficient	0.02	[-]
C_v	Viscous friction coefficient	4.06	$\frac{\mathrm{Ns}}{\mathrm{mm}}$
d_c	Diameter cylinder	65	mm
d_r	Diameter cylinder rod	35	mm
E	Young's modulus	210,000	MPa
g	Gravitational acceleration	9.807	$\frac{\mathrm{m}}{\mathrm{s}^2}$
h_{arm}	Height of arm	150	mm
l_{arm}	Length of arm	3680	mm
l_1	Distance between inner end of upper beam and inner end of upper mounting bracket	548	mm
l_2	Distance between inner end of lower beam and inner end of lower mounting bracket	410	mm
m_{arm}	Mass of arm	81	kg
m_{plfix}	Mass of payload fixture	7.5	kg

$m_{pl1...4}$	Mass of payload plate 1 to 4	76	kg
m_{pl5}	Mass of payload plate 5 (end plate)	16	kg
m_{rod}	Mass of the cylinder rod and piston	5	kg
p_{pcv}	Pressure compensator spring pressure	7	bar
p_s	Supply pressure	155	bar
$p_{fo,cv}$	Pressure needed to overcome static friction	1	bar
$p_{fc,cbv}$	Fully closed spring pressure load holding valve	350	bar
p_T	Tank pressure	0	bar
s_c	Cylinder stroke	500	mm
t_{arm}	Thickness of arm	6	mm
t_{pl}	Thickness of payload plates	50	mm
v_0	Stribeck velocity	14.19	$\frac{\text{mm}}{\text{s}}$
V_{CH1}	Dead volume cylinder side chamber	50	cm^3
V_{CH2}	Dead volume rod side chamber	50	cm^3
V_{L1}	Volume between pressure compensator and main spool	2	cm^3
V_{L2}	Volume line 2	100	cm^3
V_{L3}	Volume line 3	150	cm^3
V_{L4}	Volume line 4	200	cm^3
β	Oil stiffness	1300	MPa
μ_p	CBV pilot area	[1, 2, 3, 5]	[-]

List of Variables

Variable	**Description**	**Unit**
A	Area	mm^2
a	Acceleration	$\frac{\text{m}}{\text{s}^2}$
D	Diameter	mm
F_1	Force generated from the pressure in chamber 1	N
F_2	Force generated from the pressure in chamber 2	N
F_C	Coulomb friction	N
F_{fr}	Frictional force	N
F_L	Load force acting on cylinder	N
F_S	Static friction	N
G	Gravitational force	N
G_{rod}	Gravitational force of the cylinder rod and piston	N
l_{cyl}	Length of the cylinder	mm
m_{eff}	Effective mass	kg
m_{pl}	Total mass of payloads	kg
$p_{1...4}$	Line pressure	bar
p_{set}	Set pressure counterbalance valve spring	bar
Q	Volumetric flow	l/min
R	Reaction force	N
R_{Cho}	Gas to volume ratio in fluid	[-]
v_c	Piston velocity relative to cylinder	$\frac{\text{m}}{\text{s}}$
V	Volume at point of interest	m^3

V_0	Volume at atmospheric pressure 1	m^3
V_1	Initial volume	m^3
w_1	Length of the upper side in the test rig's vector triangle	mm
w_2	Length of the inner side in the test rig's vector triangle	mm
α_1	Angle in the test rig's vector triangle	rad
δ	Deflection of the container	mm
μ_c	Cylinder/rod area ratio	[-]
$\theta_{1,2}$	Angle in the test rig's vector triangle	rad
$\varphi_{1,2}$	Angle in the test rig's vector triangle	rad
ω	Natural frequency	$\frac{rad}{s}$

Chapter 1

Introduction

The history of hydraulic systems dates back thousands of years BC to when the first water channel was built by farmers for irrigation purposes. Today, the usage of hydraulic systems span over a wide range; from simple lifting devices to complex systems used in offshore drilling applications. One of the main advantages of hydraulics is the high power density compared to e.g. electrical systems. Another advantage is that the hydraulic fluid itself both transfers heat and lubricates mechanical parts. A disadvantage of hydraulics is that the system design might become complex, including the fact that introduction of counterbalance valves, e.g. for load holding applications, may lead to instability.

1.1 Background and Motivation

A popular way to ease the control design of hydraulic systems is to use pressure compensated proportional directional control valves to control the flows in the system. Such valves ensures a flow that is both load independent and linearly dependent of the input signal to the valve spool. This makes the control design relatively easy in comparison with creating a control system that takes hand of the non-linearities caused by the pressure dependency of the flow. The other side of the coin is that instability caused by counterbalance valves is especially prominent in systems that also are pressure compensated.

A sophisticated way of solving the instability problem for manufacturers of hydraulic valves or complete system manufacturers could be to create an internal compensation system. By doing this, the designer of the control system for the entire the system, consisting of e.g. multiple machines, would not need to concern about the instability caused by the combination of counterbalance valves and pressure compensation.

The internal compensation system could consist of e.g. a physical hydraulic circuit or an electronic control system. Drawbacks with the first approach might be reduced system response, added complexity and added cost to the hydraulic system. A drawback with the latter is that the effect of the simplification in the control system gained by the use pressure compensated valves is reduced due to required compensation of the instability.

1.2 Problem Statement

In hydraulic systems counterbalance valves are commonly used. Such valves serves several purposes such as no load drop before lift, load holding for safety reasons in case of hose rupture and prevention of cavitation. Unfortunately, counterbalance valves tends to introduce instability when handling negative loads. The instability is especially prominent if counterbalance valves are combined with pressure compensated flow control. Such flow control are widely used because it eases the control of the hydraulic system. The pressure compensation makes the flow load independent, which means that an operator of a crane do not have to take the load into account when controlling the velocity of a lifting operation. Obviously, a combination of counterbalance valves and pressure compensated flow control is often desired, but many times impeded by the instability issue. The purpose of this thesis is therefore to design an electronic control system

which compensates for the instability, thus allowing the combination of counterbalance valves and pressure compensated flow control in hydraulic systems. A stabilizing method proposed by the project supervisors should be investigated. The method is to compensate for the instability by controlling the directional control valve using pressure feedback.

1.3 Literature Review

As there are few research papers to be found on the subject, the literature review is based on the paper *Controlling a Negative Loaded Hydraulic Cylinder Using Pressure Feedback* [1] written by one of the project supervisors, Michael R. Hansen (and Torben O. Andersen). The paper investigates the subject both analytically and numerically. The proposed method in the paper is using a high pass filtered pressure feedback. Results show that the filter frequency should be chosen in accordance with the bandwidth of the valve. A low bandwidth valve requires a high filter frequency, while a high bandwidth valve yields the best results using a lower filter frequency.

1.4 Problem Solution

A theoretical and experimental investigation of an electronic control system compensating for instability introduced by the combination of pressure compensation and counterbalance valve is to be performed. A stabilizing method proposed by the project supervisors is investigated. The method proposed is to compensate for the instability by controlling a pressure compensated proportional directional control valve using pressure feedback. A physical test rig has been designed by the project supervisors with the goal of provoking the mentioned instability. The test rig consists of a boom actuated by a double acting asymmetric hydraulic cylinder, a directional control valve, a counterbalance valve and a variety of sensors. An illustration of the test rid is shown in Figure 1.1.

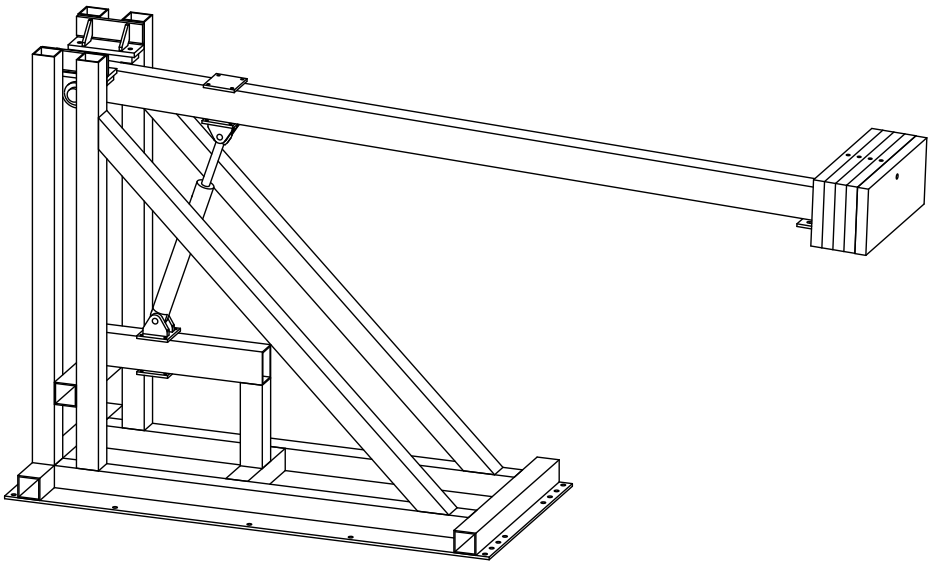

Figure 1.1: Test rig designed by project supervisors

A simulation model of the system including a flexible boom is to be made and verified by comparing results to analytic expressions and test data from the physical test rig. The stability is evaluated both for the uncompensated and compensated system. The compensation method is then tested and tuned on the simulation model before implementing it to the physical test rig.

1.5 Report Outline

In chapter 2 analytic models are made for the mechanical and hydraulic system. A stability analysis of a linear system is performed.

In chapter 3 a simulation model of the system is created. The analytic models are used to make a preliminary verification of the simulation model.

In chapter 4 the experimental set-up of the test rig is described and vital components are listed.

In chapter 5 tests are performed on the physical test rig for parameter identification and the final verification of the simulation model.

In chapter 6 the stabilizing method proposed is investigated analytically for the linearized system and numerically using the simulation model.

In chapter 7 the stabilizing method is tested on the physical test rig and the results from the test are viewed.

In chapter 8 the results of the experiments performed on the test rig are discussed.

Chapter 2

Theoretical Background

For making a good simulation model the theory behind the model is essential. Mathematical models of the system are used directly into the simulation program or as a verification of the simulations. The theoretical part is divided into mechanical system, hydraulic system and stability analysis of the system. The following points of assumptions and neglects for this chapter are made.

Assuming:

- Oil density is constant in mathematical model
- Constant bulk modulus of the fluid
- Oil type used to form characteristics in data sheets equal to the oil used in this experiment
- Turbulent flow in the system, laminar leakage flow
- Constant oil temperature
- Rig stiff

Neglecting:

- Geometry of the payload. Seen as a point mass.
- Leakage flow in pressure compensator and counterbalance valve

2.1 Mechanical System

Fluctuations in the mechanical system affects the hydraulic system, and therefore is a good simulation model of the boom needed in order to achieve a good model of the complete system.

Mathematical models describing the kinematics, kinetics and deflection of the boom are derived in this section, and later used to verify simulation models. The deflection itself is not essential for the project task, but it is used to verify the boom flexibility in the simulations. The flexibility in the simulations is modeled by a lumped boom model, which is described in the end of this section.

2.1.1 Kinematics

In order to be able to model the forces acting on the cylinder at varying cylinder length, the kinematics of the test rig has to be determined. Since the cylinder's mounting brackets are adjustable with respect to the positioning of the cylinder, it was found convenient to define the adjustable lengths from points which would make the measurements on the physical test rig easy. The two lengths are shown in Figure 2.1, where l_1 is the variable length from the end of the upper boom to the upper bracket, and l_2 is from the end of the lower beam to the lower bracket. l_{cyl} is the length of the cylinder and $b_{1...8}$ are constant lengths, e.g. dimensions of the brackets etc.

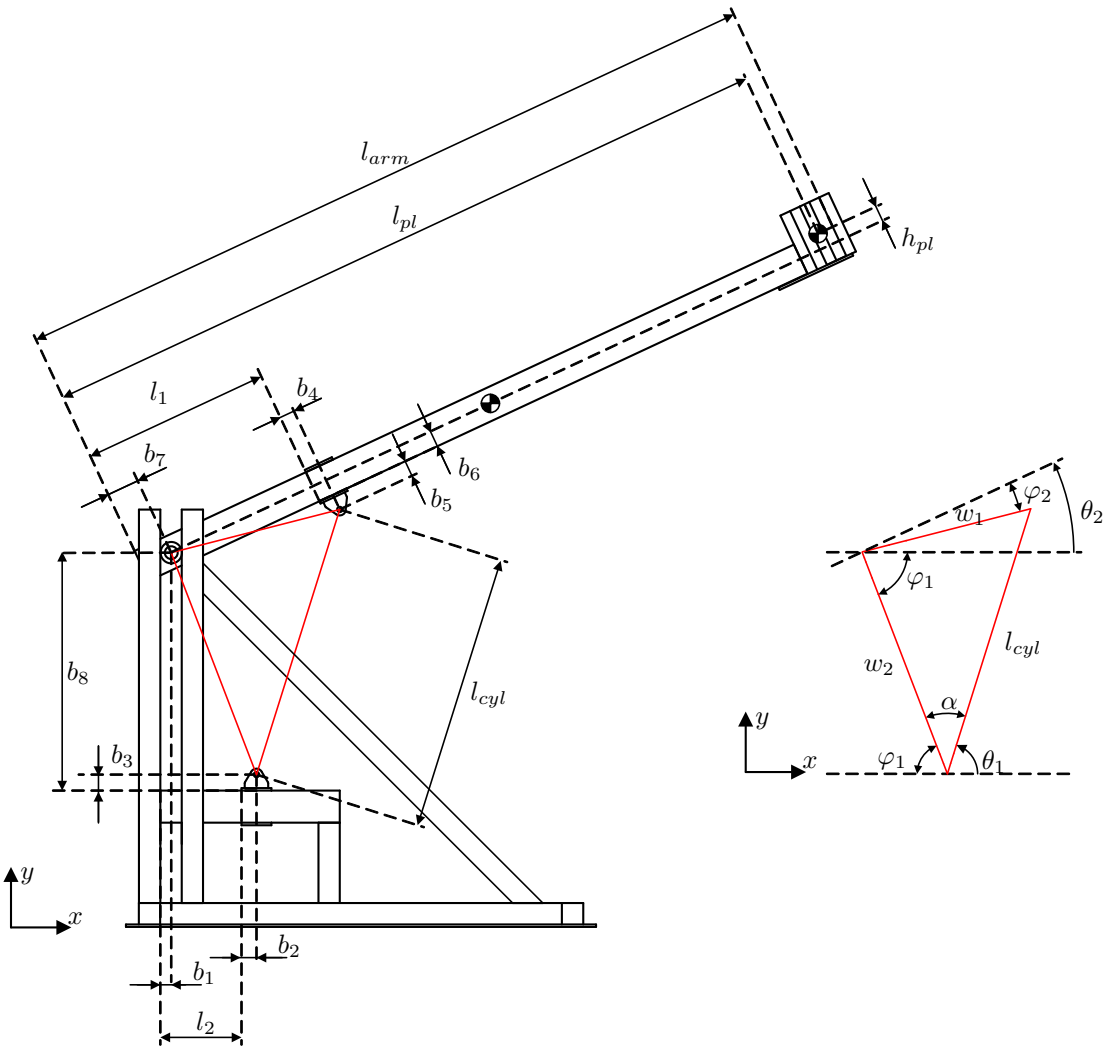

Figure 2.1: Illustration of the test rig

In this case one is interested in finding the angles of the cylinder, θ_1 , and the upper boom angle, θ_2 , with respect to the horizontal (x-axis) as functions of l_{cyl}, l_1 and l_2. Figure 2.1 shows the triangle formed by the rotational joint of the upper boom, and the cylinder mountings on both the upper boom and the lower beam. The lengths w_1 and w_2 depends on constant lengths ($b_{1...8}$) and l_1 and l_2 respectively, and are calculated using the Pythagorean theorem in equation (2.1) and equation (2.2). The angle α is calculated using the law of cosine in equation (2.3).

$$w_1 = \sqrt{(l_1 + b_4 - b_7)^2 + (b_5 + b_6)^2} \tag{2.1}$$

$$w_2 = \sqrt{(l_2 + b_2 - b_1)^2 + (b_8 - b_3)^2} \tag{2.2}$$

$$\alpha = \cos^{-1}\left(\frac{w_2^2 + l_{cyl}^2 - w_1^2}{2 \cdot w_2 \cdot l_{cyl}}\right) \tag{2.3}$$

$$\varphi_1 = \tan^{-1}\left(\frac{b_8 - b_3}{l_2 + b_2 - b_1}\right) \tag{2.4}$$

$$\varphi_2 = \tan^{-1}\left(\frac{b_5 + b_6}{l_1 + b_4 - b_7}\right) \tag{2.5}$$

$$\tag{2.6}$$

From the equations above, the cylinder angle θ_1 is computed.

$$\theta_1 = \pi - \varphi_1 - \alpha \tag{2.7}$$

The upper boom angle, θ_2, is found along with the coordinates of the common center of mass of the arm and payload by putting up kinematic constrains.

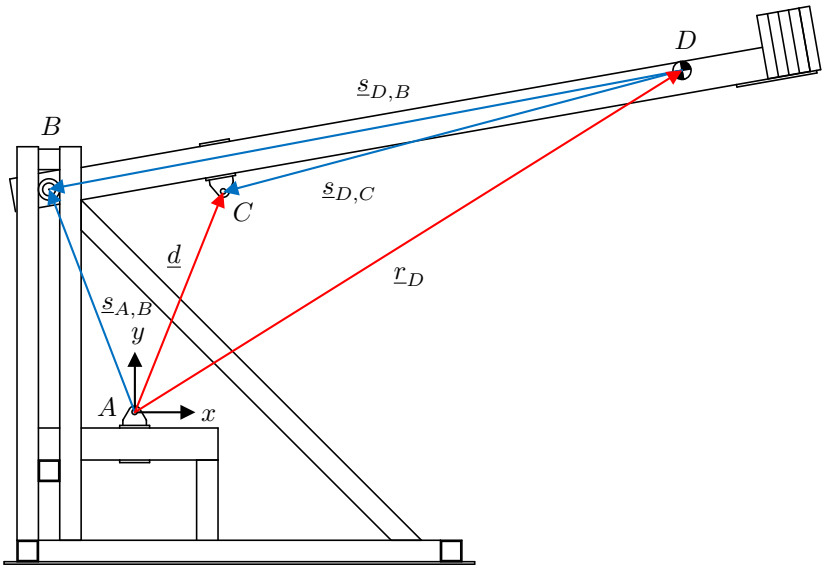

Figure 2.2: Rig with kinematic constraint vectors - *to compute the kinematics of the rigid boom*

$\underline{d}$: Global distance vector from point A to C
$\underline{r}_D$: Global distance vector from point A to center of mass in point D
$\underline{s}$: Global distance vectors with constant length

In Figure 2.2 vectors are drawn to describe the kinematic constraints. The arm and the payload is seen as one rigid body. Mass center of the body in point D is computed as the distance from the revolute joint (bearing) in point B.

$$\underline{e}_{cm} = \begin{bmatrix} e_{cm,x} \\ e_{cm,y} \end{bmatrix} = \frac{1}{m_D} \cdot \left(m_{arm} \cdot \begin{bmatrix} \frac{l_{arm}}{2} - b_7 \\ 0 \end{bmatrix} + m_{pl} \cdot \begin{bmatrix} l_{pl} - b_7 \\ h_{pl} \end{bmatrix} \right) \tag{2.8}$$

$\underline{e}_{cm}$: Distance vector from revolute joint to the center of mass in D
h_{pl} : Height from arm's center-line to payload's center of mass
l_{arm} : Length of arm
l_{pl} : Length between arm's back end and payload's center of mass
m_{arm} : Mass of arm
m_D : Mass of the entire body ($m_{arm} + m_{pl}$) with center of mass in D
m_{pl} : Mass of payload

The kinematic constraints for the revolute joint and the longitudinal drive (cylinder) are put up respectively.

$$\underline{\Phi}^{r,2} = \underline{r}_D + \underline{s}_{D,B} - \underline{s}_{A,B} = \underline{r}_D + \underline{A}_2 \cdot \underline{s}'_{D,B} - \underline{s}_{A,B} = \underline{0} \tag{2.9}$$

$$\Phi^{ld,1} = \underline{d}^T \cdot \underline{d} - l_{cyl}\left(t\right)^2 = 0 \tag{2.10}$$

where

$$\underline{d} = \underline{r}_D + \underline{s}_{D,C} = \underline{r}_D + \underline{A}_2 \cdot \underline{s}'_{D,C}$$

$$\underline{A}_2 = \begin{bmatrix} \cos\theta_2 & -\sin\theta_2 \\ \sin\theta_2 & \cos\theta_2 \end{bmatrix}$$

$$\underline{s}_{A,B} = \begin{bmatrix} s_{A,B,x} \\ s_{A,B,y} \end{bmatrix} = \begin{bmatrix} -w_2 \cdot \cos\varphi_1 \\ w_2 \cdot \sin\varphi_1 \end{bmatrix}$$

$$\underline{s}'_{D,B} = \begin{bmatrix} s'_{D,B,x} \\ s'_{D,B,y} \end{bmatrix} = \begin{bmatrix} -e_{cm,x} \\ -e_{cm,y} \end{bmatrix}$$

$$\underline{s}'_{D,C} = \begin{bmatrix} s'_{D,C,x} \\ s'_{D,C,y} \end{bmatrix} = \begin{bmatrix} w_1 \cdot \cos\varphi_2 - e_{cm,x} \\ -w_1 \cdot \sin\varphi_2 - e_{cm,y} \end{bmatrix}$$

$\underline{A}_2$: Transform matrix of the boom's center-line angle θ_2
$\underline{s}'$: Distance vectors in local coordinate system with constant length
$\Phi^{ld,1}$: Longitudinal drive constraint (cylinder), 1 degree of freedom
$\underline{\Phi}^{r,2}$: Revolute joint constraint vector, 2 degrees of freedom

From the three equations generated from the kinematic constraint vectors the x and y position of the body mass center and the angle of the boom θ_2 is found depending on the cylinder length $l_{cyl}\left(t\right)$. The position constraint vector of the system is written.

$$\underline{\Phi}\left(\underline{q}, t\right) = \begin{bmatrix} \underline{r}_D + \underline{A}_2 \cdot \underline{s}'_{D,B} - \underline{s}_{A,B} \\ \underline{d}^T \cdot \underline{d} - l_{cyl}\left(t\right)^2 \end{bmatrix}$$

$$= \begin{bmatrix} x_D + s'_{D,B,x} \cdot \cos\theta_2 - s'_{D,B,y} \cdot \sin\theta_2 - s_{A,B,x} \\ y_D + s'_{D,B,x} \cdot \sin\theta_2 + s'_{D,B,y} \cdot \cos\theta_2 - s_{A,B,x} \\ d_x^2 + d_y^2 - l_{cyl}\left(t\right)^2 \end{bmatrix} = \underline{0} \tag{2.11}$$

where

$$d_x = x_D + s'_{D,C,x} \cdot \cos\theta_2 - s'_{D,C,y} \cdot \sin\theta_2$$

$$d_y = y_D + s'_{D,C,x} \cdot \sin\theta_2 + s'_{D,C,y} \cdot \cos\theta_2$$

$\underline{q}$: Position vector
x_D : Global x-coordinate of point D
y_D : Global y-coordinate of point D
$\underline{\Phi}\left(\underline{q}, t\right)$: Position constrain vector

Obtaining the unknown position vector $\underline{q}$ from the position constraints in equation (2.11) analytically can be difficult due to the trigonometric and quadric functions. Because of this, the position vector is solved numerically by use of Newton-Raphson's Method.

Next, the velocity constraint vector is obtained from the time derivative of the position constraint vector in equation (2.11).

$$\dot{\underline{\Phi}}\left(\underline{q}, \dot{\underline{q}}, t\right) = \begin{bmatrix} \dot{\underline{r}}_D + \dot{\theta}_2 \cdot \underline{B}_2 \cdot \underline{s}'_{D,B} \\ 2 \cdot \underline{d}^T \cdot \dot{\underline{d}} - 2 \cdot l_{cyl}\left(t\right) \cdot \dot{l}_{cyl}\left(t\right) \end{bmatrix} = \underline{0} \tag{2.12}$$

where

$$\dot{\underline{d}} = \dot{\underline{r}}_D + \dot{\theta}_2 \cdot \underline{B}_2 \cdot \underline{s}'_{D,C}$$

$$\underline{B}_2 = \begin{bmatrix} -\sin\theta_2 & -\cos\theta_2 \\ \cos\theta_2 & -\sin\theta_2 \end{bmatrix}$$

$\underline{B}_2$: Transformation matrix, the time derivative of $\underline{A}_2$ divided by $\dot{\theta}_2$

Re-writing equation (2.12) it is expressed as the Jacobian matrix, velocity vector (Cartesian velocities and angular velocity) and time-depending input vector.

$$\dot{\underline{\Phi}}\left(\underline{q}, \dot{\underline{q}}, t\right) = \underline{\Phi}_{\underline{q}}\left(\underline{q}\right) \cdot \dot{\underline{q}} - \underline{\phi}_v\left(t\right)$$

giving

$$\dot{\underline{q}} = \underline{\Phi}_{\underline{q}}^{-1}\left(\underline{q}\right) \cdot \underline{\phi}_v\left(t\right)$$

or

$$\begin{bmatrix} \dot{\underline{r}}_D \\ \dot{\theta}_2 \end{bmatrix} = \begin{bmatrix} \underline{I} & \underline{B}_2 \cdot \underline{s}'_{D,B} \\ 2 \cdot \underline{d}^T & 2 \cdot \underline{d}^T \cdot \underline{B}_2 \cdot \underline{s}'_{D,C} \end{bmatrix}^{-1} \cdot \begin{bmatrix} \underline{0} \\ 2 \cdot l_{cyl}\left(t\right) \cdot \dot{l}_{cyl}\left(t\right) \end{bmatrix} \tag{2.13}$$

$\underline{\Phi}_{\underline{q}}\left(\underline{q}\right)$: Jacobian matrix
$\underline{\phi}_v\left(t\right)$: Input vector to the velocity constrain

Finally, the acceleration constraint vector is derived from the time derivative of equation (2.12).

$$\ddot{\underline{\Phi}}\left(\underline{q}, \dot{\underline{q}}, \ddot{\underline{q}}, t\right) = \begin{bmatrix} \ddot{\underline{r}}_D + \ddot{\theta}_2 \cdot \underline{B}_2 \cdot \underline{s}'_{D,B} - \dot{\theta}_2^2 \cdot \underline{A}_2 \cdot \underline{s}'_{D,B} \\ 2 \cdot \underline{d}^T \cdot \ddot{\underline{d}} + 2 \cdot \dot{\underline{d}}^T \cdot \dot{\underline{d}} - 2 \cdot l_{cyl}\left(t\right) \cdot \ddot{l}_{cyl}\left(t\right) - 2 \cdot \dot{l}_{cyl}^2\left(t\right) \end{bmatrix} = \underline{0} \tag{2.14}$$

where

$$\ddot{\underline{d}} = \ddot{\underline{r}}_D + \ddot{\theta}_2 \cdot \underline{B}_2 \cdot \underline{s}'_{D,C} - \dot{\theta}_2^2 \cdot \underline{A}_2 \cdot \underline{s}'_{D,C}$$

Re-written as the Jacobian matrix, acceleration vector and time-depending input vector.

$$\ddot{\underline{\Phi}}\left(\underline{q}, \dot{\underline{q}}, \ddot{\underline{q}}, t\right) = \underline{\Phi}_{\underline{q}}\left(\underline{q}\right) \cdot \ddot{\underline{q}} - \underline{\phi}_a\left(\underline{q}, \dot{\underline{q}}, t\right)$$

giving

$$\ddot{\underline{q}} = \underline{\Phi}_{\underline{q}}^{-1}\left(\underline{q}\right) \cdot \underline{\phi}_a\left(\underline{q}, \dot{\underline{q}}, t\right)$$

or

$$\begin{bmatrix} \ddot{\underline{r}}_D \\ \ddot{\theta}_2 \end{bmatrix} = \begin{bmatrix} \underline{I} & \underline{B}_2 \cdot \underline{s}'_{D,B} \\ 2 \cdot \underline{d}^T & 2 \cdot \underline{d}^T \cdot \underline{B}_2 \cdot \underline{s}'_{D,C} \end{bmatrix}^{-1} \cdot \begin{bmatrix} \dot{\theta}_2^2 \cdot \underline{A}_2 \cdot \underline{s}'_{D,B} \\ 2 \cdot \underline{d}^T \cdot \dot{\theta}_2^2 \cdot \underline{A}_2 \cdot \underline{s}'_{D,C} - 2 \cdot \dot{\underline{d}}^T \cdot \dot{\underline{d}} + 2 \cdot \dot{l}_{cyl}^2\left(t\right) \end{bmatrix} \tag{2.15}$$

$\underline{\phi}_a\left(t\right)$: Input vector to the acceleration constrain

2.1.2 Kinetics

Finding the reaction forces in the revolute joint and the cylinder force is the aim of the kinetics. Accelerations computed in the kinematics section are used to compute the acceleration forces and moment.

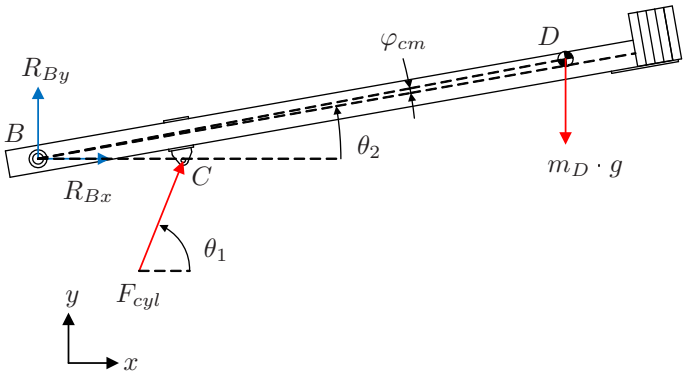

(a) FBD

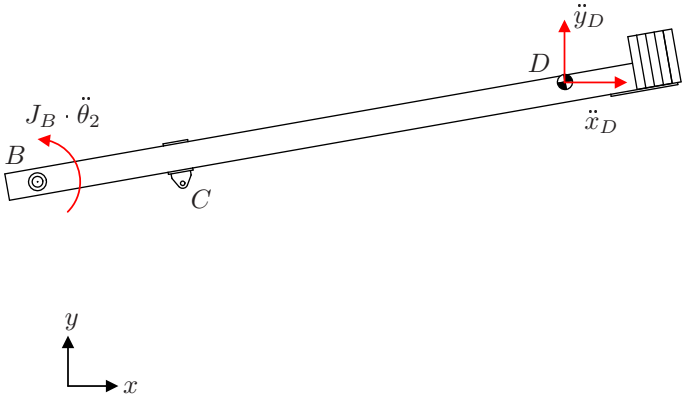

(b) KD

Figure 2.3: FBD and KD of arm

F_{cyl} : Cylinder force
J_B : Mass moment of inertia around point B
R_{Bx} : Reaction force in x-direction in revolute joint
R_{By} : Reaction force in y-direction in revolute joint

From the free body diagram (FBD) and the kinetic diagram (KD) in Figure 2.3 the force and moment equations of motion are put up. Moment equilibrium is taken around the joint in point B.

$$\Sigma F_x = R_{Bx} + \cos\theta_1 \cdot F_{cyl} = m_D \cdot \ddot{x}_D \tag{2.16}$$

$$\Sigma F_y = R_{By} + \sin\theta_1 \cdot F_{cyl} - m_D \cdot g = m_D \cdot \ddot{y}_D$$

$$\Rightarrow R_{By} + \sin\theta_1 \cdot F_{cyl} = m_D \cdot \ddot{y}_D + m_D \cdot g \tag{2.17}$$

$$\Sigma M_B = w_1 \cdot \begin{bmatrix} \cos(\theta_2 - \varphi_2) \\ \sin(\theta_2 - \varphi_2) \end{bmatrix} \times \begin{bmatrix} \cos\theta_1 \\ \sin\theta_1 \end{bmatrix} \cdot F_{cyl} + w_{cm} \cdot \begin{bmatrix} \cos(\theta_2 + \varphi_{cm}) \\ \sin(\theta_2 + \varphi_{cm}) \end{bmatrix} \times \begin{bmatrix} 0 \\ -m_D \cdot g \end{bmatrix} = J_B \cdot \ddot{\theta}_2$$

$$\Rightarrow w_1 \cdot \sin(\theta_1 - \theta_2 + \varphi_2) \cdot F_{cyl} = J_B \cdot \ddot{\theta}_2 + w_{cm} \cdot \cos(\theta_2 + \varphi_{cm}) \cdot m_D \cdot g \tag{2.18}$$

where

$$J_B = \frac{1}{12} \cdot m_{arm} \cdot l_{arm}^2 + m_{arm} \cdot \left(\frac{l_{arm}}{2} - b_7 \right)^2 + m_{pl} \cdot \left((l_{pl} - b_7)^2 + h_{pl}^2 \right)$$

$$w_{cm} = \sqrt{e_{cm,x}^2 + e_{cm,y}^2}$$

$$\varphi_{cm} = \tan^{-1} \left(\frac{e_{cm,y}}{e_{cm,x}} \right)$$

Putting the equilibrium equations above on matrix form, the unknown forces are computed as a vector.

$$\begin{bmatrix} 1 & 0 & \cos\theta_1 \\ 0 & 1 & \sin\theta_1 \\ 0 & 0 & w_1 \cdot \sin(\theta_1 - \theta_2 + \varphi_2) \end{bmatrix} \cdot \begin{bmatrix} R_{Bx} \\ R_{By} \\ F_{cyl} \end{bmatrix} = \begin{bmatrix} m_D & 0 & 0 \\ 0 & m_D & 0 \\ 0 & 0 & J_B \end{bmatrix} \cdot \begin{bmatrix} \ddot{x}_D \\ \ddot{y}_D \\ \ddot{\theta}_2 \end{bmatrix} + \begin{bmatrix} 0 \\ m_D \cdot g \\ w_{cm} \cdot \cos(\theta_2 + \varphi_{cm}) \cdot m_D \cdot g \end{bmatrix}$$

or

$$\underline{R} \cdot \underline{f} = \underline{M} \cdot \underline{\ddot{q}} + \underline{b}$$

giving

$$\underline{f} = \underline{R}^{-1} \cdot \left(\underline{M} \cdot \underline{\ddot{q}} + \underline{b} \right) \tag{2.19}$$

2.1.3 Deflection

The beam deflection is computed from differential equations of the curvature. The exact expression of the curvature is given by both the first and second derivative of the deflection. For small angles of deflection (first derivative) the curvature is approximately equal to the second derivative of the deflection as seen in the equation below [2, p.681]. For angles less than 1 degree the approximation is considered valid.

$$\kappa = \frac{v''}{(1 + (v')^2)^{\frac{3}{2}}} \approx v'' \tag{2.20}$$

For a beam whose material is linearly elastic and follows Hook's law, the curvature, κ, is given by the bending moment equation, Young's modulus for the material and the second area moment of inertia. Using the approximation in equation (2.20) yields the differential equation of the deflection curve.

$$\kappa = \frac{M_z(x_a)}{E \cdot I_z} \tag{2.21}$$

$$\Rightarrow v'' = \frac{M_z(x_a)}{E \cdot I_z} \tag{2.22}$$

The bending moment equation is computed in three sections along the local x coordinate of the arms center-line. First section stretches from the revolute joint up to the cylinder,the second section from the cylinder to the payload and the third section from the payload to the end of the arm. The cylinder force and the reaction forces are computed from the formulas in subsection 2.1.2.

Section 1: $0 \leqslant x_a < x_1$

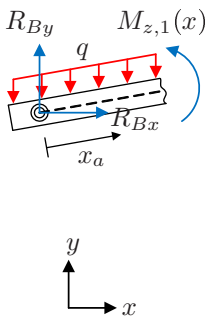

Figure 2.4: FBD of section 1

$$\Sigma M_{sec,1} = 0 \text{ Nm} = \left(\underline{A}_2 \cdot \begin{bmatrix} -x_a \\ 0 \end{bmatrix}\right) \times \begin{bmatrix} R_{Bx} \\ R_{By} \end{bmatrix} + \left(\underline{A}_2 \cdot \begin{bmatrix} -\frac{x_a}{2} \\ 0 \end{bmatrix}\right) \times \begin{bmatrix} 0 \\ -q \cdot x_a \end{bmatrix}$$

$$+ \left(\underline{A}_2 \cdot \begin{bmatrix} -x_a - \frac{b_7}{2} \\ 0 \end{bmatrix}\right) \times \begin{bmatrix} 0 \\ -q \cdot b_7 \end{bmatrix} + M_{z,1}(x_a)$$

$$\Rightarrow M_{z,1}(x_a) = \left(\underline{A}_2 \cdot \begin{bmatrix} x_a \\ 0 \end{bmatrix}\right) \times \begin{bmatrix} R_{Bx} \\ R_{By} \end{bmatrix} + \left(\underline{A}_2 \cdot \begin{bmatrix} \frac{x_a}{2} \\ 0 \end{bmatrix}\right) \times \begin{bmatrix} 0 \\ -q \cdot x_a \end{bmatrix} + \left(\underline{A}_2 \cdot \begin{bmatrix} x_a + \frac{b_7}{2} \\ 0 \end{bmatrix}\right) \times \begin{bmatrix} 0 \\ -q \cdot b_7 \end{bmatrix}$$

$$= x_a \cdot \left(\cos\theta_2 \cdot \left(R_{By} - \frac{q}{2} \cdot x_a - q \cdot b_7\right) - \sin\theta_2 \cdot R_{Bx}\right) - \cos\theta_2 \cdot \frac{q}{2} \cdot b_7^2 \tag{2.23}$$

Section 2: $x_1 \leqslant x_a < x_2$

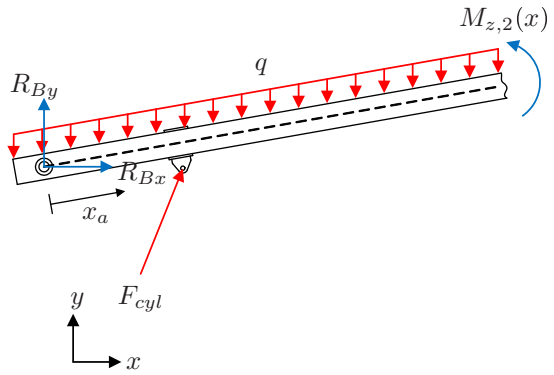

Figure 2.5: FBD of section 2

$$\Sigma M_{sec,2} = 0 \text{ Nm} = -M_{z,1}(x_a) + \left(\underline{A}_2 \cdot \begin{bmatrix} -x_a + x_1 \\ -w_1 \cdot \sin\varphi_2 \end{bmatrix}\right) \times \begin{bmatrix} \cos\theta_1 \\ \sin\theta_1 \end{bmatrix} \cdot F_{cyl} + M_{z,2}(x_a)$$

$$\Rightarrow M_{z,2}(x_a) = M_{z,1}(x_a) + \left(\underline{A}_2 \cdot \begin{bmatrix} x_a - x_1 \\ w_1 \cdot \sin\varphi_2 \end{bmatrix}\right) \times \begin{bmatrix} \cos\theta_1 \\ \sin\theta_1 \end{bmatrix} \cdot F_{cyl}$$

$$= x_a \cdot \left(\cos\theta_2 \cdot \left(R_{By} - \frac{q}{2} \cdot x_a - q \cdot b_7\right) - \sin\theta_2 \cdot R_{Bx} + \sin(\theta_1 - \theta_2) \cdot F_{cyl}\right)$$

$$- \cos\theta_2 \cdot \frac{q}{2} \cdot b_7^2 - (x_1 \cdot \sin(\theta_1 - \theta_2) + w_1 \cdot \sin\varphi_2 \cdot \cos(\theta_1 - \theta_2)) \cdot F_{cyl} \tag{2.24}$$

Section 3: $x_2 \leqslant x_a < x_{end}$

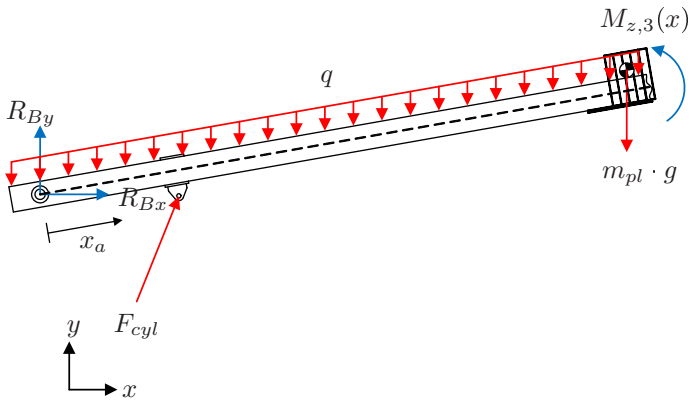

Figure 2.6: FBD of section 3

$$\Sigma M_{sec,2} = 0 \text{ Nm} = -M_{z,2}(x_a) + \underline{A}_2 \cdot \begin{bmatrix} -x_a + x_2 \\ +h_{pl} \end{bmatrix} \times \begin{bmatrix} 0 \\ -m_{pl} \cdot g \end{bmatrix} + M_{z,3}(x_a)$$

$$\begin{aligned} \Rightarrow M_{z,3}(x_a) =& M_{z,2}(x_a) + \underline{A}_2 \cdot \begin{bmatrix} x_a - x_2 \\ -h_{pl} \end{bmatrix} \times \begin{bmatrix} 0 \\ -m_{pl} \cdot g \end{bmatrix} \\ =& x_a \cdot \left(\cos\theta_2 \cdot \left(R_{By} - \frac{q}{2} \cdot x_a - q \cdot b_7 \right) - \sin\theta_2 \cdot R_{Bx} + \sin(\theta_1 - \theta_2) \cdot F_{cyl} - \cos\theta_2 \cdot m_{pl} \cdot g \right) \\ & - \cos\theta_2 \cdot \frac{q}{2} \cdot b_7^2 - (x_1 \cdot \sin(\theta_1 - \theta_2) + w_1 \cdot \sin\varphi_2 \cdot \cos(\theta_1 - \theta_2)) \cdot F_{cyl} \\ & + (x_2 \cdot \cos\theta_2 - h_{pl} \cdot \sin\theta_2) \cdot m_{pl} \cdot g \end{aligned} \tag{2.25}$$

where

$$q = \frac{m_{arm} \cdot g}{l_{arm}}$$

$$x_1 = w_1 \cdot \cos\varphi_2$$

$$x_2 = l_{pl} - b_7$$

$$x_{end} = l_{arm} - b_7$$

The second area moment of inertia for a hollow rectangular cross-sectional area yields the following equation.

$$I_z = \frac{1}{12} \cdot \left(w_{arm} \cdot h_{arm}^3 - (w_{arm} - 2 \cdot t_{arm}) \cdot (h_{arm} - 2 \cdot t_{arm})^3 \right) \tag{2.26}$$

Integration of the differential equation in equation (2.22) gives the angle of deflection, which integrated gives

the deflection. Angle of deflection and deflection for section 1 is computed.

$$E \cdot I_z \cdot v_1'(x_a) = \int M_{z,1}(x_a) \cdot dx$$
$$= \frac{1}{2} \cdot \left(\cos\theta_2 \cdot \left(R_{By} - \frac{q}{3} \cdot x_a - q \cdot b_7\right) - \sin\theta_2 \cdot R_{Bx}\right) \cdot x_a^2 - \cos\theta_2 \cdot \frac{q}{2} \cdot b_7^2 \cdot x_a + c_0 \quad (2.27)$$

$$E \cdot I_z \cdot v_1(x_a) = \int\int M_{z,1}(x_a) \cdot dx^2$$
$$= \frac{1}{6} \cdot \left(\cos\theta_2 \cdot \left(R_{By} - \frac{q}{4} \cdot x_a - q \cdot b_7\right) - \sin\theta_2 \cdot R_{Bx}\right) \cdot x_a^3$$
$$- \cos\theta_2 \cdot \frac{q}{4} \cdot b_7^2 \cdot x_a^2 + c_0 \cdot x_a + c_1 \quad (2.28)$$

Next, the angle of deflection and deflection for section 2 is computed.

$$E \cdot I_z \cdot v_2'(x_a) = \int M_{z,2}(x_a) \cdot dx$$
$$= \frac{1}{2} \cdot \left(\cos\theta_2 \cdot \left(R_{By} - \frac{q}{3} \cdot x_a - q \cdot b_7\right) - \sin\theta_2 \cdot R_{Bx} + \sin(\theta_1 - \theta_2) \cdot F_{cyl}\right) \cdot x_a^2$$
$$- \left(\cos\theta_2 \cdot \frac{q}{2} \cdot b_7^2 + (x_1 \cdot \sin(\theta_1 - \theta_2) + w_1 \cdot \sin\varphi_2 \cdot \cos(\theta_1 - \theta_2)) \cdot F_{cyl}\right) \cdot x_a + c_2 \quad (2.29)$$

$$E \cdot I_z \cdot v_2(x_a) = \int\int M_{z,2}(x_a) \cdot dx^2$$
$$= \frac{1}{6} \cdot \left(\cos\theta_2 \cdot \left(R_{By} - \frac{q}{4} \cdot x_a - q \cdot b_7\right) - \sin\theta_2 \cdot R_{Bx} + \sin(\theta_1 - \theta_2) \cdot F_{cyl}\right) \cdot x_a^3$$
$$- \frac{1}{2} \cdot \left(\cos\theta_2 \cdot \frac{q}{2} \cdot b_7^2 + (x_1 \cdot \sin(\theta_1 - \theta_2) + w_1 \cdot \sin\varphi_2 \cdot \cos(\theta_1 - \theta_2)) \cdot F_{cyl}\right) \cdot x_a^2$$
$$+ c_2 \cdot x_a + c_3 \quad (2.30)$$

Finally, the angle of deflection and deflection for section 2 is computed.

$$E \cdot I_z \cdot v_3'(x_a) = \int M_{z,3}(x_a) \cdot dx$$
$$= \frac{1}{2} \cdot \left(\cos\theta_2 \cdot \left(R_{By} - \frac{q}{3} \cdot x_a - q \cdot b_7\right) - \sin\theta_2 \cdot R_{Bx} + \sin(\theta_1 - \theta_2) \cdot F_{cyl} - \cos\theta_2 \cdot m_{pl} \cdot g\right) \cdot x_a^2$$
$$- \left(\cos\theta_2 \cdot \frac{q}{2} \cdot b_7^2 + (x_1 \cdot \sin(\theta_1 - \theta_2) + w_1 \cdot \sin\varphi_2 \cdot \cos(\theta_1 - \theta_2)) \cdot F_{cyl}\right) \cdot x_a$$
$$+ (x_2 \cdot \cos\theta_2 - h_{pl} \cdot \sin\theta_2) \cdot x_a \cdot m_{pl} \cdot g + c_4 \quad (2.31)$$

$$E \cdot I_z \cdot v_3(x_a) = \int\int M_{z,3}(x_a) \cdot dx^2$$
$$= \frac{1}{6} \cdot \left(\cos\theta_2 \cdot \left(R_{By} - \frac{q}{4} \cdot x_a - q \cdot b_7\right) - \sin\theta_2 \cdot R_{Bx} + \sin(\theta_1 - \theta_2) \cdot F_{cyl} - \cos\theta_2 \cdot m_{pl} \cdot g\right) \cdot x_a^3$$
$$- \frac{1}{2} \cdot \left(\cos\theta_2 \cdot \frac{q}{2} \cdot b_7^2 + (x_1 \cdot \sin(\theta_1 - \theta_2) + w_1 \cdot \sin\varphi_2 \cdot \cos(\theta_1 - \theta_2)) \cdot F_{cyl}\right) \cdot x_a^2$$
$$+ \frac{1}{2}(x_2 \cdot \cos\theta_2 - h_{pl} \cdot \sin\theta_2) \cdot x_a^2 \cdot m_{pl} \cdot g + c_4 \cdot x_a + c_5 \quad (2.32)$$

Initial conditions are put up to determine the constants $c_{0...5}$.

$$v_1(0) = 0$$

$$v_1(x_1) = 0$$

$$v_2(x_1) = v_1(x_1)$$

$$v_2'(x_1) = v_1'(x_1)$$

$$v_3(x_2) = v_2(x_2)$$

$$v_3'(x_2) = v_2'(x_2)$$

Inserting the initial conditions into equation (2.27) to equation (2.32) the above equality equations are put up on matrix form to find the constants.

$$\begin{bmatrix} 0 & 1 & 0 & 0 & 0 & 0 \\ -x_1 & -1 & 0 & 0 & 0 & 0 \\ -x_1 & -1 & x_1 & 1 & 0 & 0 \\ -1 & 0 & 1 & 0 & 0 & 0 \\ 0 & 0 & -x_2 & -1 & x_2 & 1 \\ 0 & 0 & -1 & 0 & 1 & 0 \end{bmatrix} \cdot \begin{bmatrix} c_0 \\ c_1 \\ c_2 \\ c_3 \\ c_4 \\ c_5 \end{bmatrix} = \begin{bmatrix} 0 \\ \frac{1}{6} \cdot \left(\cos\theta_2 \cdot \left(R_{By} - \frac{q}{4} \cdot x_1\right) - \sin\theta_2 \cdot R_{Bx}\right) \cdot x_1^3 - \cos\theta_2 \cdot \frac{q}{4} \cdot b_7^2 \cdot x_1^2 \\ \left(\frac{1}{3} \cdot x_1 \cdot \sin(\theta_1 - \theta_2) + \frac{1}{2} \cdot w_1 \cdot \sin\varphi_2 \cdot \cos(\theta_1 - \theta_2)\right) \cdot x_1^2 \cdot F_{cyl} \\ \left(\frac{1}{2} \cdot x_1 \cdot \sin(\theta_1 - \theta_2) + w_1 \cdot \sin\varphi_2 \cdot \cos(\theta_1 - \theta_2)\right) \cdot x_1 \cdot F_{cyl} \\ \left(-\frac{1}{3} \cdot x_2 \cdot \cos\theta_2 + \frac{1}{2} \cdot h_{pl} \cdot \sin\theta_2\right) \cdot x_2^2 \cdot m_{pl} \cdot g \\ \left(-\frac{1}{2} \cdot x_2 \cdot \cos\theta_2 + h_{pl} \cdot \sin\theta_2\right) \cdot x_2 \cdot m_{pl} \cdot g \end{bmatrix}$$

or

$$\underline{\underline{H}} \cdot \underline{c} = \underline{u}$$

giving

$$\underline{c} = \underline{\underline{H}}^{-1} \cdot \underline{u} \tag{2.33}$$

2.1.4 Lumped Beam Model

In order to model a beam's deflection and the resulting effect of it, a lumped beam model can be used. Instead of using a single rigid beam, one divides the beam into two or more rigid sections. The sections are connected by rotational joints, torsional springs, and eventually torsional dampers. The coefficients of the force elements are determined by physical dimensions and material properties. The total length of the sections must be equal to the length of the rigid beam. The principle is shown in Figure 2.7 (the total length of the sections is *not* equal to the total length of the rigid beam in the figure).

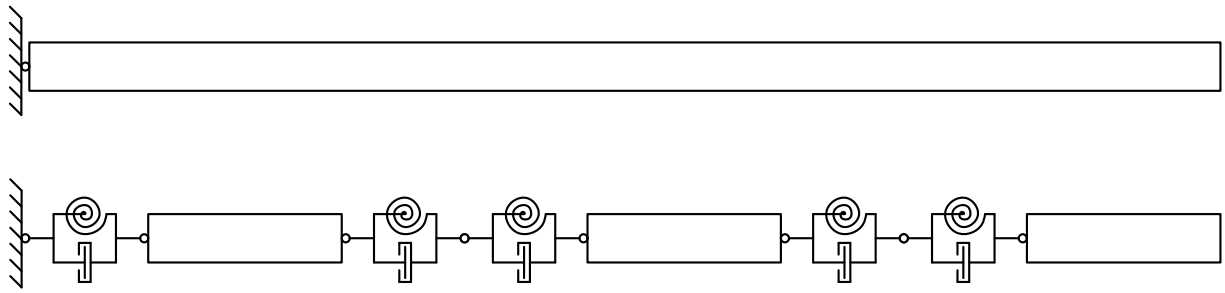

Figure 2.7: Rigid beam (top) vs. lumped beam (bottom).

The torsional spring stiffness for a beam section is described in equation (2.34).

$$k_{sec} = \frac{2 \cdot E \cdot I}{l_{sec}} \tag{2.34}$$

where

E : Young's modulus of section
I : Area moment of inertia of section
k_{sec} : Torsional spring stiffness of section
l_{sec} : Length of section

When two sections are to be connected, the effective stiffness of the two connected springs can be written as equation (2.35).

$$\begin{aligned} \frac{1}{k_{eff}} &= \frac{1}{k_{sec}} + \frac{1}{k_{sec}} \\ \Rightarrow k_{eff} &= \frac{k_{sec}}{2} \\ k_{eff} &= \frac{E \cdot I}{l_{sec}} \end{aligned} \tag{2.35}$$

where

k_{eff} : Effective torsional spring stiffness

In general, damping in a system can be described by the damping ratio, ξ, see equation (2.36).

$$\begin{aligned} \xi &= \frac{c}{c_{cr}} \\ \Rightarrow c &= \xi \cdot c_{cr} \end{aligned} \tag{2.36}$$

where

$$c_{cr} = 2 \cdot \sqrt{k \cdot J} \tag{2.37}$$

c : Torsional damping
c_{cr} : Critical torsional damping
J : Moment of inertia
ξ : Damping ratio

The effective damping of two dampers connected in series follows the same form as two springs connected in series, see equation (2.38).

$$\begin{aligned} \frac{1}{c_{eff}} &= \frac{1}{c} + \frac{1}{c} \\ \Rightarrow c_{eff} &= \frac{c}{2} \\ &= \xi \cdot \sqrt{k \cdot J} \\ &= \xi \cdot \sqrt{2 \cdot k_{eff} \cdot J} \end{aligned} \tag{2.38}$$

where

c_{eff} : Effective torsional damping coefficient

Assuming that the moment of inertia of the beam sections can be described by the equation for a long, thin rod yields equation (2.39). This assumption is valid because the steel thickness of the beam is small relative to the length.

$$J_{sec} = \frac{1}{3} \cdot m_{sec} \cdot l_{sec}^2 \tag{2.39}$$

According to [3, p. 97] the damping ratio, ξ, for typical steel structures is 1-2 %. $\xi = 0.02$ is therefore assumed for the beam..

2.2 Hydraulic System

This section describes the hydraulic system and all its components. Each component is described mathematically and valve characteristics are drawn to be used as data table input for the valve blocks in the simulation model.

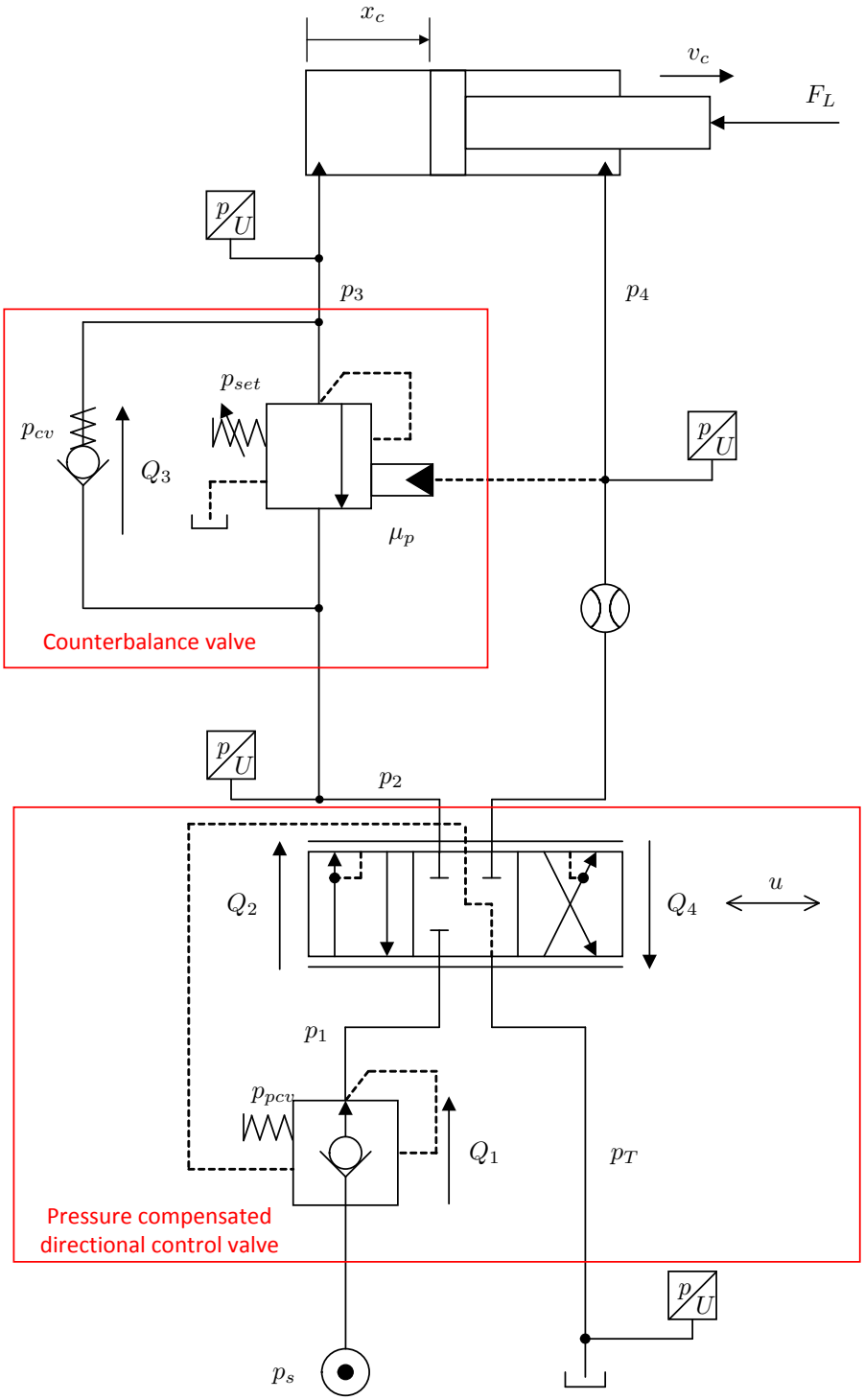

Figure 2.8: Hydraulic schematic - *consisting of a pressure source, a directional control valve with internal pressure compensation, a counterbalance valve and a cylinder*

In Figure 2.8 the hydraulic schematic is shown. It consists of a pressure source, a directional control valve (DCV) with an internal pressure compensation valve (PCV), a counterbalance valve (CBV) and a cylinder.

Also pressure transducers and a flow meter available on the test rig is seen in the schematic.

2.2.1 Pressure Compensated Directional Control Valve

To provoke instabilities in the system a pressure compensated valve block disposable on the test rig is chosen. The valve block has a linear flow control spool and the rated flow of the spool is 25 $\frac{\text{l}}{\text{min}}$.

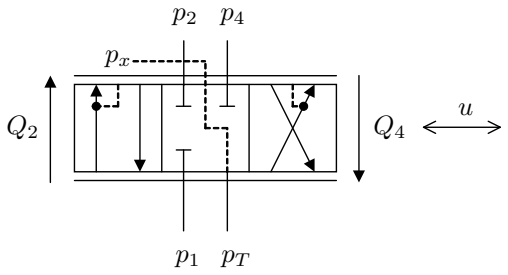

Figure 2.9: DCV symbol - *FC spool with closed neutral position.*

p_1 : Compensated pressure
p_2 : Line 2 pressure
p_4 : Line 4 pressure
p_T : Tank pressure
p_x : LS pressure
Q_2 : DCV restriction flow from port P to A / A to T
Q_4 : DCV restriction flow from port B to T / P to B
u : Main spool opening

Figure 2.9 shows the DCV symbol for a linear flow control spool with closed neutral position. The flow through the valve is proportional to the opening of the main spool, u. The spool is symmetrical giving equal opening magnitude in both directions.

For $u \geqslant 0$:

$$Q_2 = K_1 \cdot u \cdot \sqrt{p_1 - p_2} \tag{2.40}$$

$$Q_4 = K_1 \cdot u \cdot \sqrt{p_4 - p_T} \tag{2.41}$$

For $u < 0$:

$$Q_2 = K_1 \cdot u \cdot \sqrt{p_2 - p_T} \tag{2.42}$$

$$Q_4 = K_1 \cdot u \cdot \sqrt{p_1 - p_4} \tag{2.43}$$

The main spool opening, u, is determined by the spool position, maximum spool travel and spool travel dead band. The maximum spool travel is 7 mm and the dead band for the linear spool type is 0.8 mm. The main spool opening is expressed as a piece-wise defined function depending on the spool travel x_v.

$$u = \begin{cases} \dfrac{x_v + x_{db}}{-x_{max} + x_{db}} & : x_v < -x_{db} \\ 0 & : -x_{db} \leqslant x_v < x_{db} \\ \dfrac{x_v - x_{db}}{x_{max} - x_{db}} & : x_v \geqslant x_{db} \end{cases} \tag{2.44}$$

The dynamic of the main spool is assumed to yield the first order transfer function given in (2.45).

$$G_v(s) = \frac{1}{\frac{1}{\omega_v} \cdot s + 1} \tag{2.45}$$

where

ω_v : Eigenfrequency of the main spool

The flow coefficient K_1 is computed later in this section as the pressure compensator have to be taken into considerations.

Leakage flow is given in the data sheet in Table D.1. The leakage in the valve from port A and B to tank is 25 $\frac{\text{cm}^3}{\text{min}}$ at 100 bar. It is assumed a leakage from port P to tank with equal leakage rate as port A and B.

$$Q_{LA} = dQ_L \cdot (p_2 - p_T) \tag{2.46}$$

$$Q_{LB} = dQ_L \cdot (p_4 - p_T) \tag{2.47}$$

$$Q_{LP} = dQ_L \cdot (p_1 - p_T) \tag{2.48}$$

where

$$dQ_L = \frac{25 \cdot \frac{1}{60} \cdot 10^{-6}}{100 \cdot 10^5} \frac{\text{m}^3}{\text{s} \cdot \text{Pa}} = 4.17 \cdot 10^{-14} \frac{\text{m}^3}{\text{s} \cdot \text{Pa}}$$

Q_{LA} : Leakage from A port to tank
Q_{LB} : Leakage from B port to tank
Q_{LP} : Leakage from P port to tank

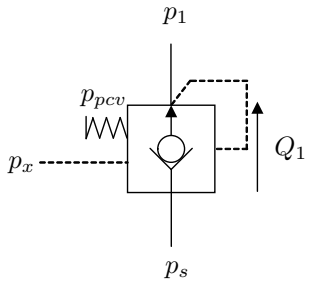

Figure 2.10: PCV symbol - *normally opened relief valve*

p_{pcv} : PCV spring pressure
p_s : Supply pressure
Q_1 : PCV restriction flow

The PCV is a normally opened pressure relief valve as seen in Figure 2.10. The spring pressure p_{pcv} and the back pressure p_x tries to open the valve, while the compensated pressure p_1 tries to close the valve. This results in a close to constant pressure drop across the main spool equal to the PCV spring pressure p_{pcv}.

$$p_1 = p_x + p_{pcv} + (1 - u_{pcv}) \cdot p_{fc,pcv}$$

$$\Rightarrow u_{pcv} = 1 - \frac{p_1 - p_x - p_{pcv}}{p_{fc,pcv}} \tag{2.49}$$

$p_{fc,pcv}$: Pressure to fully close the PCV spring

The valve opening is given in equation (2.49). Spring pressure increases proportional to the valve closing $(1 - u_{pcv})$, with a fully closed spring pressure rise denoted $p_{fc,pcv}$ assumed to be 1 bar. Dynamic of the PCV is neglected as it is assumed to have a higher eigenfrequency than the main spool.

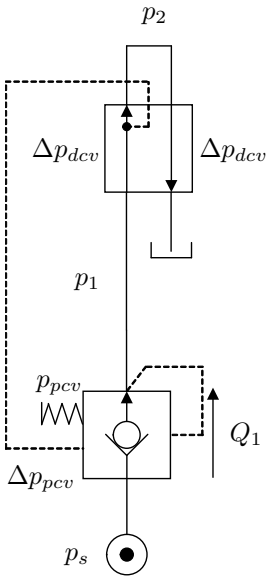

Figure 2.11: Shorted hydraulic circuit - *to determine valve characteristics*

$$Q_1 = K_3 \cdot u_{pcv} \cdot \sqrt{p_s - p_1} \tag{2.50}$$

Restriction flow through the PCV is given in equation (2.50). The flow coefficient K_3 (including discharge area, discharge coefficient and oil density) is assumed constant (increase in area proportional to valve opening) and computed from the shorted hydraulic circuit as seen in Figure 2.11 and equation (2.50). The flow through the circuit is equal to the rated PVB flow of 100 $\frac{\text{l}}{\text{min}}$. The supply pressure is set to 20 bar and the fully open PCV gives a pressure drop of 7 bar over the main spool, resulting in a pressure drop across the pressure compensator of 6 bar.

$$K_3 = \frac{100 \cdot \frac{1}{60{,}000}}{\sqrt{6 \cdot 10^5}} \frac{\text{m}^3}{\text{s} \cdot \sqrt{\text{Pa}}} = 2.15 \cdot 10^{-6} \frac{\text{m}^3}{\text{s} \cdot \sqrt{\text{Pa}}}$$

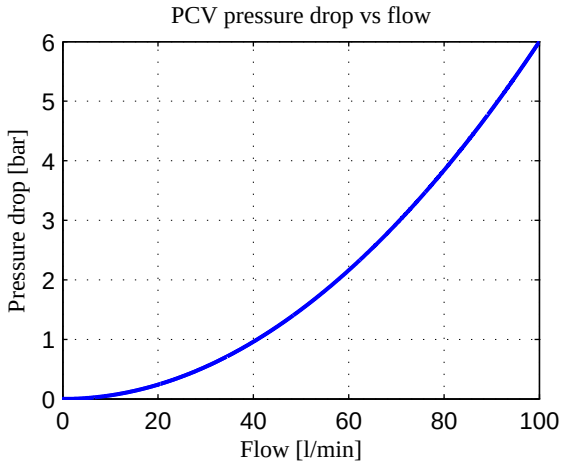

Figure 2.12: PCV characteristics - *flow vs pressure drop*

From the coefficient K_3 the flow vs pressure drop characteristics of the PCV is plotted up to rated flow in Figure 2.12.

Flow coefficient K_1 for the linear flow control spool is found from the rated main spool flow and the compensated pressure drop over the spool. The pressure drop over the spool is equal to the spring pressure of

the PCV, which at 25 $\frac{\text{l}}{\text{min}}$ is greater than 7 bar due to a smaller opening area of the PCV. To determine the pressure drop over the main spool the shorted hydraulic circuit in Figure 2.11 is used, but now with a circuit flow of 25 $\frac{\text{l}}{\text{min}}$. From the equations expressing circuit pressure drops and the restriction flow in equation (2.50) with equation (2.49) inserted, the pressure drop across the pressure compensator, Δp_{pcv}, is found.

$$p_2 = \Delta p_{dcv} \tag{2.51}$$

$$p_1 = p_2 + \Delta p_{dcv} = 2 \cdot \Delta p_{dcv} \tag{2.52}$$

$$\Delta p_{dcv} = \frac{p_s - \Delta p_{pcv}}{2} \tag{2.53}$$

$$Q_1 = K_3 \cdot \left(1 - \frac{p_1 - p_2 - p_{pcv}}{p_{fc,pcv}}\right) \cdot \sqrt{p_s - p_1} \tag{2.54}$$

$$\Rightarrow \left(\frac{2 \cdot p_{fc,pcv} \cdot Q_1}{K_3}\right)^2 = \Delta p_{pcv}^3 + 2 \cdot \left(2 \cdot \left(p_{fc,pcv} + p_{pcv}\right) - p_s\right) \cdot \Delta p_{pcv}^2 + \left(2 \cdot \left(p_{fc,pcv} + p_{pcv}\right) - p_s\right)^2 \cdot \Delta p_{pcv}$$

$$\Rightarrow \Delta p_{pcv} = \ [4.57,\ 3.33,\ 0.01] \text{ bar}$$

Solving the third order polynomial equation for Δp_{pcv} three positive real values are found. The largest value results in the lowest pressure drop, and the closest to 7 bar, across the spool. This value is assumed to be the pressure drop occurring. The flow coefficient for the linear spool, K_1, is computed from equation (2.42).

$$\Delta p_{dcv} = \frac{20 \text{ bar} - 4.57 \text{ bar}}{2} = 7.72 \text{ bar}$$

$$K_1 = \frac{25 \cdot \frac{1}{60{,}000}}{\sqrt{7.72 \cdot 10^5}} \frac{\text{m}^3}{\text{s} \cdot \sqrt{\text{Pa}}} = 4.74 \cdot 10^{-7} \frac{\text{m}^3}{\text{s} \cdot \sqrt{\text{Pa}}}$$

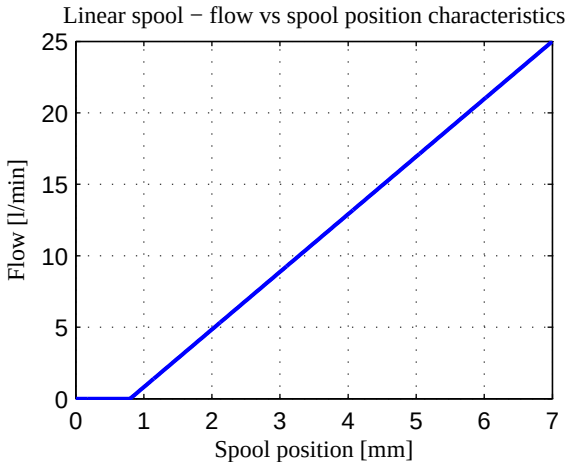

Figure 2.13: Linear flow control spool characteristics - *flow vs main spool position*

Flow vs main spool position characteristics for the linear flow control spool is seen in Figure 2.13. The flow is plotted from 0 to 25 $\frac{\text{l}}{\text{min}}$ with a pressure drop of 7.72 bar.

2.2.2 Counterbalance valve

Four counterbalance cartridge valves with different pilot area ratio are available. The counterbalance valves (CBV) are vented and have an adjustable spring pressure setting on the load holding relief valve. The free

flow flows through a spring loaded check valve with a check pressure of 2.8 bar. The flow capacity of the CBV's is 60 $\frac{\text{l}}{\text{min}}$.

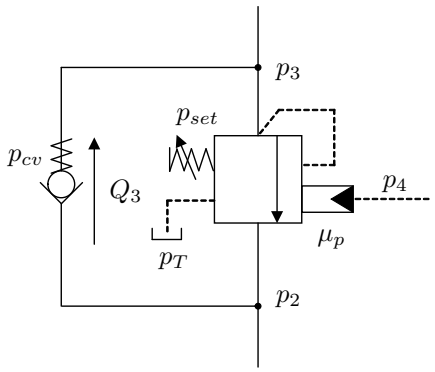

Figure 2.14: CBV symbol - *spring loaded check valve and load holding relief valve in parallel.*

$p_{2...4}$: Line pressure
p_{cv} : Check valve spring pressure
p_{set} : Load holding relief valve set pressure
p_T : Tank pressure
Q_3 : Volumetric flow through CBV
μ_p : Pilot area ratio

The CBV symbol is shown in Figure 2.14. From the figure the valve opening of the check valve and the load holding valve can be written.

$$p_2 = p_3 + p_{cv} + p_{fo,cv} \cdot u_{cv}$$

$$\Rightarrow u_{cv} = \frac{p_2 - p_3 - p_{cv}}{p_{fo,cv}} \tag{2.55}$$

$$\mu_p \cdot p_4 + p_3 = p_{set} + (1 + \mu_p) \cdot p_T + p_{fo,cbv} \cdot u_{cbv}$$

$$\Rightarrow u_{cbv} = \frac{\mu_p \cdot p_4 + p_3 - p_{set} - (1 + \mu_p) \cdot p_T}{p_{fo,cbv}} \tag{2.56}$$

$p_{fo,cbv}$: Pressure to fully open the load holding valve
$p_{fo,cv}$: Pressure to fully open the check valve
u_{cbv} : Opening of load holding valve
u_{cv} : Opening of check valve

The fully open check valve spring pressure, $p_{fo,cv}$, in equation (2.55) increases linear to the opening of the valve is assumed to be 1 bar. Likewise, the load holding valve spring pressure in equation (2.56) is linear to the opening of the valve, increasing with the fully open spring pressure $p_{fo,cbv}$. The load holding valve's fully open spring pressure is found where the load holding relief characteristics and the piloted open flow intersects (data sheet URL is found in appendix D.1). In Figure 2.15 the flow characteristic curve intersects the relief characteristics curves at 220 and 480 bar. The fully open spring pressure is based on this assumed to be $p_{fo,cbv} = 350$ bar.

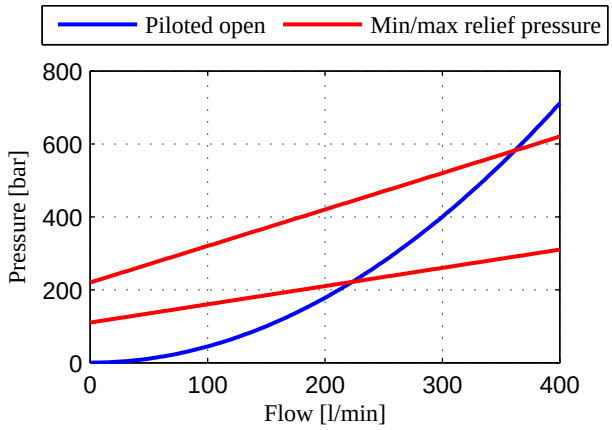

Figure 2.15: Load holding valve fully open spring pressure - *found where the piloted open characteristic curve intersects the relief pressure characteristic curve*

The dynamic of the load holding valve opening is assumed to yield the first order transfer function given in (2.57). Dynamic of the check valve is neglected.

$$G_{cbv}(s) = \frac{1}{\frac{1}{\omega_{cbv}} \cdot s + 1} \tag{2.57}$$

where

ω_{cbv} : Eigenfrequency of the CBV load holding valve

From the data sheet in appendix **??** the free flow and piloted open pressure drop characteristic is shown, where the flow coefficient K_2 is computed from yielding both the check valve and the load holding valve. For a flow of 60 $\frac{\text{l}}{\text{min}}$ the pressure drop is 16 bar.

$$K_2 = \frac{60 \cdot \frac{1}{60{,}000}}{\sqrt{16 \cdot 10^5}} \frac{\text{m}^3}{\text{s} \cdot \sqrt{\text{Pa}}} = 7.91 \cdot 10^{-7} \frac{\text{m}^3}{\text{s} \cdot \sqrt{\text{Pa}}}$$

Assuming proportional relation between the opening of the valve and the increase in area, the flow can be expressed by the following orifice equation.

$$Q_3 = K_2 \cdot u_{cv} \cdot \sqrt{p_2 - p_3} \;\; ; \qquad p_2 \geqslant p_3 \tag{2.58}$$

$$Q_3 = -K_2 \cdot u_{cbv} \cdot \sqrt{p_3 - p_2} \;\; ; \qquad p_2 < p_3 \tag{2.59}$$

The flow direction (and which valve's open) depends on the pressure difference between p_2 and p_3.

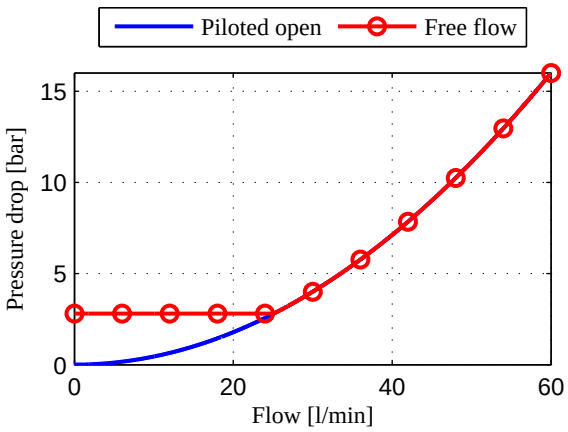

Figure 2.16: CBV characteristics - *free flow and piloted open pressure drop.*

In Figure 2.16 the flow vs pressure drop characteristics of the CBV are plotted using equation (2.58) with $u_{cv} = 1$. The free flow curve yields flow through the check valve, and the piloted open curve yields flow through the load holding valve. Due to the check valve spring there is a constant pressure drop in the free flow characteristics until the pressure difference between p_2 and p_3 overcomes the spring pressure.

2.2.3 Hydraulic Cylinder

The modelling of the hydraulic cylinder mainly consists of determining the force acting on the cylinder. Since the cylinder to be used in the experiment is brand new, any internal or external leakage is assumed to be zero. The forces acting on the hydraulic cylinder are shown in Figure 2.17.

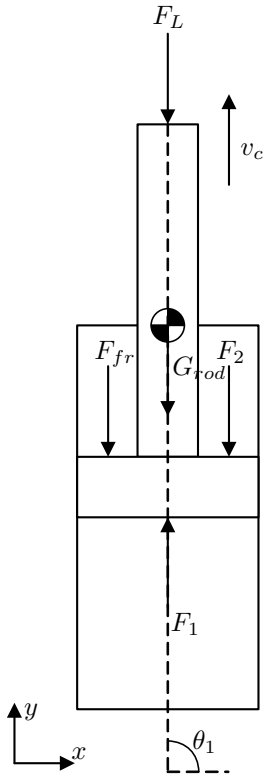

Figure 2.17: Forces acting on the hydraulic cylinder.

F_1 : Force generated from the pressure in chamber 1
F_2 : Force generated from the pressure in chamber 2
F_{fr} : Frictional force
F_L : External force acting on the cylinder
G_{rod} : Gravitational force of the cylinder rod and piston
v_c : Piston velocity relative to cylinder
θ_1 : Cylinder angle

$$F_1 = p_3 \cdot A \tag{2.60}$$

$$F_2 = p_4 \cdot \mu_c \cdot A \tag{2.61}$$

$$G_{rod} = m_{rod} \cdot g \cdot \sin\theta_1 \tag{2.62}$$

m_{rod} : Mass of the cylinder rod and piston

Friction in cylinders depends on multiple factors. Oil type, sealing material, temperature, relative velocity and pressure are only a few examples of these factors. There exists many models describing friction with

varying level of complexity. The models range from simple, constant models (Coulomb's friction model) to models including velocity dependency and surface properties (LuGre), to even more complex models. In [4], Ottestad, Nilsen & Hansen used the combination of Coulomb, Stribeck, viscous and pressure dependent friction shown in equation (2.63) to describe the frictional force in a hydraulic cylinder.

$$F_{fr} = F_c + (F_s - F_c) \cdot e^{-\frac{|v_c|}{v_0}} + C_v \cdot |v_c| + C_p \cdot |\Delta p| \tag{2.63}$$

where

$$\Delta p = |p_4 - p_3| \tag{2.64}$$

C_p : Pressure friction coefficient
C_v : Viscous friction coefficient
F_c : Coulomb friction
F_s : Static friction
v_0 : Stribeck velocity
v_c : Piston velocity relative to cylinder

A problem with the model is that is depends on many unknown, and it is therefore not suitable to use without performing physical experiments.

A simplified model considering only static and pressure dependent friction is shown in equation (2.65), and has been used by Bak in [5]. Note the different usage of the term "pressure dependent" by Ottestad et al. and Bak. Ottestad et al. uses the pressure dependency coefficient, C_p, multiplied by the absolute value of the pressure difference in the chambers to describe the pressure dependent friction. Bak uses the "pressure" dependency coefficient, $C_{p,\,Bak}$, multiplied by the absolute value of the force difference generated by the pressures in the chambers. Because the areas on the piston side and the rod side of the (asymmetric) cylinder are different, the two cases are not equal. The coefficient used by Ottestad et al. has the unit N/Pa (which equals to m^2), while Bak's is dimensionless. Even though it is not wrong to say that Bak's model depends on pressure (since the force is a function of the pressure), it would be more correct to use "force dependent".

$$F_{fr} = F_s + C_{p,\,Bak} \cdot |\Delta F| \tag{2.65}$$

where

$$F_s = A \cdot p_{static} \tag{2.66}$$

$$\Delta F = F_1 - F_2 \tag{2.67}$$

$C_{p,\,Bak}$: Pressure friction coefficient (proposed to 2...3 % in [5])
p_{static} : Pressure needed to overcome static friction (proposed to 1 bar in [5])

The actual frictional force can be found by using Newton's second law while performing physical experiments:

$$F_1 - F_2 - F_L - F_{frik} - G_{rod} = m_{eff} \cdot a_c$$

$$\Rightarrow F_{fr} = F_1 - F_2 - F_L - G_{rod} - m_{eff} \cdot a_c \tag{2.68}$$

where

a_c : Piston acceleration relative to cylinder

Until experiments can be performed, the friction model used by Bak in [5] with the proposed values of $C_{p,\,Bak} = 2$ % and $p_{static} = 1$ bar will be used. If the experiments shows that the model do not describe the friction sufficiently, the topic will be revisited.

2.3 Stability Analysis

The combination of a constant flow and a load holding valve often introduces instability in the system when handling negative load. As the pressure compensated directional control valve supplies the hydraulic circuit with a constant flow, independent to the load, the low pressurized cylinder chamber (on the side of in-flow) starts building up and thereby increasing the high pressurized chamber. When the pressures are high enough to overcome the load holding valve's spring pressure the valve starts opening, putting the payload in motion, and the pressures decreases due to fluid flowing out of the volumes. As the pressures now decreases the load holding valve starts closing and the pressure build up starts over. Now the motion of the payload contributes to additional pressure fluctuations leading to instability. Due to slower pressure build up low flow tends to be more unstable than a high flow.

To prove the stated instability a theoretical stability analysis is carried out. The idealized constant pressure drop over the directional control valve results in a flow that is independent to the system pressures and linear to the valve opening. The compensated DCV is simplified as a input flow and the simplified system is put up according to [1].

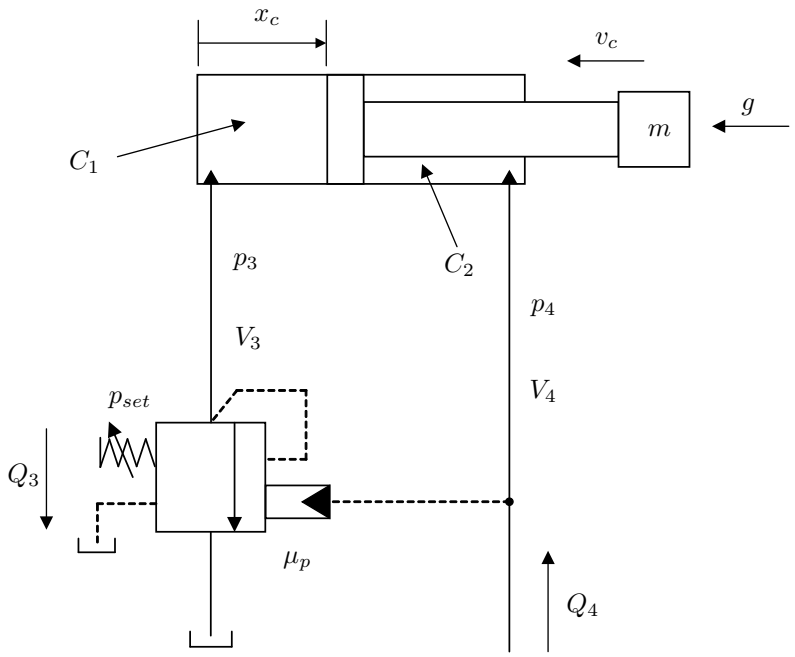

Figure 2.18: Simplified hydraulic diagram - *directional control valve, pressure compensator and pressure source is replaced with a volume flow. CBV back pressure is neglected.*

In Figure 2.18 the hydraulic system in Figure 2.8 is simplified by replacing the directional control valve, pressure compensator and pressure source with a volume flow. CBV back pressure is neglected and the payload is seen as a constant mass. Neglecting CBV dynamics, dead volume in cylinder and hoses, and assuming constant bulk modulus, the governing equations for the simplified system are:

$$m \cdot \dot{v}_c(t) = p_4(t) \cdot \mu_c \cdot A_c - p_3(t) \cdot A_c + m \cdot g \tag{2.69}$$

$$\dot{p}_3(t) \cdot C_1 = A_c \cdot v_c(t) - Q_3(t) \tag{2.70}$$

$$\dot{p}_4(t) \cdot C_2 = Q_4(t) - \mu_c \cdot A_c \cdot v_c(t) \tag{2.71}$$

$$Q_3(t) = K_2 \cdot u_{cbv}(t) \cdot \sqrt{p_3(t)} \tag{2.72}$$

$$u_{cbv}(t) \cdot p_{fo,cbv} = \mu_p \cdot p_4(t) + p_3(t) - p_{set} \tag{2.73}$$

where

$$C_1 = \frac{V_3}{\beta}$$

$$C_2 = \frac{V_4}{\beta}$$

$$V_3 = A_c \cdot x_c$$

$$V_4 = \mu_c \cdot A_c \cdot (s_c - x_c)$$

Linearizing around a steady state solution the Laplace-transform of equation (2.69) to equation (2.73) yields the following equations:

$$m \cdot V_c(s) \cdot s = P_4(s) \cdot \mu_c \cdot A_c - P_3(s) \cdot A_c \tag{2.74}$$

$$P_3(s) \cdot C_1 \cdot s = A_c \cdot V_c(s) - Q_3(s) \tag{2.75}$$

$$P_4(s) \cdot C_2 \cdot s = Q_4(s) - \mu_c \cdot A_c \cdot V_c(s) \tag{2.76}$$

$$Q_3(s) = K_{qu} \cdot U_{cbv}(s) + K_{qp} \cdot P_3(s) \tag{2.77}$$

$$U_{cbv}(s) \cdot p_{fo,cbv} = \mu_p \cdot P_4(s) + P_3(s) \tag{2.78}$$

The linearized flow coefficients in equation (2.77) are the derivative of the orifice equation dependent to spool opening and pressure. From equation (2.72) the flow coefficients are derived.

$$K_{qu} = \frac{\partial Q_3}{\partial u_{cbv}}|_{ss} = K_2 \cdot \sqrt{p_3^{(ss)}} \tag{2.79}$$

$$K_{qp} = \frac{\partial Q_3}{\partial p_3}|_{ss} = \frac{K_2 \cdot u_{cbv}^{(ss)}}{2 \cdot \sqrt{p_3^{(ss)}}} \tag{2.80}$$

where

$$u_{cbv}^{(ss)} = \frac{\mu_p \cdot p_4^{(ss)} + p_3^{(ss)} - p_{set}}{p_{fo,cbv}}$$

$$p_3^{(ss)} = \frac{m \cdot g}{A_c} + \mu_p \cdot p_4^{(ss)}$$

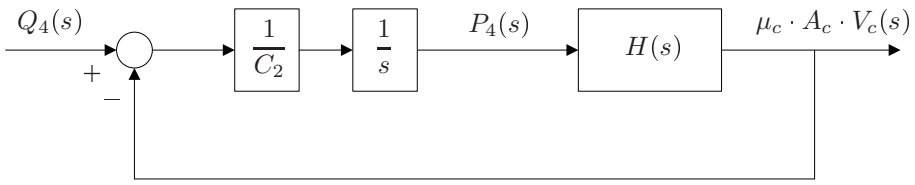

Figure 2.19: Closed loop block diagram

From equation (2.76) the closed loop system is put up as block diagram in Figure 2.19 with input flow and output cylinder velocity. The transfer function block $H(s)$ is computed from equation (2.74), (2.75), (2.77) and (2.78).

$$H(s) = \frac{\mu_c \cdot A_c \cdot V_c(s)}{P_4(s)} = \kappa \cdot \frac{\tau \cdot s + 1}{\frac{1}{\omega_n^2} \cdot s^2 + \frac{2 \cdot \zeta}{\omega_n} \cdot s + 1} \tag{2.81}$$

where

$$\kappa = \mu_c^2 \cdot \left(\frac{K_{qu}}{p_{fo,cbv}} \left(1 + \frac{\mu_p}{\mu_c} \right) + K_{qp} \right)$$

$$\tau = \frac{C_1}{\frac{K_{qu}}{p_{fo,cbv}} \left(1 + \frac{\mu_p}{\mu_c} \right) + K_{qp}}$$

$$\omega_n = \frac{A_c}{\sqrt{C_1 \cdot m}}$$

$$\zeta = \frac{1}{2 \cdot A_c} \cdot \sqrt{\frac{m}{C_1}} \cdot \left(\frac{K_{qu}}{p_{fo,cbv}} + K_{qp} \right)$$

Next, the closed loop transfer function of the system is written by block reduction of the closed loop system in Figure 2.19.

$$\frac{\mu_c \cdot A_c \cdot V_c(s)}{Q_4(s)} = \frac{H(s)}{C_2 \cdot s + H(s)} = \frac{b_1 \cdot s + b_0}{a_3 \cdot s^3 + a_2 \cdot s^2 + a_1 \cdot s + a_0} \tag{2.82}$$

where

$$b_1 = \mu_c^2 \cdot C_1$$

$$b_0 = \mu_c^2 \cdot \left(\frac{K_{qu}}{p_{fo,cbv}} \cdot \left(1 + \frac{\mu_p}{\mu_c} \right) + K_{qp} \right)$$

$$a_3 = \frac{1}{A_c^2} \cdot m \cdot C_1 \cdot C_2$$

$$a_2 = \frac{1}{A_c^2} \cdot m \cdot C_2 \cdot \left(\frac{K_{qu}}{p_{fo,cbv}} + K_{qp} \right)$$

$$a_1 = \mu_c^2 \cdot C_1 + C_2$$

$$a_0 = \mu_c^2 \left(\frac{K_{qu}}{p_{fo,cbv}} \cdot \left(1 + \frac{\mu_p}{\mu_c} \right) + K_{qp} \right)$$

Stability of the system is investigated using Routh-Hurwitz stability criterion. The stability of the closed loop transfer function is, in general, formed by equating the characteristic equation of the denumerator to zero [6, p.112-114]. Routh's array is set up.

s^0	a_0	
s^1	$a_1 - \frac{a_3 \cdot a_0}{a_2}$	
s^2	a_2	a_0
s^3	a_3	a_1

Routh-Hurwitz stability criterion states that for there to be no positive real roots all the coefficients in the characteristic equation must be none zero and have the same sign. If this is true the condition for stability is that all coefficients of the first column of Routh's array have the same sign. The condition for stability lies in the second row of the array.

$$a_1 \geqslant \frac{a_3 \cdot a_0}{a_2}$$

$$\Rightarrow \frac{C_2}{C_1} \geqslant \mu_c \cdot \mu_p \cdot \frac{K_{qu}}{K_{qu} + K_{qp} \cdot p_{fo,cbv}} \tag{2.83}$$

Inserting the linearized flow coefficients in equation (2.79) and equation (2.80) into the stability criterion in equation (2.83) the steady state situation is evaluated.

$$\frac{C_2}{C_1} \geqslant \mu_c \cdot \mu_p \cdot \frac{2 \cdot p_3^{(ss)}}{2 \cdot p_3^{(ss)} + u_{cbv}^{(ss)} \cdot p_{fo,cbv}} \tag{2.84}$$

The steady state pressure $p_3^{(ss)}$ is found from a steady state situation of equation (2.69).

$$p_3^{(ss)} = p_4^{(ss)} \cdot \mu_c + \frac{m \cdot g}{A_c} \tag{2.85}$$

Normally the opening of the CBV, u_{cbv}, is much less than 1. For high pressure levels and low flows the fraction in equation (2.84) is approximately 1 and the stability criterion is simplified. Rewriting the capacitances and neglecting line volumes and cylinder dead volumes, the approximated stability criterion yields the following equation.

$$\frac{C_2}{C_1} \geqslant \mu_c \cdot \mu_p \tag{2.86}$$

$$\Rightarrow x_c \leqslant \frac{1}{1 + \mu_p} \cdot s_c \tag{2.87}$$

For $\mu_p = 1$ the system is unstable when $x_c > \frac{s_c}{2}$. Higher pilot area ratio makes the system unstable for greater length of stroking. The conclusion drawn from this analysis is that the stroking length of instability increases with high pressure levels, high pilot area ratio and small flows.

Chapter 3

Modeling and Simulations

Modeling and simulation of both the mechanical and hydraulic systems are performed by the use of SimulationX, which is a fraphical commercial simulation software. In SimulationX simulation models are built by connecting predefined blocks to each other in a block diagram view. The block's parameters are defined by the user (e.g. the diameter of a hydraulic valve or the resistance of a resistor).

In order to verify the simulations performed in SimulationX the equations derived in chapter 2 were numerically time integrated in MATLAB. The results of the time integrations were then used to verify the results of the simulations.

3.1 Modeling of the Mechanical System

The mechanical system is modeled by the use of the *MBS Mechanics* library which allows 3-dimensional multi-body-systems (MBS) simulations. For the task the use of the 2-dimensional *Planar Mechanics* library would have been sufficient, but a license for this library was not available. In the modeling of the mechanical system the cylinder friction is not taken into account.

For the simulations in this chapter the lengths used are $l_1 = 600$ mm and $l_2 = 300$ mm.

3.1.1 Rigid Beam Model

The mechanical system is initially modeled with a rigid beam in order to be able to verify the kinematics and kinetics by the use of time integration of equations in MATLAB. Figure 3.1 shows the model of the rigid beam in SimulationX.

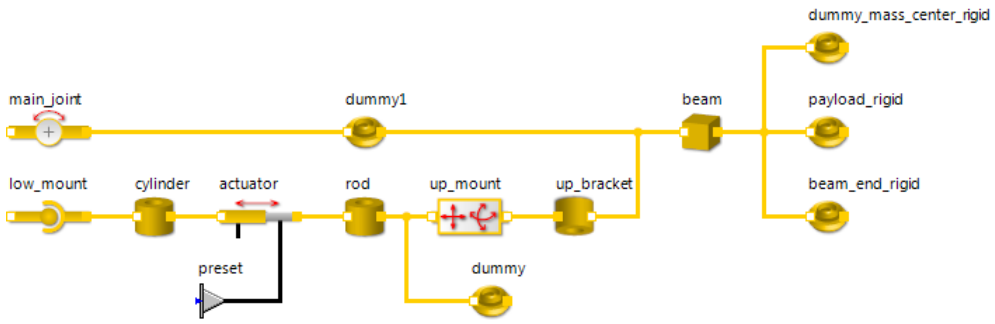

Figure 3.1: The rigid beam in SimulationX

The model is built up bodies, joints and constraints connected to each other. Starting in the lower half of Figure 3.1, *low_ mount* is a spherical joint representing the lower cylinder mount, and allows rotation around all axes. The next three elements represents the cylinder; *cylinder* represents the cylinder, *rod* represents the rod, and *actuator* is a prismatic joint which connects the cylinder bodies to each other and allows a

translational motion between them along one axis. The actuator's displacement, velocity or acceleration can be set by the preset conveniently called *preset*. The constraint, *up_ mount*, is representing the upper cylinder mount, and is connecting the cylinder to the upper bracket, *up_ bracket*. The constraint's translational and rotational constraints are user defined. In this case is the constraint set to fixed in all translational directions in addition to any rotation around the y-axis. Rotation around the x-axis and z-axis is allowed. The beam's main joint is represented by *main_ joint* which is a revolute joint allowing rotation around the z-axis. The beam itself is represented by the body *beam* where mass and dimensions are defined. The payload is represented as a point mass by *payload_ rigid*, and is placed in the coordinates of the actual payload's center of mass. The remaining bodies are dummy bodies (very small masses which are negligible) which are used for either manipulation or monitoring purposes (in order to be able to monitor a coordinate's position etc. must either a body or a sensor be placed in the particular coordinate). While using the *MBS library* the model is subjected to gravitational acceleration by default.

Figure 3.2 and Figure 3.3 shows comparisons between analytically derived and simulated main joint angles and cylinder force respectively. As seen in the figures, there is no deviation between the analytic and simulated model. A larger selection of comparisons between the analytic model and the simulated model can be found in appendix B.1. In the comparisons are the lengths l_1 and l_2 are set to 0.6 m and 0.3 m respectively. The cylinder stroke is increased from 0 to 500 mm (full cylinder stoke) with a velocity of 0.1 $\frac{\text{m}}{\text{s}}$, which means that the x-axes of the plots ranging from 0 s to 5 s are analogous to 0 mm to 500 mm cylinder stroke.

θ_1 and θ_2:

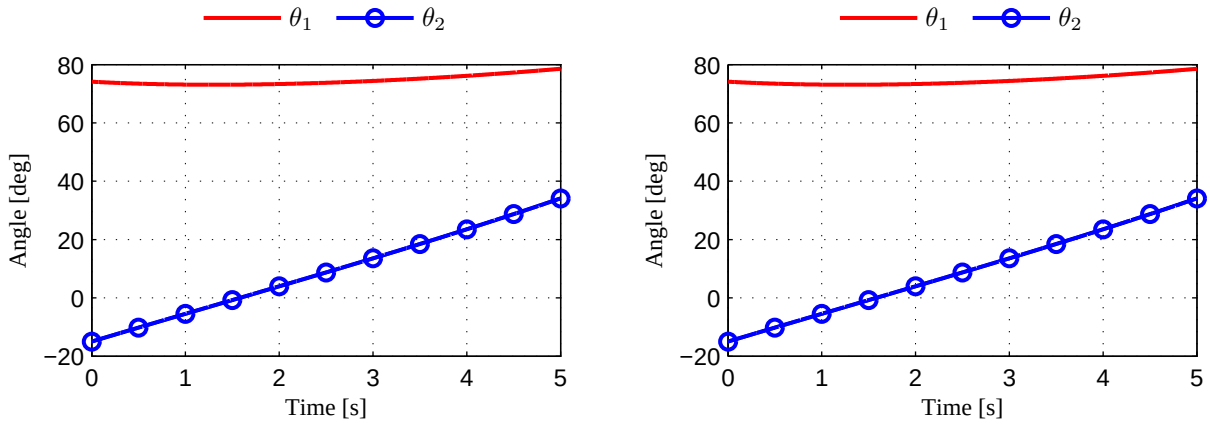

(a) Analytically derived

(b) Simulated

Figure 3.2: Plots of analytically derived and simulated angles

Cylinder force:

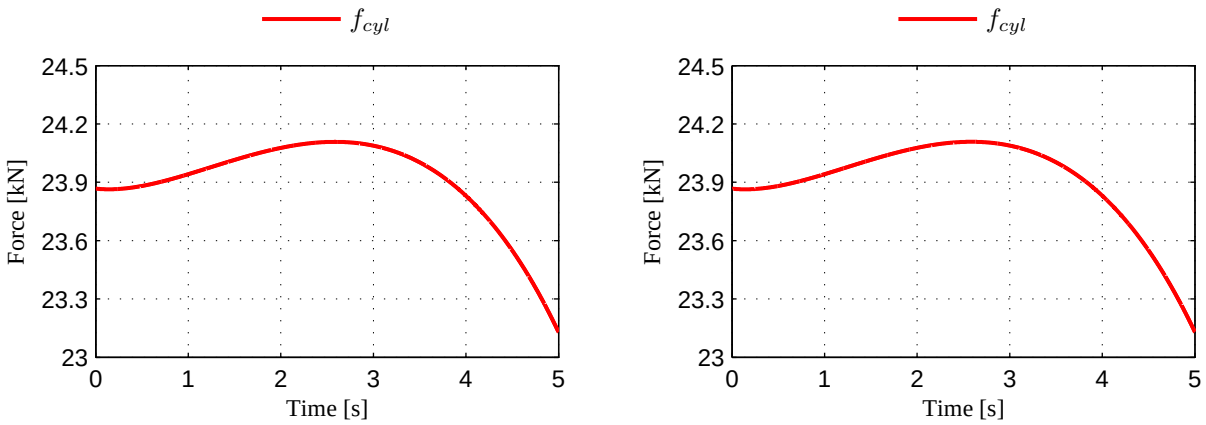

(a) Analytically derived

(b) Simulated

Figure 3.3: Plots of analytically derived and simulated cylinder force

3.1.2 Flexible Beam Model

In order to include the beam's dynamics in the simulation, the lumped beam model discussed in subsection 2.1.4 is implemented in the simulation model. By introducing beam dynamics in the simulation, the beam's influence on the hydraulic system becomes more realistic due to the introduced stiffness and damping.

As shown in Figure 3.4 the flexible model is very similar to the rigid model shown in Figure 3.1. The difference between the models is that the single beam in the rigid model is divided into sections connected by rotational joints, springs and dampers in the flexible model. The coefficients of the force elements are described in subsection 2.1.4.

The accuracy of a lumped beam model depends on how many sections it is divided into. A high number of sections yields a high accuracy, but also results in a high computational time. In order to determine the number of sections to divide the beam into, simulated experiments are performed in SimulationX, and verified by analytic calculations performed in MATLAB. The measure of accuracy used is the static deflection of the beam's end in y-direction.

In MATLAB the beam's static deflection is calculated by integration of bending moment, see subsection 2.1.3. In SimulationX lumped beam models are simulated under the same static conditions as in MATLAB. The lengths l_1 and l_2 are set to 0.6 m and 0.3 m respectively. The cylinder length, l_{cyl}, is set to to 0.93 m, which results in an approximately horizontal beam ($\theta_2 \approx 0°$), which is when the deflection in y-direction is largest. The payload is modeled as a point mass with a mass equal to 382.6 kg (all available weights in the physical experiment). The point mass is placed -80 mm in x-direction and 70 mm in y-direction (h_{pl}) with respect to the center of the beam's end. See Figure 2.1 for .

In the experiments performed in SimulationX the beam is divided into 3 main parts; part I which is the part prior to the main joint, part II which is the part between the main joint and the cylinder mount, and part III which is the part from the cylinder mount to the end of the beam, see Figure 3.5. Part I is assumed rigid at all times, while part II and III are to be simulated non-rigid. Three sets of simulated experiments are performed. First a single experiment with both part II and part III divided into a relatively high number of sections is performed in order to verify the use of a lumped beam model. Then experiments with part II rigid and part III non-rigid in otder to determine the required number of sections to divide part III into. In the last experiment is both part II and III non-rigid in order to determine the number of sections required to divide part II into. In this experiment is part III modeled with the number of sections found in the second experiment.

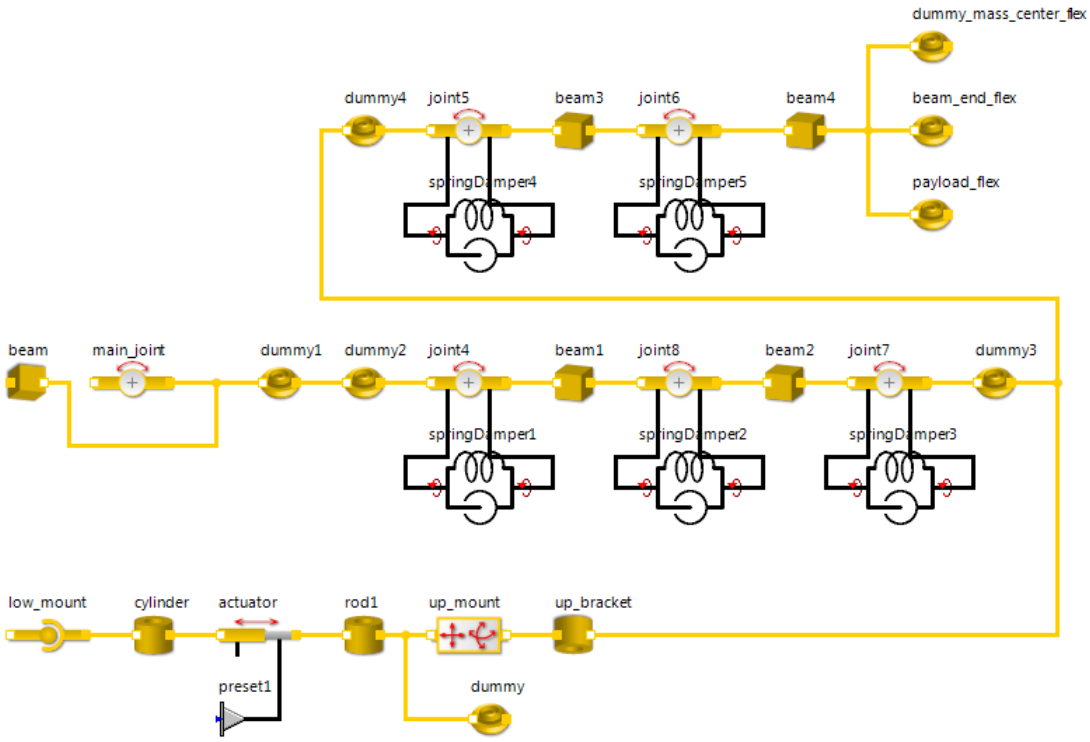

Figure 3.4: The flexible beam in SimulationX - *here illustrated with the beam divided into five sections; one prior to the main joint, two between the main joint and the upper cylinder mount, and two after the upper cylinder mount.*

Figure 3.5: Main parts of the beam - *Part I is the part prior to the main joint, part II is the part between the main joint and the upper cylinder mount, and part III is the part from the upper cylinder mount to he end of the beam.*

Experiment I

In the first experiment are part II and part III divided into 15 sections each. The experiment resulted in a deflection in y-direction at the beam's end equal to 22.0252 mm. The calculation in MATLAB gave 22.2900 mm, which is 0.2648 mm more. In SimulationX the cylinder mount is displaced due to the deflection of the beam, while the mounting is a rigid boundary condition in the analytic approach. The conclusion of the experiment is therefore that a simulation of a lumped beam in SimulationX yields a realistic result.

Experiment II

In the second experiment the goal is to reduce the number of sections of part III of the beam from 15 (used in experiment I) to as few as possible, but still maintain a sufficient accuracy. To achieve this, part II of the beam is modeled rigid while part III is modeled non-ridig. Successive experiments are performed where the number of sections part III is divided into is increased from 1 to 15 while the deflection of the end in y-direction is logged. Thereafter the derivative of the deflection, which describes the rate of change in deflection, is calculated numerically. The deflections are then compared with the deflection calculated in MATLAB under the same conditions (a cantilever beam with the length of part III under same load conditions).

As seen in Figure 3.6a the deflection simulated in SimulationX is converging to the deflection calculated in MATLAB while the number of sections is increasing. It is assumed that the accuracy of the model is sufficient when the derivative is less than one quarter of a millimeter per number of sections. With a number of sections equal to 5 the derivative is equal to $-0.2332\frac{\text{mm}}{\text{no. sec}}$, see Figure 3.6b. At this point the deflection in SimulationX is equal to 19.2266 mm, which gives a deviation between SimulationX and MATLAB equal to 2.1 % (with MATLAB as reference). This deviation is assumed to be acceptable, and part III of the beam is therefore divided into 5 sections.

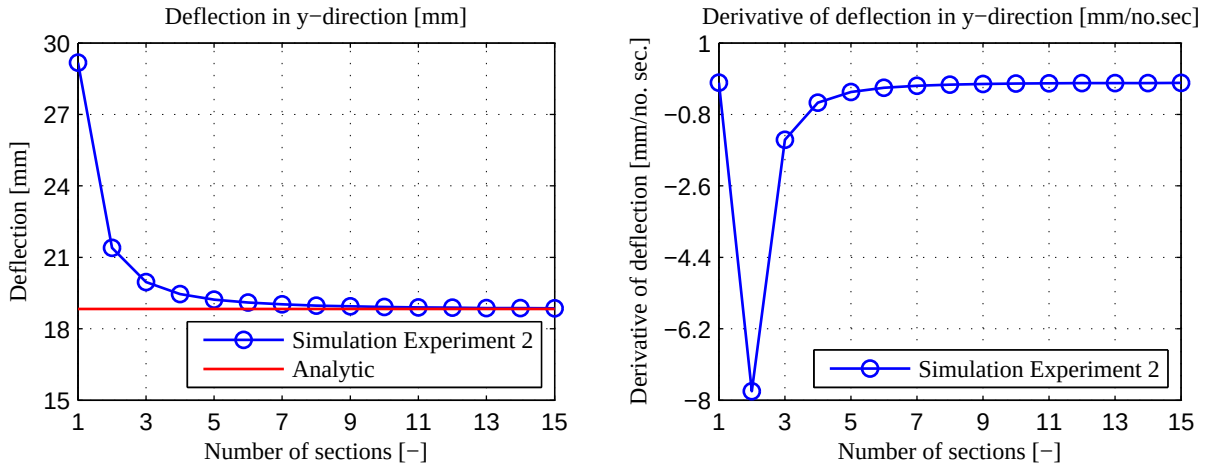

(a) Deflection in y-direction

(b) Derivative of deflection in y-direction

Figure 3.6: Plots of beam part III's deflection and it's derivative vs. the number of sections the part is divided into simulated in SimulationX - *the deflection in SimulationX compared with the deflection calculated in MATLAB which is calculated to 18.83 mm.*

Experiment III

In the third experiment the goal is to reduce the number of sections of part II. The number of sections of part II is increased while the deflection in y-direction is logged. The number of sections of part III is set to 5 due to the results of experiment II.

The plots of the beam's deflection and it's derivative are shown in Figure 3.7. As seen in Figure 3.7a is the deflection converging to a larger level than the results from both the analytic and simulated results in experiment I. The is because the number of section of beam part III is set to 5 (experiment II), which yields in a larger deflection. The criteria to determine how many sections part II should be divided into is the same as in experiment II; the derivative should be less than a quarter of a millimeter per number of sections. It can be seen in Figure 3.7b that this criteria is fulfilled with 4 sections or more (the derivative with 4 sections is $0.1295\frac{\text{mm}}{\text{no. sec}}$).

With part I of the beam assumed stiff, part II divided into 4 sections, and part III divided into 5 sections is the simulated static deflection equal to 22.2267 mm. This gives a deviation with respect to the analytic and simulated results in experiment I equal to -0.28 % and 0.91 % respectively. A deviation less than 1 % is considered sufficient.

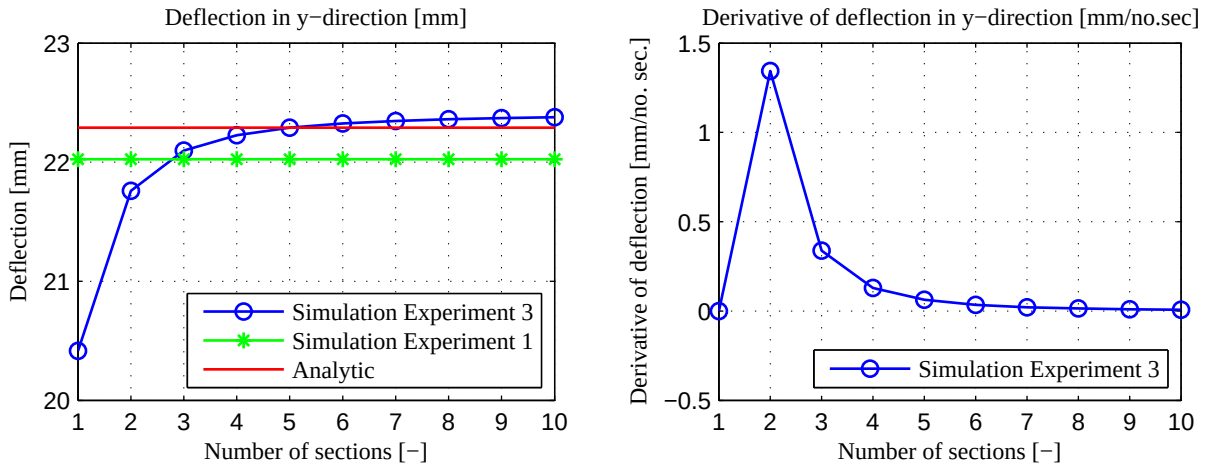

(a) Deflection in y-direction

(b) Derivative of deflection in y-direction

Figure 3.7: Plots of the beam's deflection with beam part III divided into 5 sections, and the number of sections of beam part II increased from 1 to 10 sections - *the simulated deflections in experiment 3 are compared with the simulated and analytic deflection from experiment 1.*

Note: There were performed simulated experiments where the beam was only divided into 2 main parts; a stiff part prior to the main joint, and a part non-rigid part spanning from the main joint to the end of the beam. The experiments were performed as the experiments described above; the deflection in y-direction was logged while the number of sections the part was divided into was increased, see Figure 3.8. By looking at both Figure 3.8a and Table 3.1 it can be seen that the deflection is depending on how close to a section end the cylinder mount is. The cylinder mount is at all times placed 0.59 m from the main join in x-direction, while on which section it is placed depends on how many sections the part of the beam is divided into. The peaks seen at the number of sections equal to 6, 12 and 18 in Figure 3.8a can be traced to when the distance between the cylinder mount's distance to the end of the section it is placed on is small. This problem was solved by ensuring that the cylinder mount always was placed between two sections (as in experiment I, II and III).

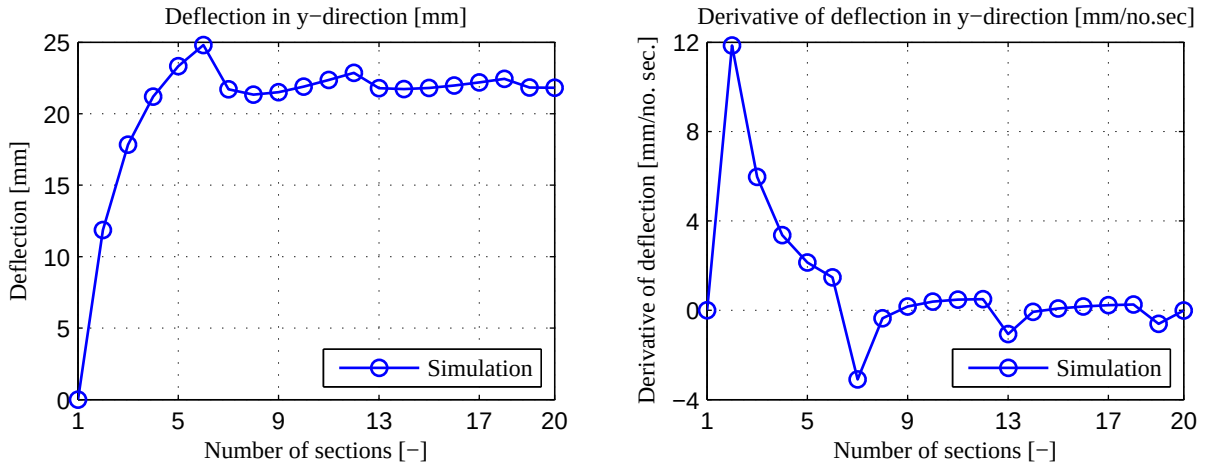

(a) Deflection in y-direction

(b) Derivative of deflection in y-direction

Figure 3.8: Plots of the beam's deflection and it's derivative with the beam's flexible part spanning from the main joint to the end - *the number of sections the flexible part is divided into is increased from 1 to 20.*

Table 3.1: The cylinder mount's section placement

No. of sections	Length of sections	Cyl. mount placed on section no.	Distance from cyl. mount to end of section placed
1	3.600	1	3.010 m
2	1.800 m	1	1.210 m
3	1.200 m	1	0.610 m
4	0.900 m	1	0.310 m
5	0.720 m	1	0.130 m
6	**0.600 m**	**1**	**0.010 m**
7	0.514 m	2	0.439 m
8	0.450 m	2	0.310 m
9	0.400 m	2	0.210 m
10	0.360 m	2	0.130 m
11	0.327 m	2	0.065 m
12	**0.300 m**	**2**	**0.010 m**
13	0.277 m	3	0.241 m
14	0.257 m	3	0.181 m
15	0.240 m	3	0.130 m
16	0.225 m	3	0.085 m
17	0.212 m	3	0.045 m
18	**0.200 m**	**3**	**0.010 m**
19	0.189 m	4	0.168 m
20	0.180 m	4	0.130 m

3.2 Modeling of the Hydraulic System

The hydraulic system is modeled using the hydraulics library in SimulationX. The oil properties are many, like gas fractions, temperature, bulk modulus, viscosity and density. Not all of these properties are taken into account in the analytic model. For the part of verification the properties whom allows it are set constant, and those properties required for the valve characteristics reference measurements (oil density and viscosity) are assumed equal for both models.

In the analytic model the restriction flows are based on stationary volume flow, meaning the volume flow in to the restriction is equal to the volume flow out of it. That implies a constant oil density. In reality the density depends on temperature and pressure. For a physical system the volume flow out of the restriction is slight greater than the volume flow sent in. The reason is that when a constant volume is pressurized it becomes stiffer, which increases the density. After the restriction the pressure is reduced and thereby the density is reduced, hence increasing the volume for the same amount of mass. The mass flow is stationary, meaning that when the density decreases the volume flow have to increase ($dm = \rho \cdot dV$). SimulationX calculates mass flow which gives the realistic picture of the physical system.

Valve blocks in SimulationX have several options to describe the characteristics of the valve. A convenient way, and the one preferred, of describing the valve characteristics is to generate the characteristics curve using the *Data Table* option. The curve is generated by using *SimulationX Curve Editor* to load characteristic data generated form the equations in section 2.2. The characteristic of a valve, using Data Table, is pressure drop vs flow or flow vs spool position. For the pressure drop vs flow characteristics the flow dependency on the oil properties is neglected. The flow through these valves are proportional to the valve opening. Flow vs spool position characteristic valves require reference measurements such as pressure drop, density and viscosity. These valves consider both laminar and turbulent flow, where as the analytic

model assumes pure turbulent flow.

3.2.1 Modeling and Verification of Components

The hydraulic system is verified by comparing valve characteristics from SimulationX to the analytic valve characteristics described in section 2.2. All volumes in the simulations are 5 cm^3, with rigid walls. The fluid used is HLP46 with constant temperature of 40 °C and without gas fractions.

PCV:

The PCV is modeled using a normally open, pilot operated pressure relief valve. The characteristics of the valve given in Figure 2.12 in subsection 2.2.1 is used as the characteristics for the relief valve. The valve is fully open for the verification of the characteristics, therefore the pilot pressure ports are connected to the tank side. One would expect no mention worthy deviation from the analytic model as the temperature is constant and the pressure drop across the valve is small, giving close to stationary volume flow.

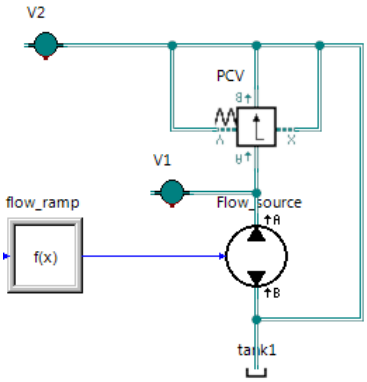

Figure 3.9: PCV verification model

In Figure 3.9 the simulation modeling of the verification of the PCV is shown. The flow source is ramped up from 0 to 100 $\frac{l}{min}$ in 5 sec.

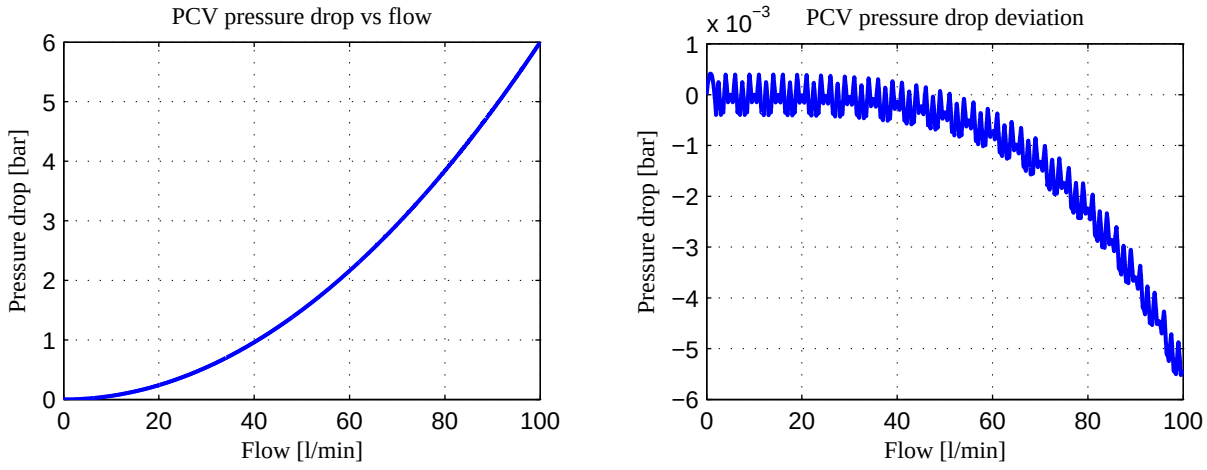

(a) Pressure drop vs flow

(b) Pressure drop deviation

Figure 3.10: PCV pressure drop vs flow simulated

The pressure drop vs flow characteristics of the valve is shown in Figure 3.10a. Deviation from the analytic model is, as expected, close to zero as seen in Figure 3.10b (note that the values on the pressure drop axis is multiplied 10^{-3}) and accepted as a valid representation of the PCV.

DCV:

The DCV is modeled for verification as a shorted circuit consisting of the main spool and the PCV. Leakages in the valve block are also modeled. Eventually deviation between the simulation model and the analytic model will be corrected for to ensure that the DCV is able to deliver 25 $\frac{\text{l}}{\text{min}}$.

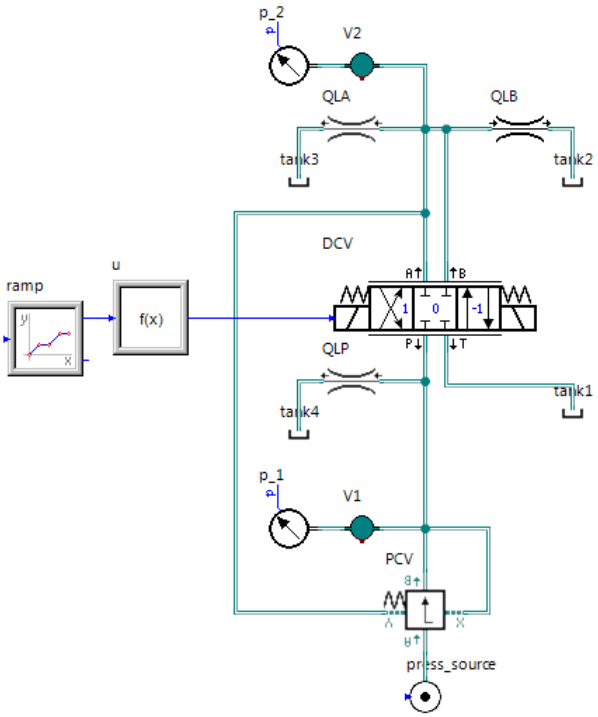

Figure 3.11: DCV verification model

The shorted circuit in Figure 3.11 is supplied with a pressure source of 20 bar. The flow vs spool position characteristic of the DCV is the same as in Figure 2.13 with reference pressure drop of 7.72 bar and default oil density and viscosity (890 $\frac{\text{kg}}{\text{m}^3}$ and 41 cSt). The main spool opening, u, is ramped up from 0 to 1 in 5 sec.

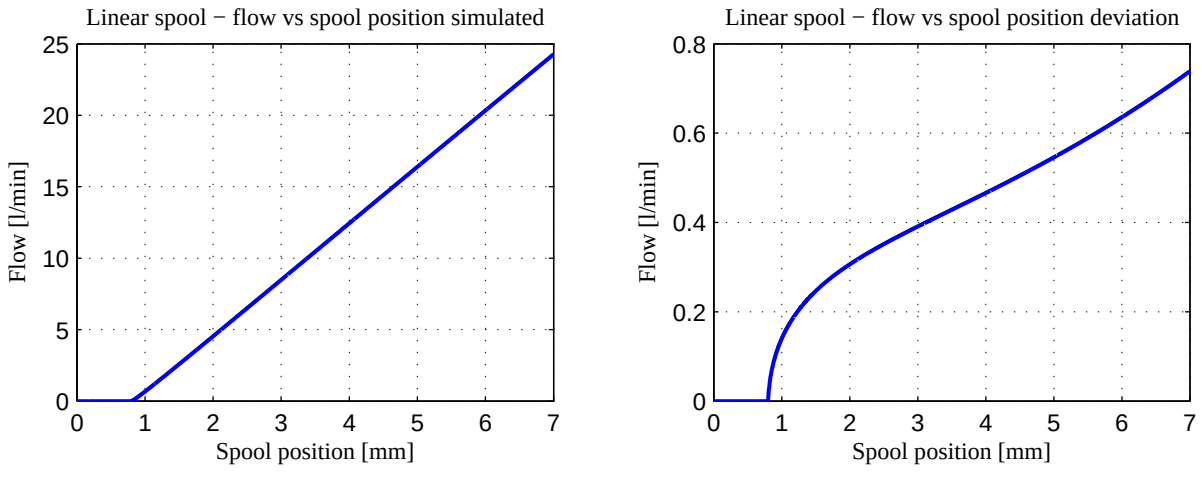

(a) Flow vs spool position

(b) Flow deviation

Figure 3.12: DCV deviation - *between simulation model and analytic model*

In Figure 3.12a the flow vs spool position characteristics of the main spool is shown. From Figure 3.12b the deviation from the analytic model (deviation = analytic - simulated) is seen to be approximately 0.75 $\frac{\text{l}}{\text{min}}$.

The majority of the deviations are not caused by leakage flow due to the low pressurized system, but may be caused by the inconsistency between the models as described in the section intro. The deviation is reduced by decreasing the pressure drop reference for the DCV characteristics.

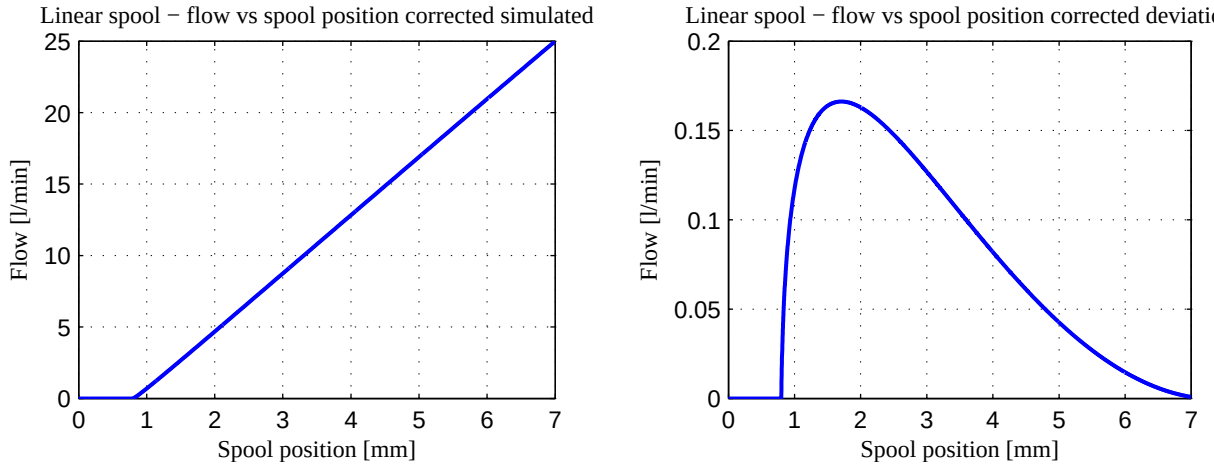

(a) Corrected flow vs spool position

(b) Corrected flow deviation

Figure 3.13: DCV corrected deviation - *between simulation model and analytic model*

The reference pressure drop is now 7.272 bar. In Figure 3.13b it is seen that the deviation when the spool is fully open is zero, meaning the fully open valve flow is 25 $\frac{\text{l}}{\text{min}}$ as seen in Figure 3.13a. The deviation between the two models during ramping is caused by the analytic model has a pure linear relation between flow and spool opening, while it can be observed (not shown) that the simulated model has a parabolic shape for small openings. There is no way to determine the exact shape of the flow vs spool opening characteristics from the data sheet for the valve, other than the rated flow and the general shape of the characteristics. Therefore the result, with a maximum deviation of approximately 4 %, is accepted as an valid representation of the DCV.

CBV:

The load holding valve and the check valve are modeled as two separate variable throttle valves. The characteristics of the valves given in Figure 2.16 in subsection 2.2.2 are used as the characteristics for the throttle valves. The opening of the valves are given by equation (2.56) and equation (2.55), but for verification of pressure drop vs flow characteristics they are set to 1 and 0 depending on which valve characteristics that is simulated.

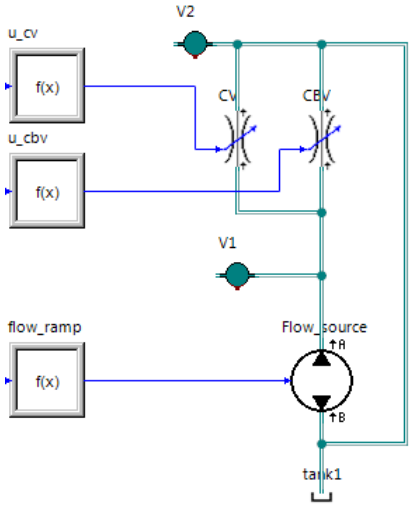

Figure 3.14: CBV verification model

In Figure 3.14 the simulation modeling of the verification of the CBV is shown. The flow source is ramped up from 0 to 60 $\frac{\text{l}}{\text{min}}$ in 5 sec.

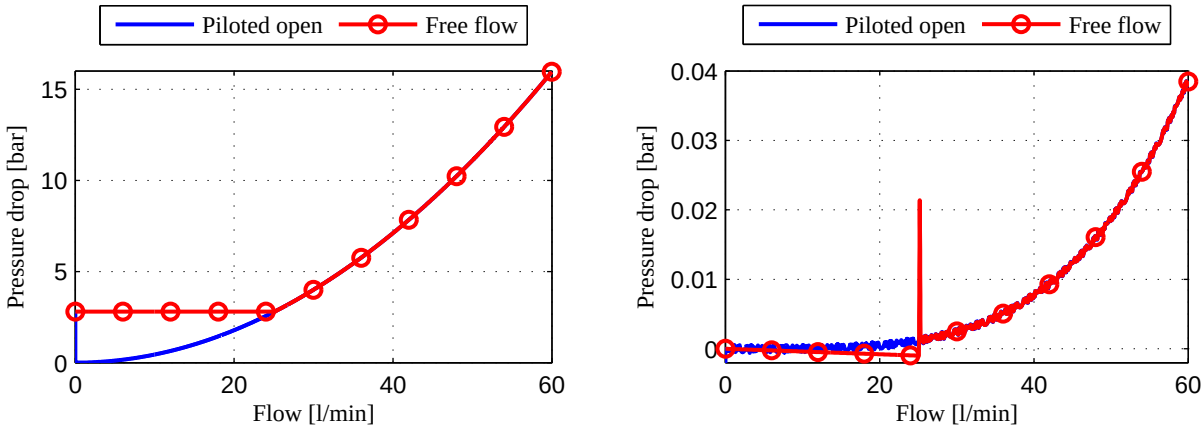

(a) Pressure drop vs flow

(b) Pressure drop deviation

Figure 3.15: CBV deviation - *between simulation model and analytic model*

The pressure drop vs flow characteristics of the two valves is shown in Figure 3.15a. Deviation from the analytic model is seen in Figure 3.15b. The red spike in the free flow deviation plot occurs in the transition from constant to parabolic pressure drop, meaning than the characteristics in the simulation valve turns to the parabolic shaped curve before the analytic model does. Maximum deviation between the models is found at the spike and is less than 1 % of the pressure drop in this point (2.8 bar). With deviations being close to zero the model is accepted as a valid representation of the CBV.

3.2.2 Hydraulic System Simulation Model

The DCV is corrected to give the desired flow of 25 $\frac{\text{l}}{\text{min}}$, and the PCV and CBV characteristics are verified. Now the entire hydraulic simulation model is put up.

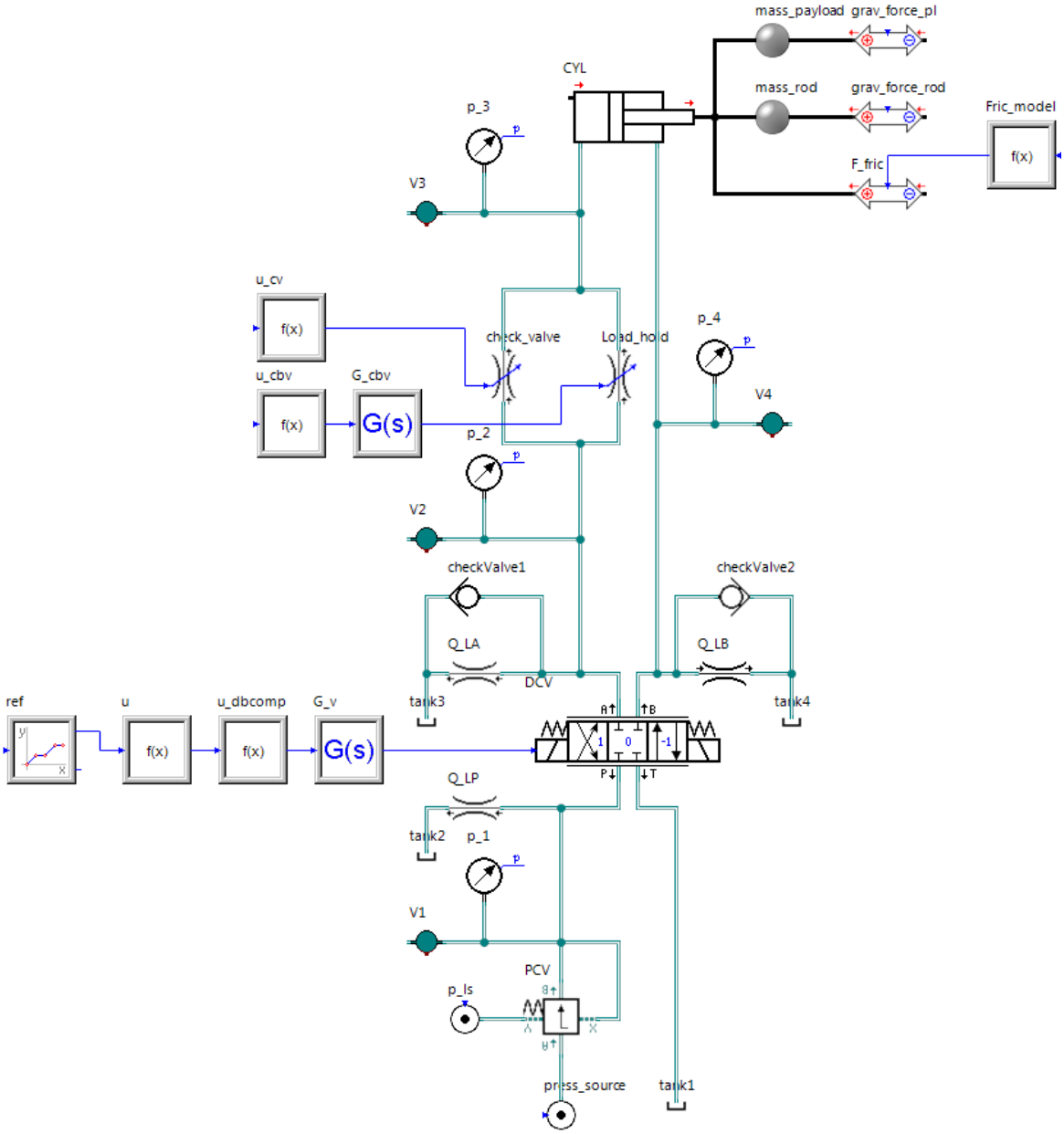

Figure 3.16: Hydraulic system simulation model

In Figure 3.16 the hydraulic system simulation model is shown. It consists of a pressure source supplying the system with 200 bar and unlimited flow. The pressure compensator valve, derived in the previous subsection, retrieves the opening pressure, p_x, from a pressure source which gives the pressure p_2 or p_4 depending on the direction of the main spool. The cylinder is modeled without internal friction and leakage, and friction model derived in equation (2.65) in subsection 2.2.3 is added as an external force to the cylinder rod. The payload mass and force are constant and will later be replaced with the model of the flexible arm. Valve dynamics of the main spool and the counterbalance valve are added as transfer functions with input from the desired opening and outputs the actual opening. The pressure transducers used in the physical model has a reaction time of 1 ms, which is much lower than the data sampling time. Time delay in the pressure sensors are therefor neglected and the feedback pressure (p_4) is taken directly from the pressure in line 4. The flow sensor is not included in the simulation model as it is not used as a feedback to the control system.

3.3 Simulation Results

In this section the simulation model is evaluated by means of comparing the models with and without flexibility in the beam and dynamics in the valves. The three first plots are generated from simulations on the model using a rigid boom, and the rest of the plots compares the use of rigid boom and flexible boom.

The path of the reference spool opening $u^{(ref)}$ is given in Figure 3.17 and is used for all the plots in this section. Note that a negative spool opening gives a positive flow and vice versa due to different definition of positive and negative opening direction in SimulationX and the theoretical equations. The dynamic of the valve is not compared, as the first order transfer function is independent to the pressures and only depends on the reference opening $u^{(ref)}$. The result of the transfer function is a delay in the response.

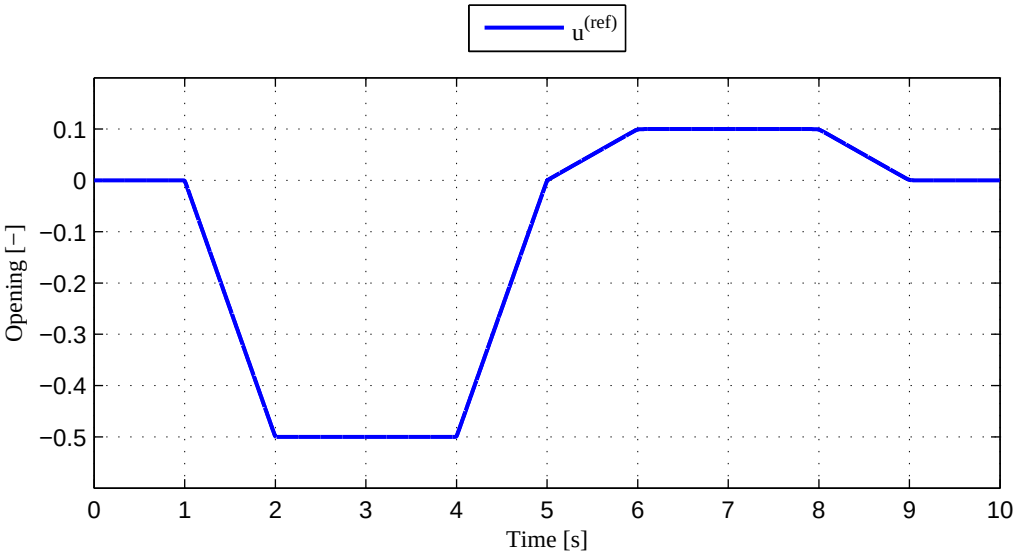

Figure 3.17: Simulation model dynamics of DCV

In Figure 3.18 the load holding valve is plotted using the rigid boom both with a dynamic valve opening ($u_{cbv,dyn}$) and without dynamic valve opening ($u_{cbv,stiff}$). The eigenfrequency used for the load holding valve in these simulations is $\omega_{cbv} = 63\ \frac{\text{rad}}{\text{s}}$. The dynamic valve is seen to have less fluctuations, thus reducing the system stiffness.

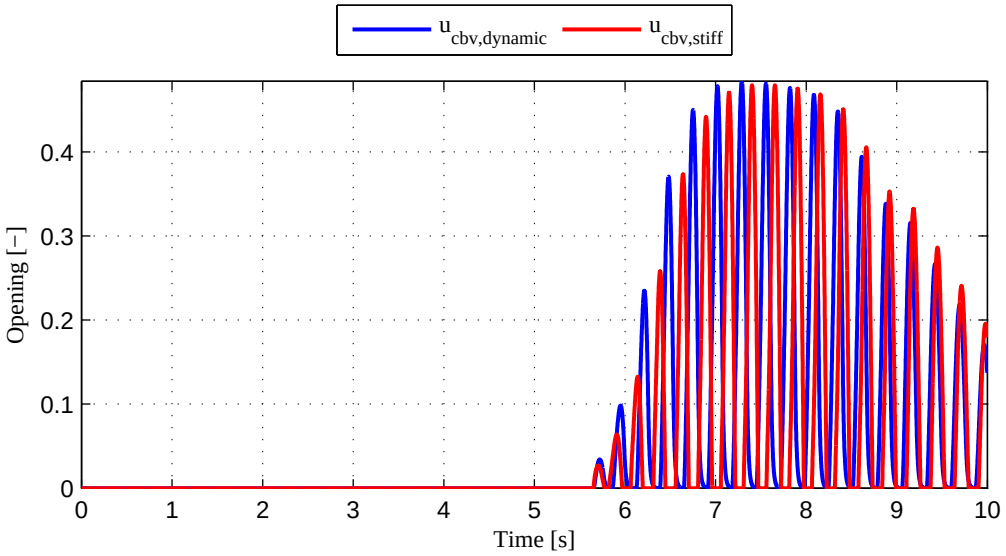

Figure 3.18: Simulation model dynamics of CBV

In Figure 3.19 the flows in and out from the DCV is shown using the rigid boom model. For a cylinder out-stroke (first 5 sec) the in-flow, Q_2, is seen to follow the ramp input given by the valve opening $u^{(ref)}$. The in-flow for cylinder in-stroke (after 5 sec), Q_4, also follows the desired ramp path, but there are some fluctuations due to instabilities that now occurs in the system.

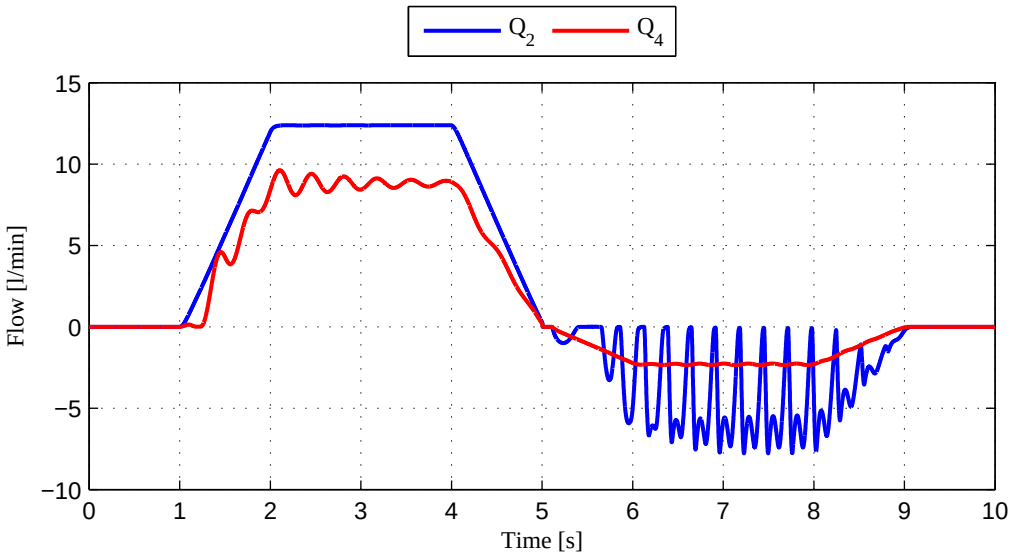

Figure 3.19: Simulation model in and out flow from the DCV

The pressure in the high pressurized cylinder chamber, p_3, in the rigid boom and flexible boom model is shown in Figure 3.20. The flexible boom is seen to give a more damped system with a lower natural frequency than the rigid boom, which is also observed for the low pressurized chamber in Figure 3.21. It is seen that the amplitude of pressures for cylinder in-stroke is amplified as the time progresses indicating an unstable system.

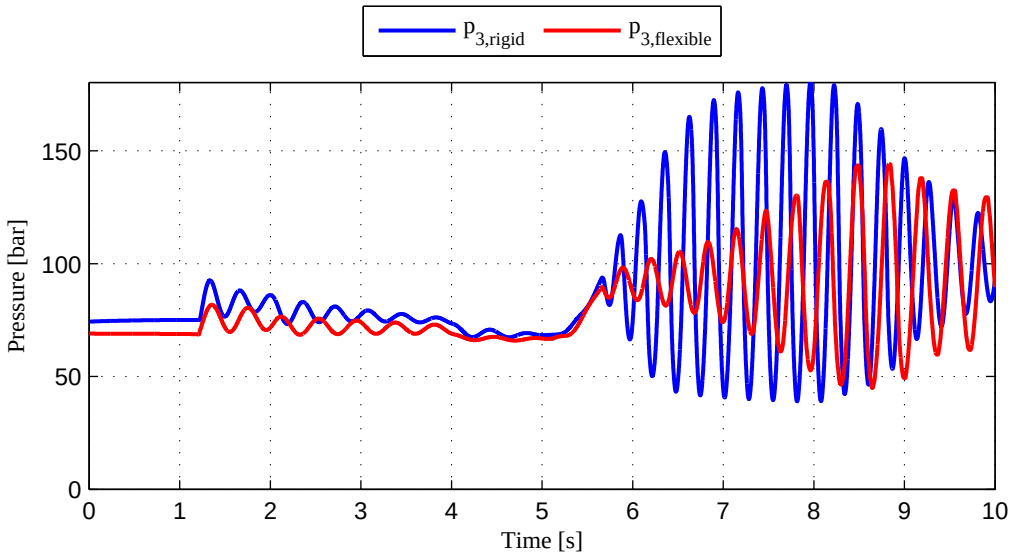

Figure 3.20: Simulation model high pressurized cylinder chamber p_3 - *comparing simulation models with rigid and flexible boom*

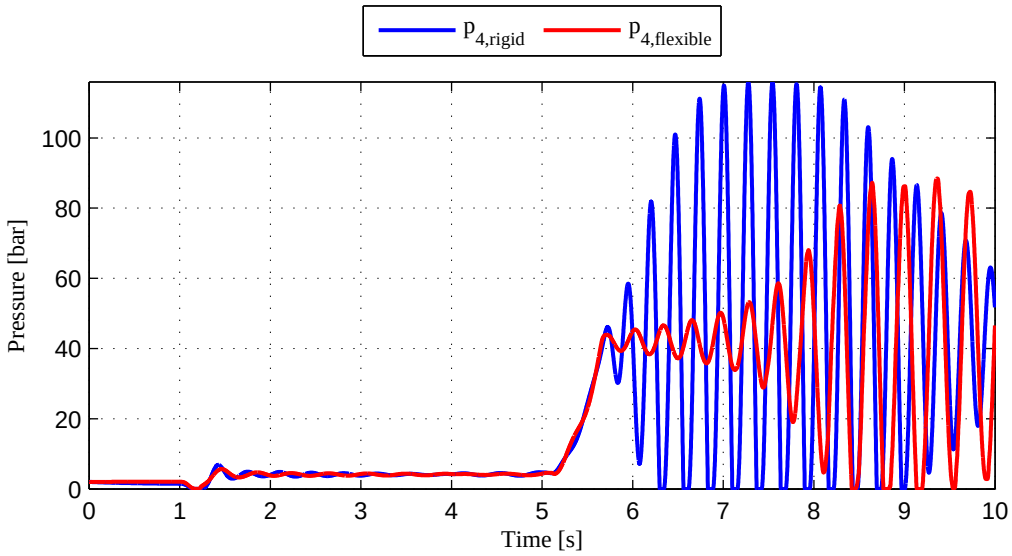

Figure 3.21: Simulation model low pressurized cylinder chamber p_4 - *comparing simulation models with rigid and flexible boom*

In Figure 3.22 the check and load holding valve openings are shown. The same observations that is seen from the pressures is seen for the CBV openings, as the openings are directly driven by the pressures.

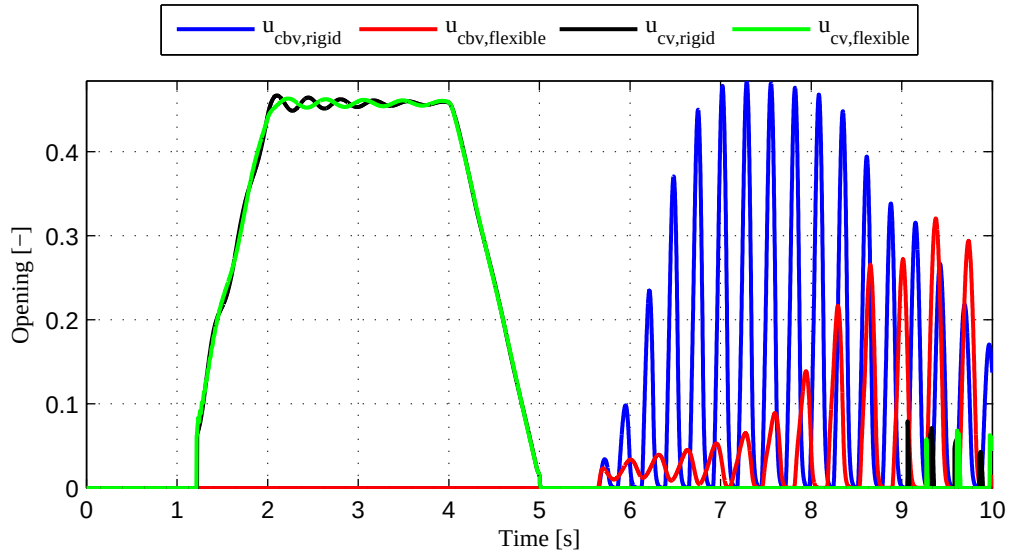

Figure 3.22: Simulation model counter balance valve opening - *comparing simulation models with rigid and flexible boom*

The velocity of the cylinder is plotted in Figure 3.23. Same observations as mentioned for the pressures is also seen here.

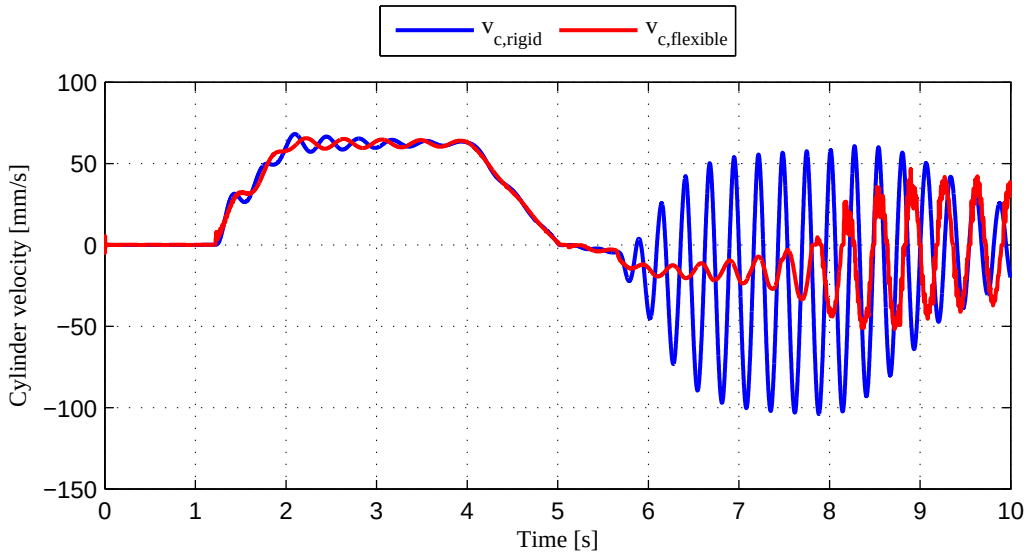

Figure 3.23: Simulation model cylinder velocity - *comparing simulation models with rigid and flexible boom*

In Figure 3.24 the friction force is shown. The friction model in (2.65) is used. By comparing with the velocity plot above it is seen that the direction of the friction force changes with the change in velocity direction. Positive velocity results in a negative friction force and a negative velocity results in a positive friction force.

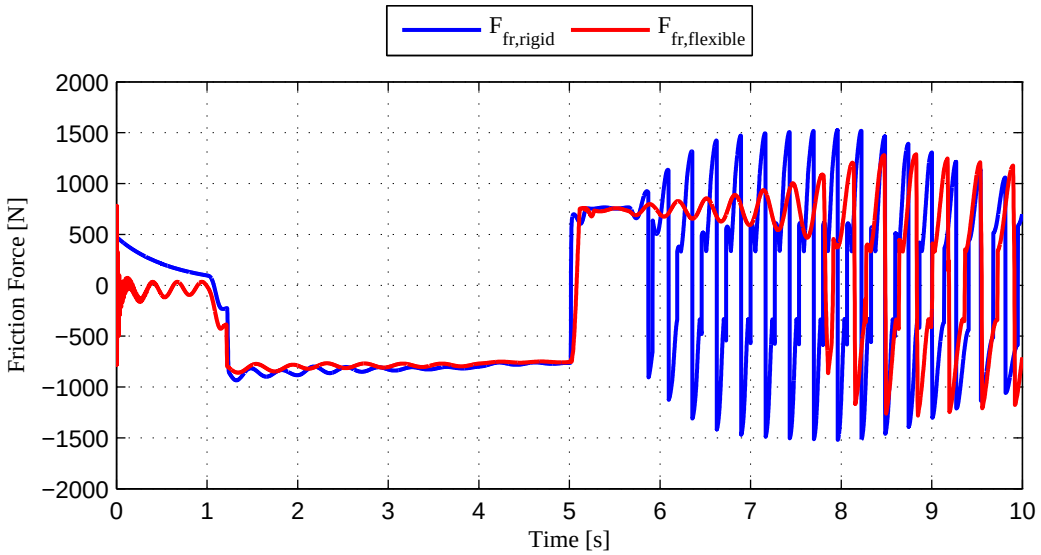

Figure 3.24: Simulation model friction force - *comparing simulation models with rigid and flexible boom*

The comparison of the model using rigid and flexible boom shows that the flexible boom makes the system slower and more damped than the rigid boom. Including load holding valve dynamic also makes the system slower. In chapter 5 the simulation model is verified by comparing results with the physical test rig.

Chapter 4

Experimental Setup

The mechanical, hydraulic and instrumentation design of the test rig was designed by the project supervisors. The assembly was completed midway in the project. In this chapter the hydraulics and instrumentation of the experimental setup is described. The mechanical system is described in chapter 2, and therefore not elaborated further in this chapter. In Figure 4.1 are pictures of the test rig shown.

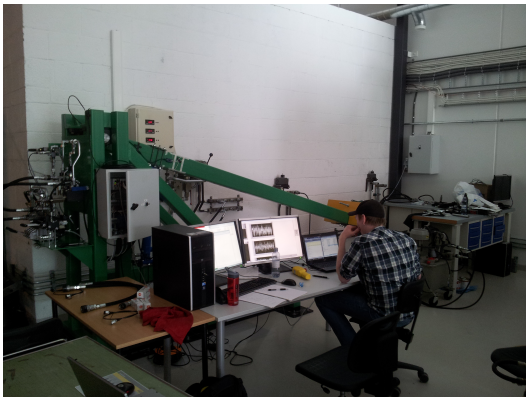

(a) Overview of the experimental setup

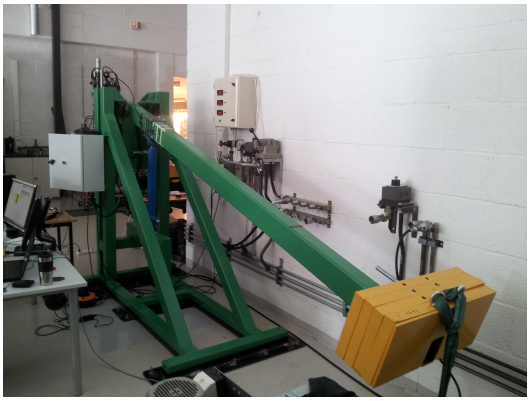

(b) The mechanical system of the experimental setup

Figure 4.1: Pictures of the experimental setup

4.1 Hydraulic System

The components of the hydraulic system are described in this section. A picture of the test rig' hydraulics is shown below.

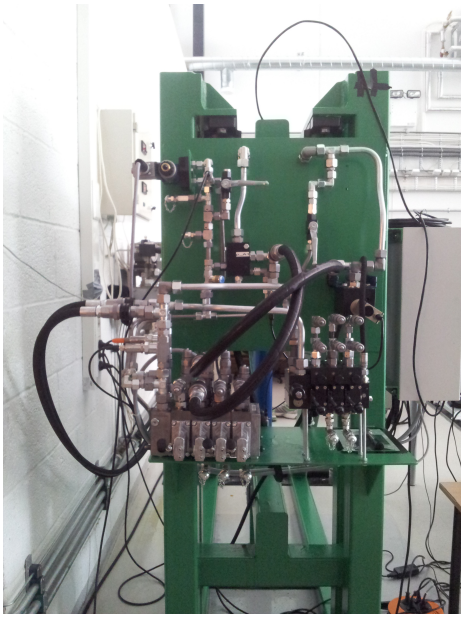

Figure 4.2: Hydraulic system experimental setup

4.1.1 Directional Control Valves

A proportional valve group, PVG 32 from Sauer Danfoss, is used for flow control. The valve group consists of a pump side module (PVP) and four basic modules (PVB) for flow control. Three of the PVB's are pressure compensated, giving near constant pressure drop across the main spool of 7 bar. The main spools all deliver 25 $\frac{\text{l}}{\text{min}}$, but have different specifications on bore and flow characteristics (linear/standard). The spools can be actuated both manually and electrically. For the purpose of this project the electrically actuation is used.

Table 4.1: Directional control valve specifications

Valve no.	**PVB**	**Main spool**	**Rated flow**	**LS setting**
1	Load drop check valve	FC spool with linear flow characteristics Without LS shuttle valve Closed neutral position	25 $\frac{\text{l}}{\text{min}}$	-
2	Non-damped compensator valve	FC spool with linear flow characteristics With LS shuttle valve Closed neutral position	25 $\frac{\text{l}}{\text{min}}$	200 bar
3	Non-damped compensator valve	FC spool with linear flow characteristics With LS shuttle valve Open neutral position	25 $\frac{\text{l}}{\text{min}}$	200 bar
4	Non-damped compensator valve	Standard PC spool With LS shuttle valve Closed neutral position	25 $\frac{\text{l}}{\text{min}}$	200 bar

In Table 4.1 the specifications on the four flow valves are listed. From the ordering list and the data sheet in appendix D.2 the complete specification is found.

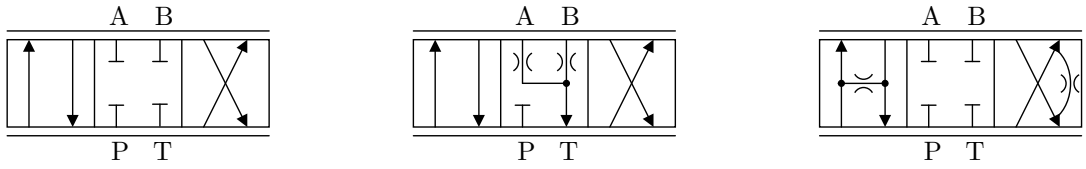

(1, 2) (3) (4)

Figure 4.3: Main spools ISO - *numbered with corresponding valve no.*

The electric valve actuation module is the type PVES. Hysteresis is approximately zero for this module. Reaction time from neutral position to max spool travel and vice versa for constant voltage supply is given in Table 4.2.

Table 4.2: PVES reaction time

Function		**Reaction time [s]**
Neutral position to max spool travel	max	0.200
	rated	0.120
	min	0.050
Max spool travel to neutral position	max	0.100
	rated	0.090
	min	0.065

4.1.2 Counterbalance Valve

Four alternatives of counterbalance valves are available, all from Sun Hydraulics. The models are listed in Table 4.3.

Table 4.3: Available counterbalance valves from Sun Hydraulics

Model	**Pilot Ratio [-]**	**Setting Range [bar]**	**Default Setting [bar]**
CWCK LHN	1:1	70-280	210
CWCL LFN	1:2	70-175	140
CWCA LHN	1:3	70-280	210
CWCG LFN	1:5	70-175	140

4.1.3 Cylinder

The test rig is actuated by a double acting asymmetric cylinder of type 25 CA from PMC Cylinders. It has a stroke of 500 mm, a piston area of 65 mm^2, and a rod area of 35 mm^2.

4.1.4 Hoses

Hydraulic hoses used on the test rig are made by Manuli Hydraulics. Specifications are listed in Table 4.4.

Table 4.4: Hydraulic hose dimensions

Hose number	Type	Pressure ratings [bar]	Diameter [in]	Length [mm]
H1	ROCKMASTER/2SN	350	1/2	800
H2	ROCKMASTER/2SN	350	1/2	1150
H3	ROCKMASTER/2SN	350	1/2	750

4.2 Instrumentation

The actuation of the cylinder is performed by either manual or electronic control of a hydraulic directional control valve. Since the goal is to create a control system which compensated for the instability in the system by actuating the valve, the test rig has been equipped with multiple sensors. The data acquisition from the sensors and the electronic actuation is performed by the use of a National Instruments CompactRIO equipped with input and output modules. In appendix D.3 is the electric diagram of the test rig found. Figure 4.4 shows the test rig's electro cabinet.

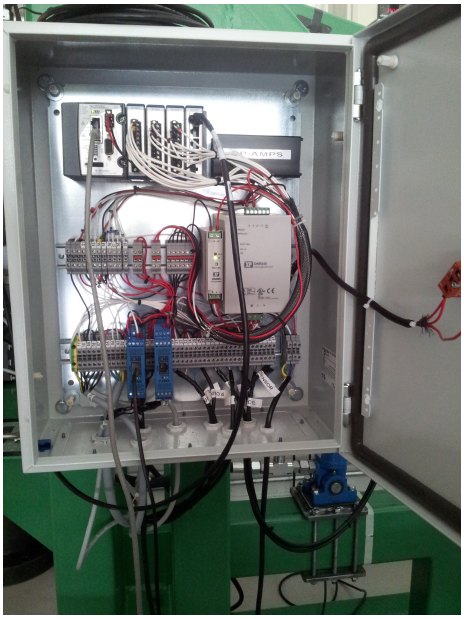

Figure 4.4: The test rig's electro cabinet

4.2.1 Sensors

The test rig is equipped with multiple pressure sensors, a flow sensor and a cylinder position sensor. In gauge sensors are also attached to the boom. The directional control valves used in the project is equipped with internal control systems for maintaining desired spool positions. The feedback signals from the spools are available for monitoring. In appendix D.1 are URLs to the sensors used found.

Pressure Sensors

The pressure sensors are of type Parker SCP-400. The sensors gives a voltage output of 0-10 V in the pressure range 0-400 bar. The outputs of the sensors were adjusted at atmospheric pressure without flow.

Flow Sensor

The flow rate meter is of type Parker SCQ-150. It gives an output current of 0-20 mA in the flow range -150 $\frac{\text{l}}{\text{min}}$ to 150 $\frac{\text{l}}{\text{min}}$ where 10 mA equals zero flow. The sensor cable is connected to a grounded resistor of 500 Ω. The resulting voltage drop over the resistor (0-10 V) is used as input to the analog input module. The sensor output was adjusted at zero flow.

Cylinder Position Sensor

The cylinder position sensor is a potentiometer of type Regal PS6310 . The output of the sensor from fully retracted to fully extracted cylinder is 0-100 % of supply voltage (6 V). The adjustment of the sensor and the conversion from voltage to millimeters follows equation (4.1).

$$\text{cylinder length} = \frac{\text{measured voltage} - \text{voltage at fully retracted}}{\text{voltage at fully extracted}} \cdot \text{cylinder length (500 mm)} \tag{4.1}$$

Valve Feedback

The spool position feedback signal used in the valve's internal control system is available for monitoring. The output voltage in 0.5 to 4.5 V in the range [-1...1].

Strain Gauge

The test rig has been equipped with two foil strain gauges connected in a half bridge configuration. The sensors are of type FLA-10-11 with a gauge actor equal to 2.11.

4.2.2 Set-up

The sensors and valves are connected to input/output (I/O) modules on a real time controller of type Compact RIO (cRIO) made by National Instruments. In addition to a real-time controller, the cRIO is equipped with a field-programmable gate array (FPGA) module. This module is able to process inputs and outputs with a high speed, and is the link between the I/O modules and the real-time controller. The model type of cRIO and I/O modules used are listed in Table 4.5.

In Figure 4.5 is a flowchart of the set-up shown. The sensors and valves are connected to the I/O modules. Signal noise is removed by lowpass filtering the signals on the FPGA module. Further signal processing and control systems and are run on the real-time controller. The real-time controller also sends data to a computer for monitoring and logging purposes. The FPGA's cycle time is 50 μs. The real-time controller is running multiple loops with different cycle times. The cycle times varies from 5 ms and up.
A list summarizing the functionality programmed on the FPGA, Real-Time controller and PC follows.

- FPGA - 1 single time critical loop with a cycle time equal to 50 μs:
  - I/O module communication (sending and receiving signals)
  - Low pass filtering of received signals
- Real-Time controller - both time critical and non-critical loops with cycle times ranging from 5 ms and up:
  - Conversion of signals
  - Differentiation of signals
  - Signal processing
  - Running of control systems
- PC - multiple non-critical loops with cycle times ranging from 10 ms and up:
  - Monitoring of signals (plots)
  - Logging (saving data to files)

4.2.3 Software

The programs running on the FPGA, Real-Time controller and PC are all programmed in LabVIEW which is a software developed by National Instrument. LabVIEW uses a graphical dataflow programming language which takes place in two planes. Programs are built up by blocks in a block diagram view which has a big variety of built-in blocks for data operations (e.g. timers, filters, PID-controllers etc.). The front panel view is the user interface while the program in running. Here the user can change parameters of blocks, start/stop loops, monitor values etc. In Figure 4.6 is a part of the block diagram running on the Real-Time controller shown. Figure 4.7 shows a part of its front panel.

Table 4.5: Real-Time Controller and Modules

Model	Description	No.
NI 9022	cRIO Real-Time Controller	1
NI 9201	8 channel Analog Input Module	2
NI 9263	4 channel Analog Output Module	1
NI 9237	4 channel Analog Input Bridge Module	1

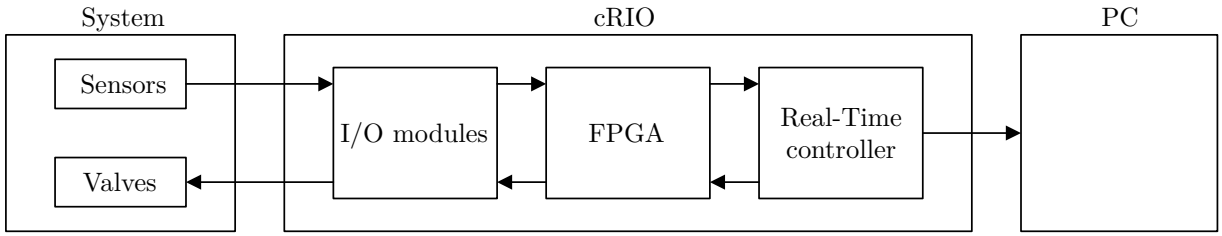

Figure 4.5: Instrumentation set-up

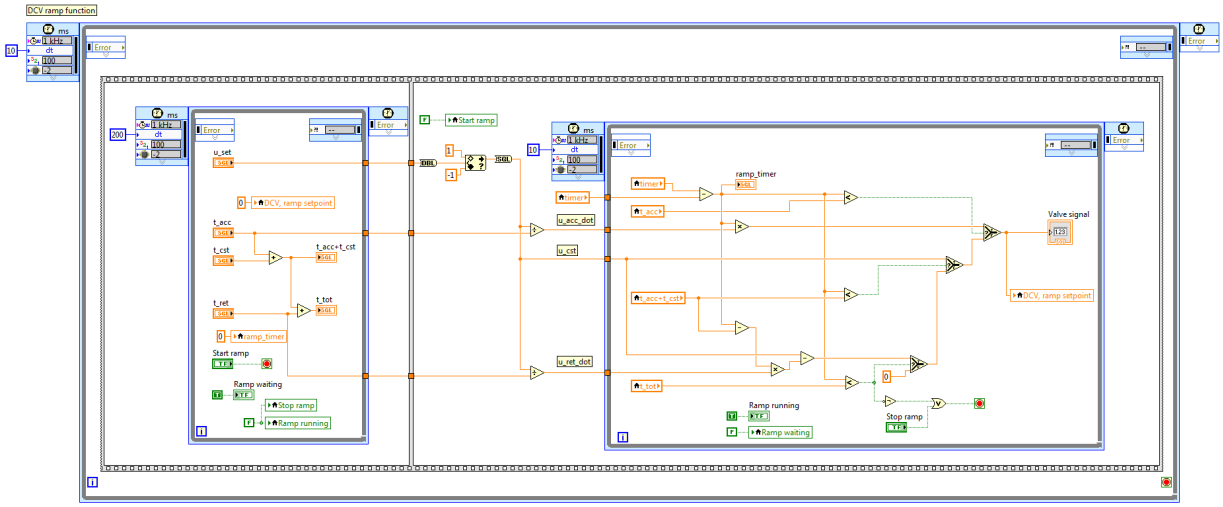

Figure 4.6: Example of a loop running on the cRIO's Real-Time controller

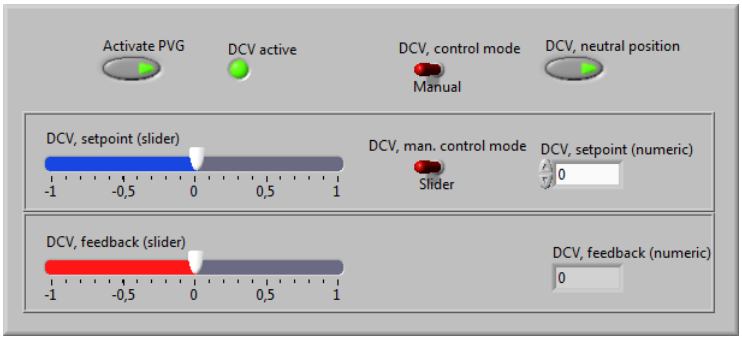

Figure 4.7: Example of a front panel running on the cRIO's Real-Time controller

Chapter 5

Verification of Simulation Model

5.1 Parameter Identification

5.1.1 Volumes and Capacitance

The majority of the volume in the hydraulic circuit, excluding the cylinder cambers, are hoses and therefore the volumes in pipes are neglected. Volume in line 2 in the hydraulic schematic in Figure 2.8 consists of hose H1 from Table 4.4. The approximate size of the volume is $V_{L2} = 100$ cm^3. Volume in line 3 consists of hose H2, giving an approximate volume $V_{L3} = 150$ cm^3. Volume in line 4 consists of both hose H1 (two equal pieces, not the same hose as in volume 2) and H3, giving an approximate volume $V_{L4} = 200$ cm^3.

Dead volumes in the cylinder chambers are not given in the data sheet. These are assumed to be $V_{CH1} = V_{CH2} = 50$ cm^3. The volume between the PCV and the main spool is assumed to be $V_1 = 2$ cm^3.

The capacitance of the lines are estimated by performing experiments on line 4. The cylinder is set to a short cylinder length in order to have small cylinder volume added to the line. A mass is then added to the boom while the cylinder length, l_{cyl}, and the pressure in the piston side cylinder chamber, p_3, are logged. The resulting plots are shown in Figure 5.1. The steady state values of the cylinder length and pressure before the mass is added are calculated by taking the means between 0 s and 6 s. After the load is added the means between 14 s and 19 s are calculated. The steady state values are shown in Table 5.1. The capacitance of the fluid itself is neglected.

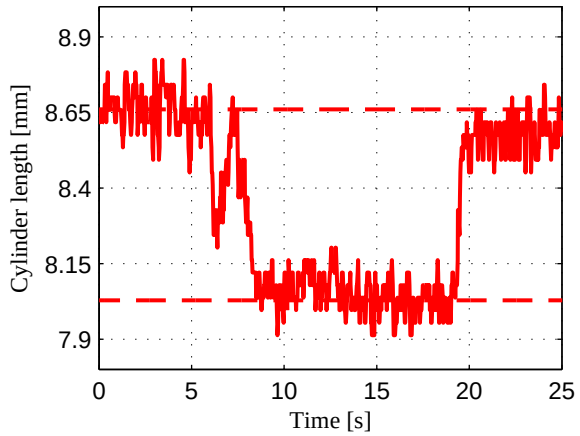

(a) Cylinder length in solid line and mean steady state values in dashed lines

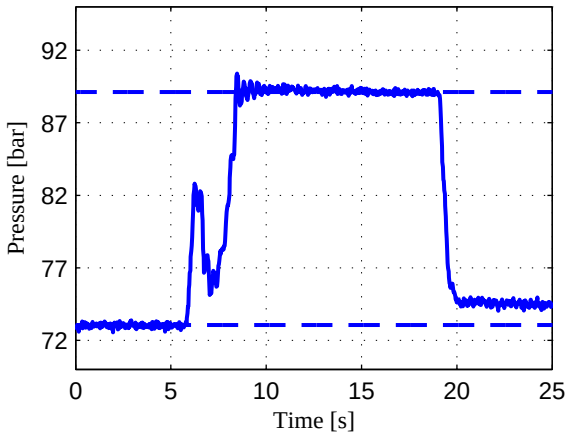

(b) Pressure in piston side cylinder chamber and mean steady state values

Figure 5.1: Plots used for estimation of capacitance

The capacitance is calculated by dividing the relative relative volume change by the relative pressure change

Table 5.1: Cylinder friction model parameters

Parameter	**Before added mass**	**After added mass**
l_{cyl}	8.66 mm	8.03 mm
p_3	73.1 bar	89.1 bar

according to equation (5.1). The calculation yielded a capacitance equal to 0.13 $\frac{\text{cm}^3}{\text{bar}}$.

$$C_{w,L4} = \frac{\Delta V_{L4}}{\Delta p_3} = \frac{\Delta l_{cyl} \cdot A_c}{\Delta p_3} \tag{5.1}$$

A general expression for the capacitance is found by dividing expression for the capacitance of line 4 with its volume, and multiplying by the volume of interest. This makes line volume an input to the equation, and capacitance of the line output, see equation (5.2). Table 5.2 shows the volumes and capacitances of the lines in the system.

$$C_w = \frac{0.13 \frac{\text{cm}^3}{\text{bar}}}{200 \text{ cm}^3} \cdot V = 0.00065 \frac{1}{\text{bar}} \cdot V \tag{5.2}$$

Table 5.2: Volumes and estimated capacitances of lines

Line	**Volume [cm^3]**	**Capacitance [$\frac{\text{cm}^3}{\text{bar}}$]**
V_{L2}	100	0.0650
V_{L3}	150	0.0975
V_{L4}	200	0.1300

5.1.2 Cylinder Friction

In order to determine the friction in the cylinder, experimental tests were performed. The pressures in both cylinder chambers, cylinder position and cylinder velocity were logged while running the cylinder from bottom to top and top to bottom at different, constant, valve openings. Since valve number 2 in Table 4.1 was used, a constant valve opening yielded a constant cylinder velocity due to the pressure compensation.

Due to somewhat noisy signals, the cylinder lengths, l_{cyl}, equal to 100 mm, 150 mm, 200 mm, 250 mm and 300 mm running the cylinder from top to bottom were investigated. The reason for investigation of multiple cylinder lengths is the pressure dependency of the friction discussed in subsection 2.2.3. The force from the pressures were calculated, and subtracted from simulated cylinder force in the same cylinder positions according to equation (5.3). The results is shown in Figure 5.2. The static friction equal to -1300 N is not measured, but assumed from the slope of the low-velocity curvatures.

$$F_{frik} = F_{sim} - (p_3 \cdot A - p_4 \cdot \mu_c \cdot A) \tag{5.3}$$

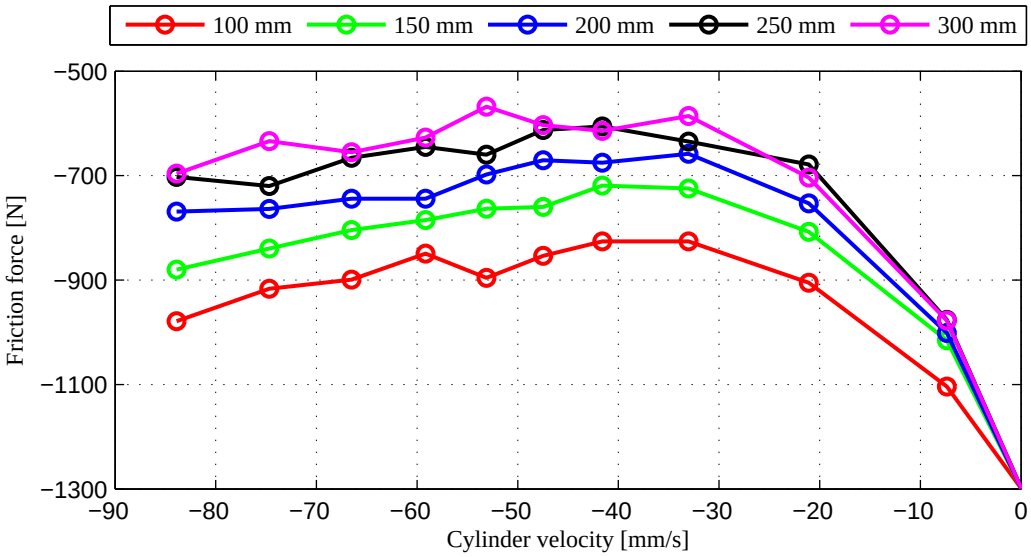

Figure 5.2: Measured friction force - *force calculated from measured cylinder pressures subtracted from simulated cylinder load force*

The friction model proposed by Ottestad et al. shown in equation (2.63) in subsection 2.2.3 was modified to equation (5.4), making the model dependent of the cylinder stroke, x_c, instead of the pressures. The modification was needed because neither the pressure dependency in the model proposed by Ottestad et al. nor Bak's model in equation (2.65) were able to reproduce the friction observed. The modification makes the friction model more accurate in this specific situation, but can not be used generally. The hyperbolic tangent term, $\tanh(C_{tan} \cdot v_c)$ is added so the friction model works for both positive and negative velocities, in addition to avoiding singularity at zero velocity.

$$F_{fr} = \tanh(C_{tan} \cdot v_c) \cdot \left(F_c + (F_s - F_c) \cdot e^{-\frac{|v_c|}{v_0}} + C_v \cdot |v_c| + \frac{x_c}{C_l} \right) \tag{5.4}$$

The solver add-in in Microsoft Excel is used for parameter identification. Each point of measurement is given as input to the model. The squared difference between the actual measure and the model output is then calculated for each point. All squared differences are then summed. The sum is then minimized by the solver by changing the parameters in equation (5.4).

The parameters found are shown in Table 5.3. In Figure 5.3 is the measured friction plotted with the friction model in the measured area. The friction model with l_{cyl} equal to 0 mm, 250 mm and 500 mm is shown in Figure 5.4.

Table 5.3: Cylinder friction model parameters

Parameter	Description	Value	Unit
C_l	Cylinder stroke coefficient	34629	$\frac{\text{mm}}{\text{N}}$
C_{tan}	Hyperbolic tangent coefficient	10.31	$\frac{\text{s}}{\text{mm}}$
C_v	Viscous velocity coefficient	4.06	$\frac{\text{Ns}}{\text{mm}}$
F_c	Coulomb friction	273.99	N
F_s	Static friction	1155.43	N
v_0	Stribeck velocity	14.19	$\frac{\text{mm}}{\text{s}}$

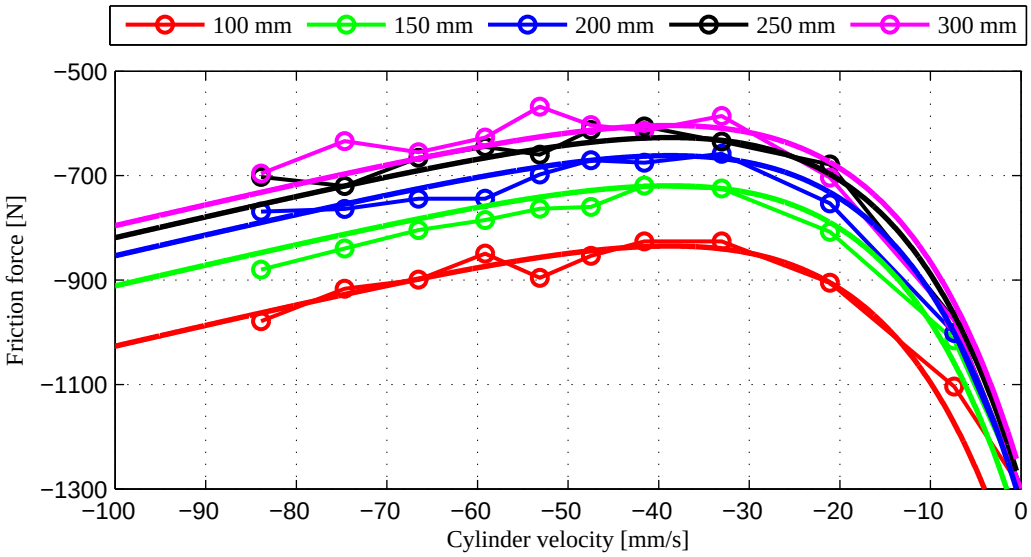

Figure 5.3: Measured friction and friction model - *Measured friction represented by solid lines with circles, friction model represented by solid lines only*

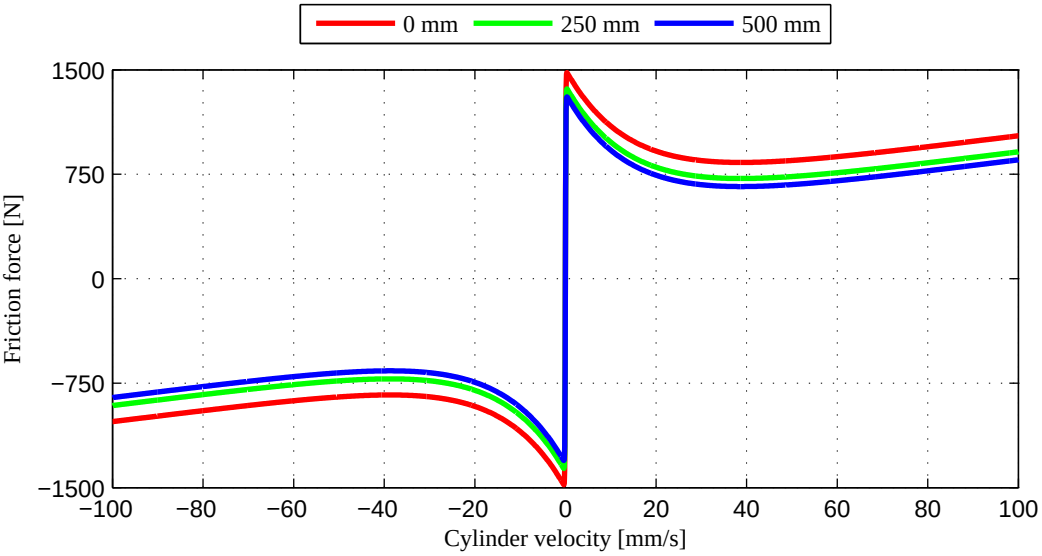

Figure 5.4: Cylinder friction model

5.1.3 System Eigenfrequency

The eigenfrequency of the system was estimated by experiments. The main boom was set in horizontal position and carefully excited by hand trying not to interfere the system's eigenfrequency. The pressure in the piston side cylinder chamber was logged with respect to time. The resulting plot is shown in Figure 5.5.

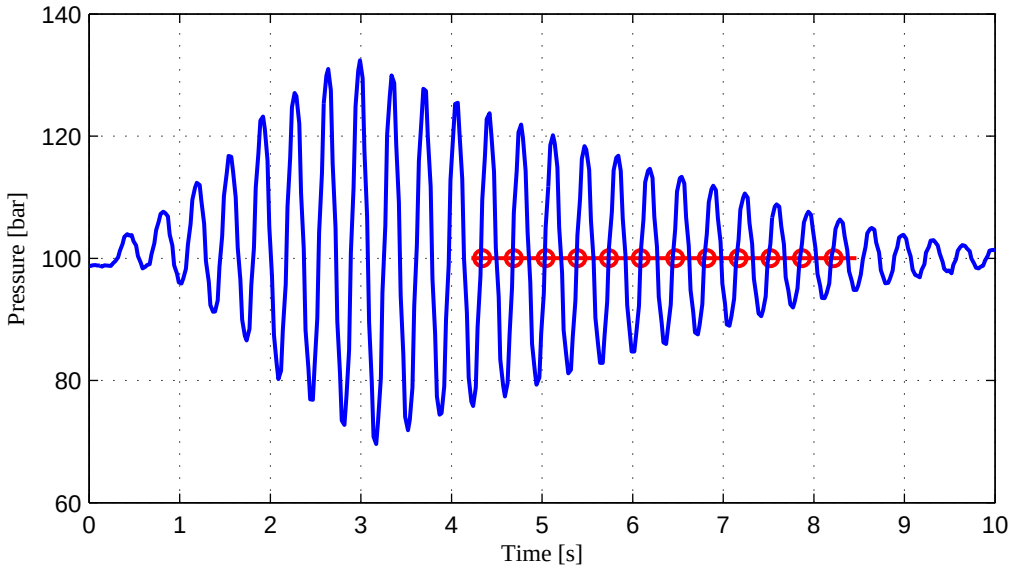

Figure 5.5: eigen

The manual excitation was started approximately at $t = 0.5$ s, and stopped at approximately $t = 3$ s. In order to let the system cancel out an eventual interference, a few periods were waited until the estimation was started. The eigenfrequency was estimated by equation (5.5), yielding an eigenfrequency, f_n, equal to 2.85 Hz.

$$f_n = \frac{N}{t_{N=N} - t_{N=1}} \tag{5.5}$$

where

f_n : Eigenfrequency in Hz
N : Number of periods

5.2 Simulation Results

Changes to the capacities and the cylinder friction in the simulation model was done and simulated. The friction model in equation (5.4) took too much of the computational load. The friction model itself fits the system better than the friction model used in chapter 3, but due to being too time consuming it is not used in the further simulations. The previous friction model is still used.

The plot in Figure 5.6 shows the feedback spool position signal from the main spool. The fluctuations in the test rig spool signal in the beginning and end of the ramping cycle is due to anti-bandwidth used in the logging software, and is not physically fluctuating. In Figure 5.7 a close up view of the spool positions is shown between 0 s to 1.2 s.

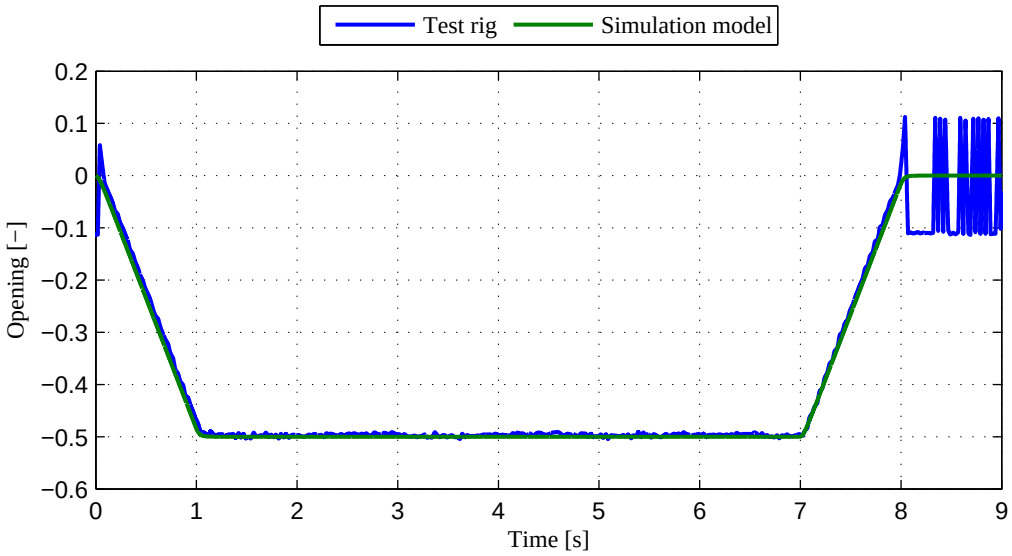

Figure 5.6: Verification of simulation model main spool opening plot

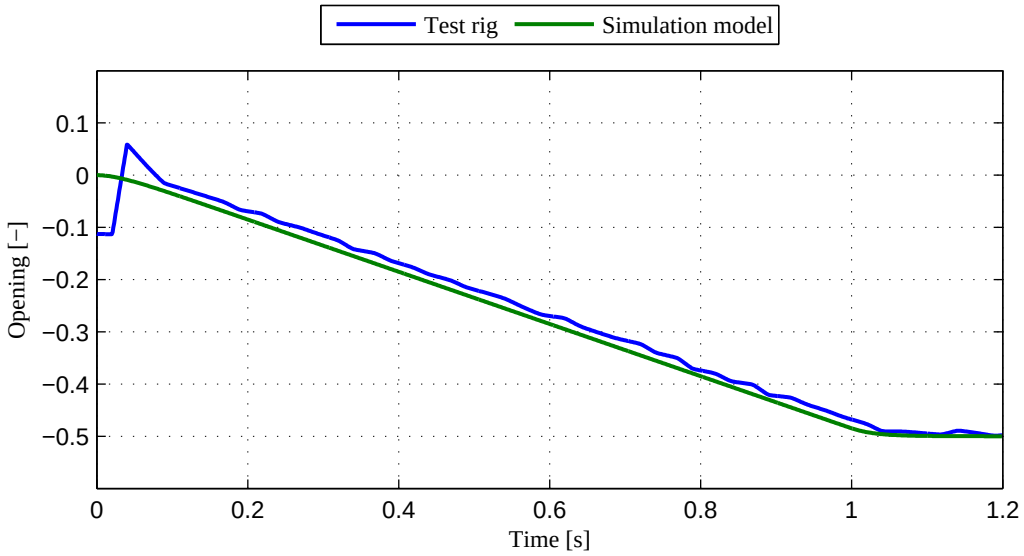

Figure 5.7: Verification of simulation model main spool opening plot

In Figure 5.8 the cylinder position, x_c, is shown. The deviation in position between the models at the end of the ramping cycle is 20 mm.

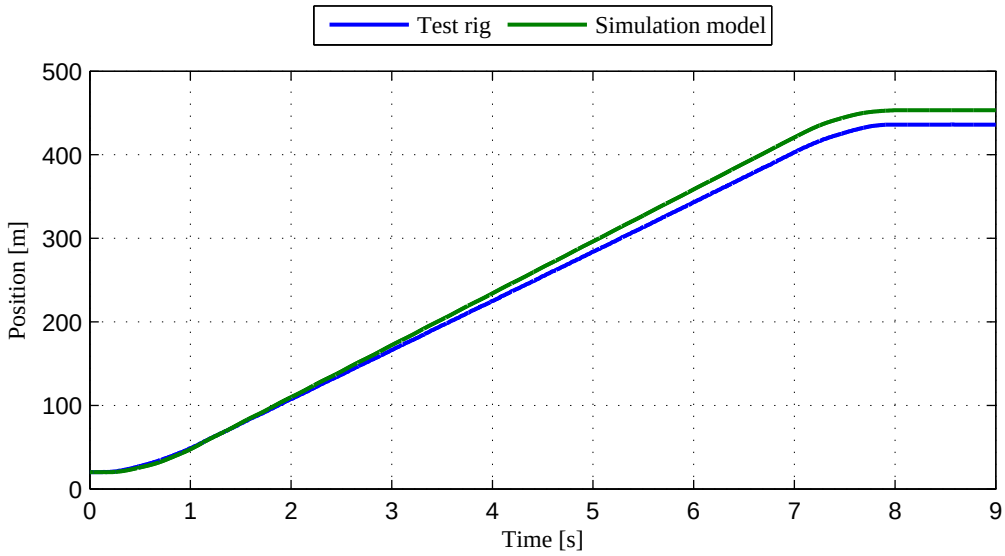

Figure 5.8: Verification of simulation model position plot

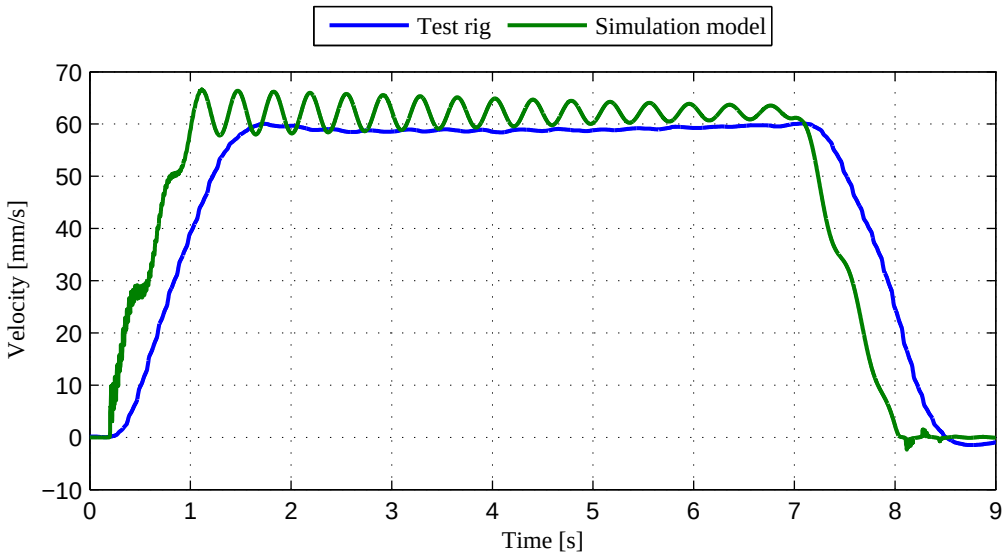

Figure 5.9: Verification of simulation model velocity plot

The velocity plot in Figure 5.9 shows that the cylinder velocity in the simulation model has a faster response and is more oscillatory than the physical test rig. The simulation model seems to be stiffer than the physical test rig.

However, the pressure in the high pressurized cylinder chamber in Figure 5.10 fits the experimental results well. As the pressure will be used as feedback, the pressure result has the highest priority.

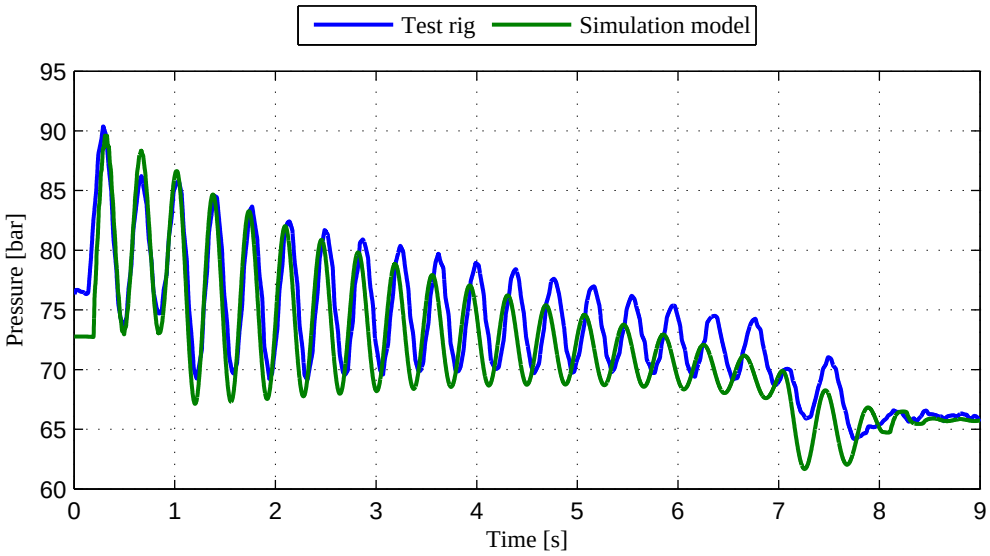

Figure 5.10: Verification of simulation model pressure plot

Chapter 6

Stabilization of the System

In this chapter the method of using pressure feedback for stabilizing the system is evaluated. The theory is to compensate for the fluctuations by giving a greater spool opening when the pressure decrease, and less spool opening when the pressure increases. In that way, the pressure fluctuations are actively damped making the system stable.

In the first section the stability is evaluated analytically. A compensation proposal using a high pass filter is reviewed and new parameters are proposed. Furthermore, the method is tested on the simulation model in the second section.

Requirements to the system response is not set, but if possible the compensation parameters are tuned to yield a better response. Proving that the stabilizing method works without compromising the velocity is the object.

6.1 Pressure Feedback

In section 2.3 the pressure compensated system combined with a counterbalance valve was proved unstable for most of the cylinder stroking. To improve the stability margins of the system the pilot pressure, p_4, is used as feedback as shown in Figure 6.1.

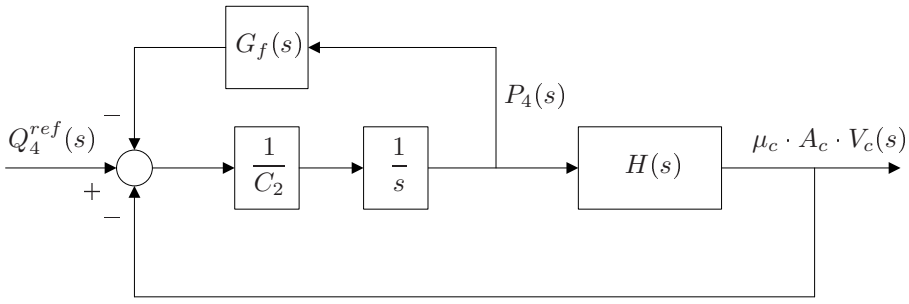

Figure 6.1: Closed loop block diagram using pressure feedback

The transfer function block $H(s)$ is given in equation (2.81) in section 2.3 and written again in equation (6.1).

$$H(s) = \kappa \cdot \frac{\tau \cdot s + 1}{\frac{1}{\omega_n^2} \cdot s^2 + \frac{2 \cdot \zeta}{\omega_n} \cdot s + 1} \tag{6.1}$$

In [1] a high pass filtered pressure is proposed used as feedback. The filter increases phase margin around the filter frequency, ω_f, and adjust the gain margin by the filter gain, K_f. The filter yields the following

transfer function.

$$G_f(s) = K_f \cdot \frac{s}{\frac{1}{\omega_f} \cdot s + 1} \tag{6.2}$$

It is shown in [1] that the filter gain K_f adds extra capacitance to C_2 in the rod side volume V_4. The filter gain is chosen from the stability criterion in equation (2.86) in section 2.3 so that the capacitance in V_4 always fulfills the criterion.

$$K_f = C_1 \cdot \mu_c \cdot \mu_p \tag{6.3}$$

The filtered pressure feedback is proven stable in [1] for the system shown in Figure 6.1 with filter gain in equation (6.3) and a filter frequency $\omega_f = 0.5 \cdot \omega_n$. However, the stability highly depends on the valve dynamics as the bandwidth of the valve may be less than the system bandwidth, so a valve block is added to the block diagram.

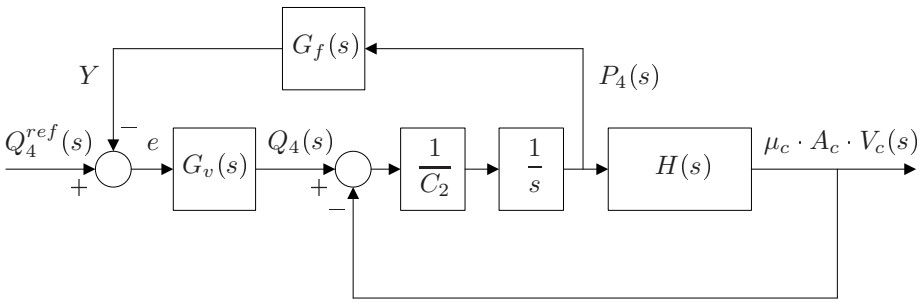

Figure 6.2: Closed loop block diagram with valve dynamics and pressure feedback

In equation (2.45) in subsection 2.2.1 the valve is approximated to yield a first order transfer function. The transfer function is shown below.

$$G_v(s) = \frac{1}{\frac{1}{\omega_v} \cdot s + 1} \tag{6.4}$$

where

$$\frac{1}{\omega_v} = \frac{T_s}{4}$$

The time constant, $\frac{1}{\omega_v}$, for a first order system is given by one fourth of the settling time. Rated reaction time from neutral to max spool travel (see Table 4.2) is used as settling time for the valve. For a conservative design, the maximum reaction time would have been used, but as the spool travel is assumed not to use a full spool travel for compensating for the pressure fluctuations the rated reaction time is used.

The stability of the system including the valve dynamics is investigated from the open loop transfer function. Input to the open loop transfer function is the error, e, and output is the feedback, Y, and yields the following transfer function.

$$G_{ol}(s) = \frac{Y}{e} = s \cdot \frac{G_v(s) \cdot G_f(s)}{C_2 \cdot s + H(s)} \tag{6.5}$$

The open loop transfer function of the system has a derivative term, in contrary with [1] where the open loop transfer function has an integral term. It seems that transfer block for the valve in [1] receives a feedback from the internal system feedback flow $\mu_c \cdot A_c \cdot V_c(s)$. This is not the case for neither the valve nor the compensation method used in this project. The open loop transfer function in equation (6.5) is therefore used, yielding different bode plot characteristics than in [1].

In Figure 6.3 a bode plot of the open loop transfer function is shown. Now the system is seen to be unstable using the filter parameters proposed for the system with infinite valve bandwidth in [1]. The feedback signal does not exceed 0 dB, meaning that the feedback, Y, is less than the error, e, and the stabilizing effect of the feedback is gone. The valve dynamics is clearly influencing the stability margins.

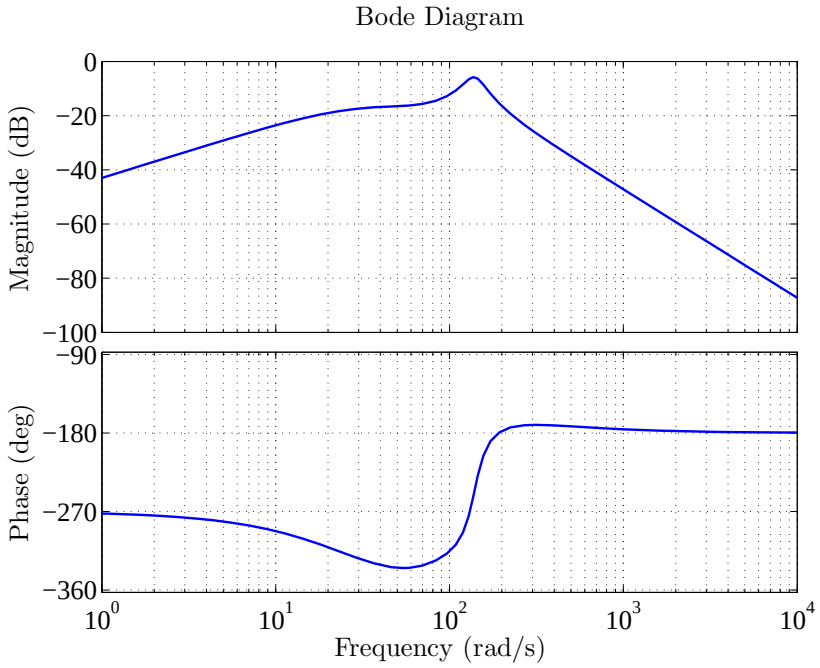

Figure 6.3: Bode plot of open loop transfer function - *filter parameters used are* $\omega_f = 0.5 \cdot \omega_n$ *and* $K_f = C_1 \cdot \mu_c \cdot \mu_p$.

Transfer function block parameters used for the bode plot is given in Table 6.1. The parameters yields the steady state solution $x_c^{(ss)} = 250$ mm and $p_4^{(ss)} = 45$ bar.

Table 6.1: Transfer function block parameters

TF block	**Parameter**	**Value**	**Unit**
$H(s)$	κ	$1.9772 \cdot 10^{-10}$	$\frac{\mathrm{m}^4 \cdot \mathrm{s}}{\mathrm{kg}}$
	τ	$1.627 \cdot 10^{-3}$	s
	ω_n	83.82	$\frac{\mathrm{rad}}{\mathrm{s}}$
	ζ	0.7796	-
$G_v(s)$	ω_v	33.3	$\frac{\mathrm{rad}}{\mathrm{s}}$
$G_{f,lp}(s)$	ω_f	41.91	$\frac{\mathrm{rad}}{\mathrm{s}}$
	K_f	$1.3593 \cdot 10^{-12}$	$\frac{\mathrm{m}^4 \cdot \mathrm{s}^2}{\mathrm{kg}}$

To achieve a stable system the influence of the open loop transfer function margins on the closed loop transient response is evaluated. The open loop transfer function has a derivative term, hence the classical design for a step response of a general second-order transfer function from desired open loop margins does not yield this transfer function. The plot in Figure 6.4 shows the gain and phase margin of the open loop transfer function of the system for varying filter gain and filter frequency values. The filter gains used to generate the plots are given in Table 6.2 as a gain factor, n_K, multiplied the previous proposed filter gain. The filter frequencies is expressed as a frequency factor, n_ω, multiplied the natural frequency of the system. The filter gain and filter frequency now yields the following equations.

$$K_f = n_K \cdot C_1 \cdot \mu_c \cdot \mu_p \tag{6.6}$$

$$\omega_f = n_\omega \cdot \omega_n \tag{6.7}$$

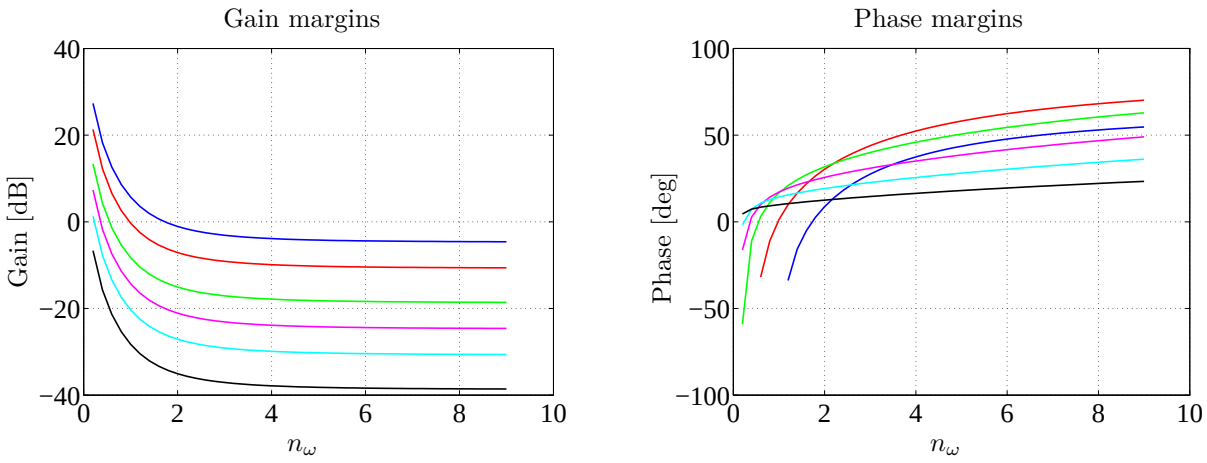

(a) Gain margins

(b) Phase margins

Figure 6.4: Open loop transfer function gain and phase margins for different filter parameter values - *Each line represents a filter gain. Filter frequencies is defined as the frequency factor n_ω multiplied the systems natural frequency.*

Table 6.2: Filter gains used in margin plots - *filter gain is given by the equation* $K_f = n_K \cdot C_1 \cdot \mu_c \cdot \mu_p$

Line no.	1	2	3	4	5	6
Color	Blue	Red	Green	Magenta	Cyan	Black
Gain factor, n_K	1	2	5	10	20	50

The phase shifting from the region around -270° to the region around -180°, as seen in Figure 6.3, is observed to yield a stable system when the gain margin is negative as seen in Figure 6.4a.

In Figure 6.5a the transient response of the closed loop transfer function given in equation (6.8) is shown, yielding gain factors 1, 5 and 50 with filter frequency factor 2. A high absolute value of the gain margin is seen to yield a slower response than a lower gain margin, but if the gain is too low the transient response becomes oscillatory and "on the edge" of instability. From the phase margins in Figure 6.4b it is seen that the phase margin for filter gain 1 (blue) at the frequency factor 2 is greater than the phase margin of filter gain 50 (black), meaning that a high filter gain is less sensitive to low phase margins than a low filter gain is when it comes to an oscillatory transient response.

$$G_{cl}(s) = \frac{\mu_c \cdot A_c \cdot V_c(s)}{Q_4^{ref}(s)} = \frac{H(s) \cdot G_v(s)}{C_2 \cdot s + H(s) + G_f(s) \cdot G_v(s) \cdot s} \tag{6.8}$$

In Figure 6.5b filter frequencies are plotted for the frequency factors 3 (blue), 5 (red) and 8 (black) with gain factor 1. For the plotted frequencies the gain margin is almost constant, while the phase margin varies from 35° to 60°. The transient response shows that the phase margin does not have any significant effect on the transient response for the plotted frequencies.

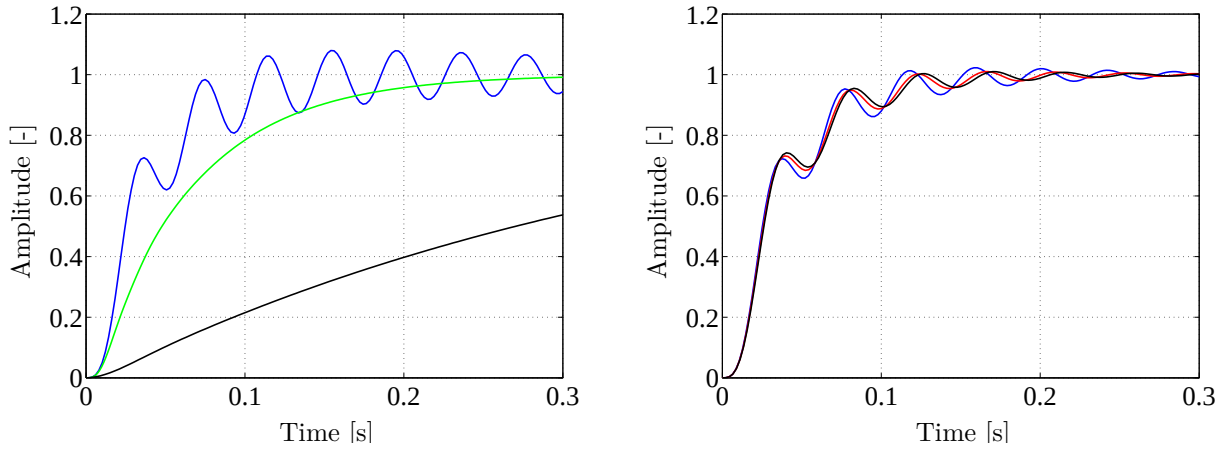

(a) Gain margins (b) Phase margins

Figure 6.5: Gain and phase margins effect on the closed loop transient response - ***Gain margins:*** *Filter gains plotted are gain factors 1, 5 and 50 with filter frequency factor 2 (1 is the oscillatory, 50 is the slowest).* ***Phase margins:*** *Filter frequencies plotted are frequency factors 3 (blue), 5 (red) and 8 (black) with gain factor 1. Note that line colors in plot (b) does not correspond the color coding in the margin plots.*

From the observations of the closed loop transient response a guideline for choosing the filter parameters is a desired gain margin in the region of -6 dB to -20 dB and phase margin around 35°, though choosing a greater phase margin does not improve the transient response noteworthy. Choosing a filter gain factor between 2 to 5 and filter frequency factor of 2 gives the desired margins seen from Figure 6.4. Gain margin, phase margin and settling time using the mentioned filter parameters are listed in Table 6.3.

Table 6.3: Filter parameters - *resulting open loop margins and closed loop time response*

Parameter	**Filter selection**				**Unit**
	a	**b**	**c**	**d**	
Gain factor, n_K	2	3	4	5	$[-]$
Frequency factor, n_ω	2	2	2	2	$[-]$
Gain margin	-7.8	-11.3	-13.8	-15.7	$[dB]$
Phase margin	31.0	33.3	32.8	31.5	[deg]
Settling time (± 2 %)	0.166	0.190	0.214	0.239	$[s]$

From Table 6.3 filter **a** results in the fastest response, however, the transient step response plot shows some oscillations. Choosing filter **b** results in a curve without visually observable oscillatory behavior and with small increase in settling time. The transient step response of the system using filter **b** is shown in Figure 6.6.

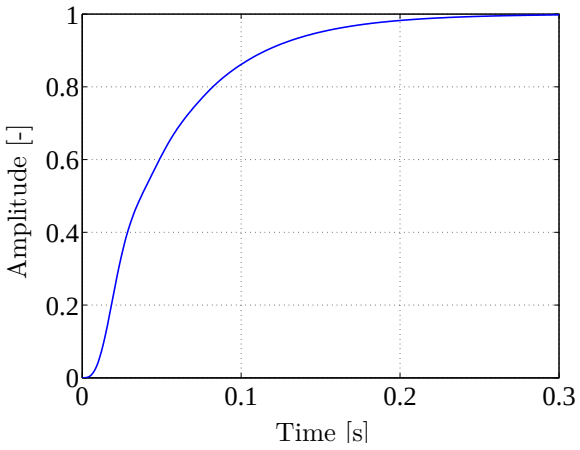

Figure 6.6: Closed loop transient step response with filter **b**

The final filter parameters are:

- $K_f = 4.08 \cdot 10^{-12}\ \frac{\mathrm{m}^4 \cdot \mathrm{s}^2}{\mathrm{kg}}$
- $w_f = 168\ \frac{\mathrm{rad}}{\mathrm{s}}$

6.2 Simulations

In this section the simulation model is used to test the filter parameters found in previous section, and if necessary tune the parameters to find better response in the simulation model.

The simulations are performed under the following conditions.

- Initial cylinder stroke set to 480 mm
- Initial pressures $p_3 = 63$ bar and $p_4 = 1$ bar
- Step input (fast ramp) of 0.1 on the spool opening reference at $t = 0$ s
- Simulation time of $T = 8$ s

Results from the simulations that are reviewed are main spool openings (reference $u^{(ref)}$, compensation contribution u_{comp} and actual u), cylinder velocity (v_c) and system pressures (pressure compensated p_1, low pressurized cylinder chamber p_4, high pressurized cylinder chamber p_4 and CBV back pressure p_2).

First, the simulation model using parameters form the stiff system found in previous section is simulated. The results are shown in Figure 6.7, Figure 6.8 and Figure 6.9. When the velocity peaks around $t = 0.3$ s, the pressure changes rapidly causing the pressure feedback compensation, u_{comp}, to corrugate the spool opening. Around $t = 1.2$ s the amplitude of the fluctuations is less than 2 % of the step input and the contribution from the pressure feedback is small. The small compensation contribution is now preventing the fluctuations picking up again, thus stabilizing the system. The same results is seen from the cylinder velocity and the system pressures.

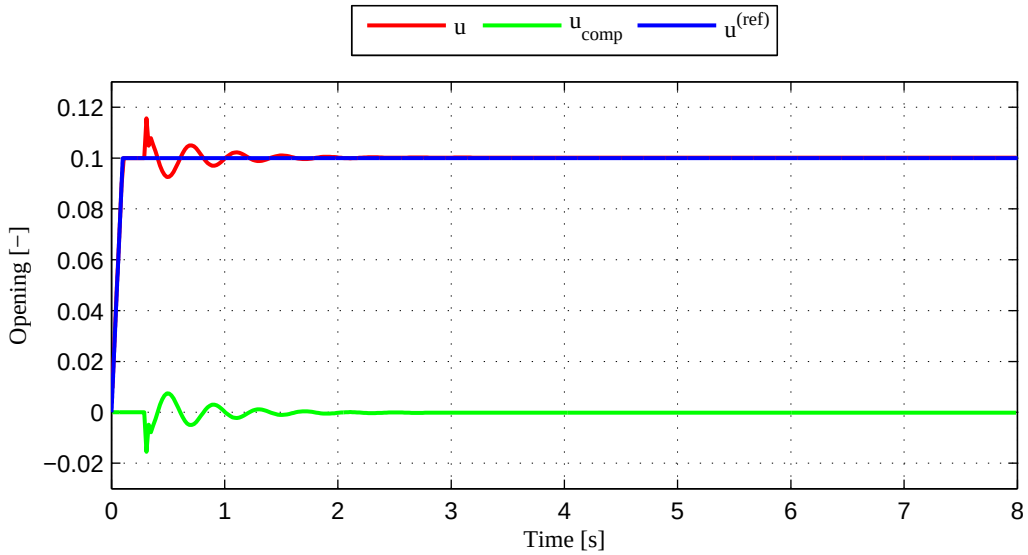

Figure 6.7: Spool openings using stiff filter parameters

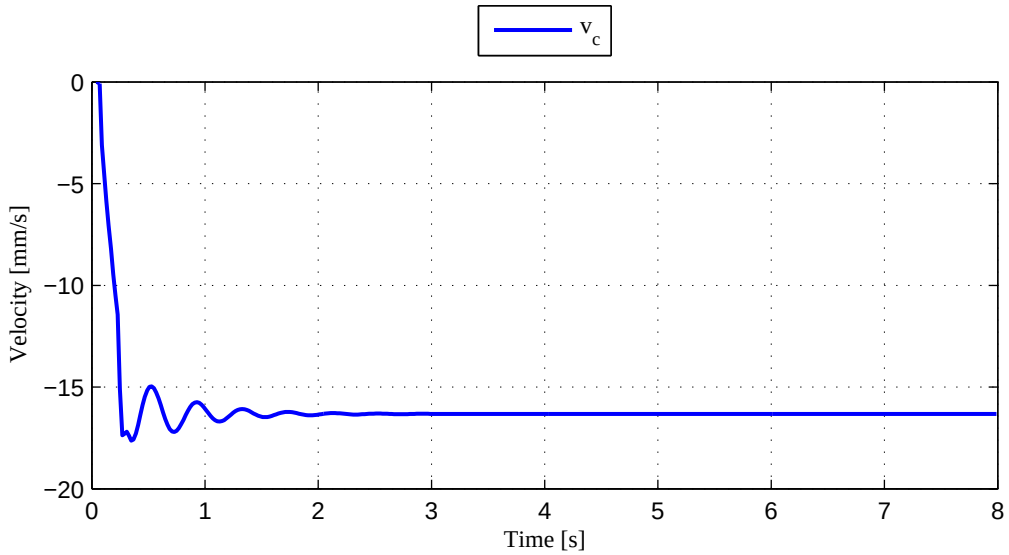

Figure 6.8: Cylinder velocity using stiff filter parameters

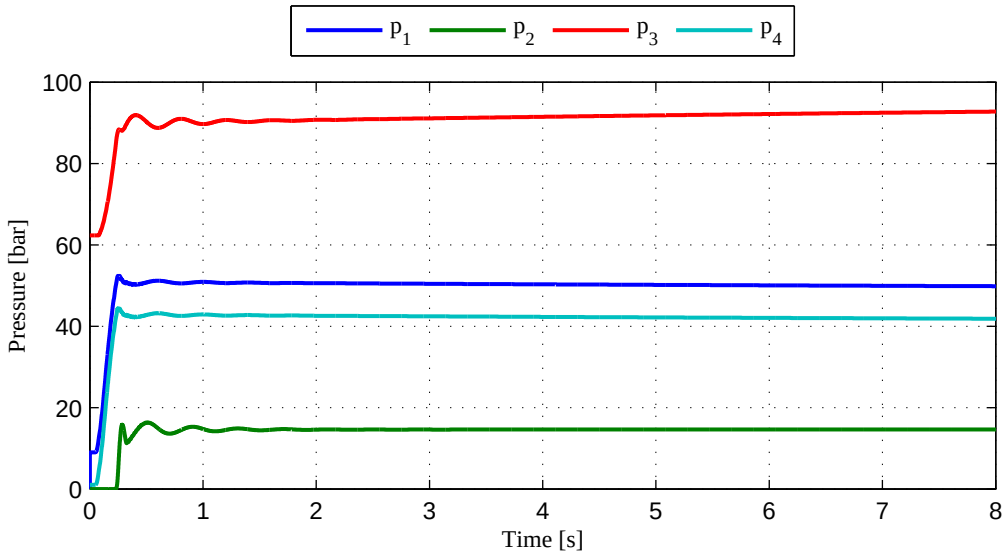

Figure 6.9: System pressures using stiff filter parameters

Though the system is stable using the stiff filter parameters the transient response could be improved. The natural frequency of the stiff system in previous section (see Table 6.1) is seen to be higher than the natural frequency of the physical test rig from the verification tests in subsection 5.1.3. Flexibility in hoses are neglected and the payload is seen as rigid. The capacitance of the hose in volume V_3 (see Table 5.2) is added to the fluid capacitance (C_1 from stiff system) to find a filter gain using a capacity closer to the simulation model. The filter frequency is changed according to the natural frequency found from the verification tests. Using the same gain and frequency factors as found for the stiff system in previous section the corrected filter parameters are:

- $K_f = 1.24 \cdot 10^{-11} \ \frac{\mathrm{m}^4 \cdot \mathrm{s}^2}{\mathrm{kg}}$
- $w_f = 35.8 \ \frac{\mathrm{rad}}{\mathrm{s}}$

Now the transient response is seen to be improved from the stiff filter parameters. The settling time of the main spool opening is about $t = 0.7$ s. The contribution from the pressure feedback is seen in Figure 6.10 to prevent the major fluctuations by increasing the main spool opening as the pressure starts decreasing and reducing the opening as the pressure rises. After that the contribution of the pressure feedback is practically speaking zero, thus the compensation does not compromise the cylinder velocity in Figure 6.11. The system pressures in Figure 6.12 also shows that the fluctuations quickly vanishes and the system is stable.

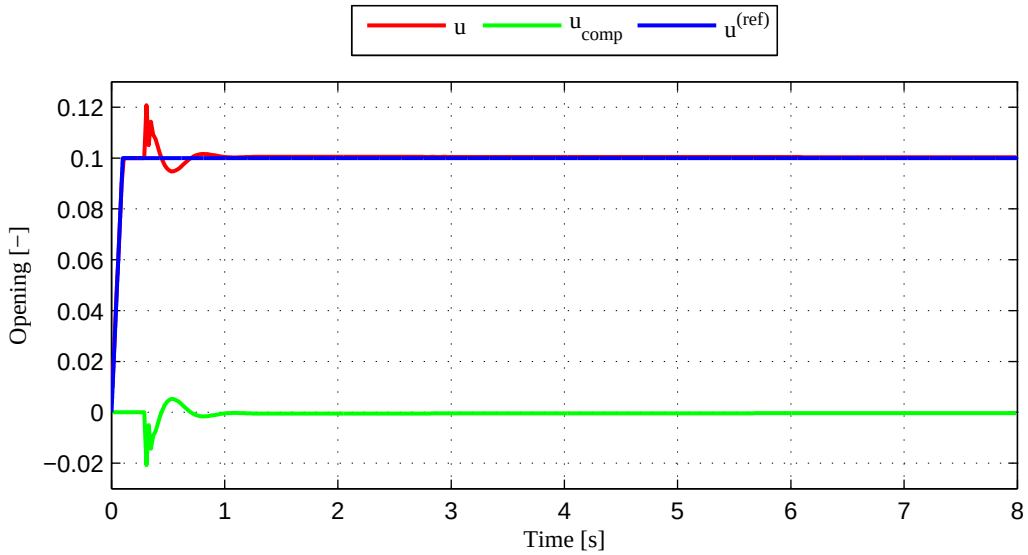

Figure 6.10: Spool openings using corrected filter parameters

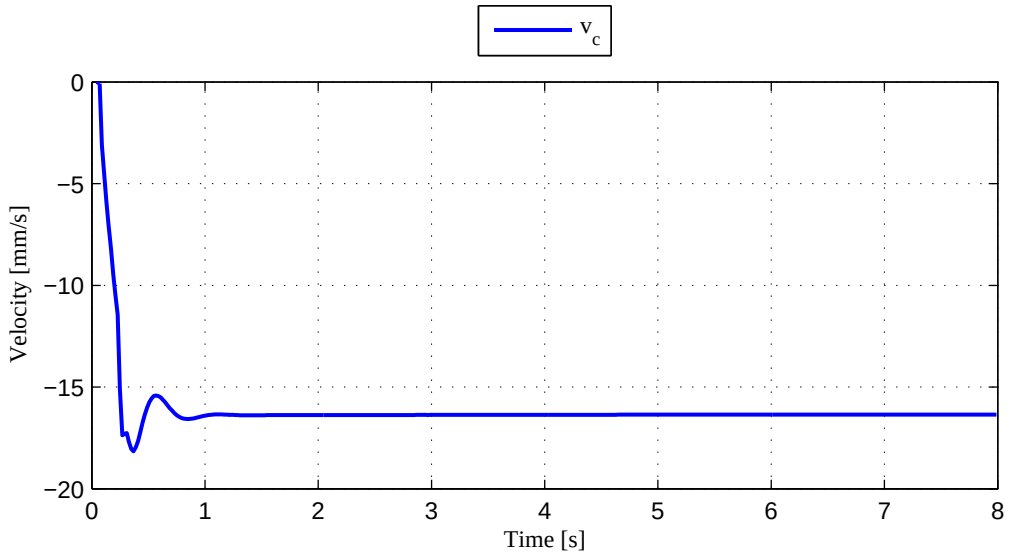

Figure 6.11: Cylinder velocity using corrected filter parameters

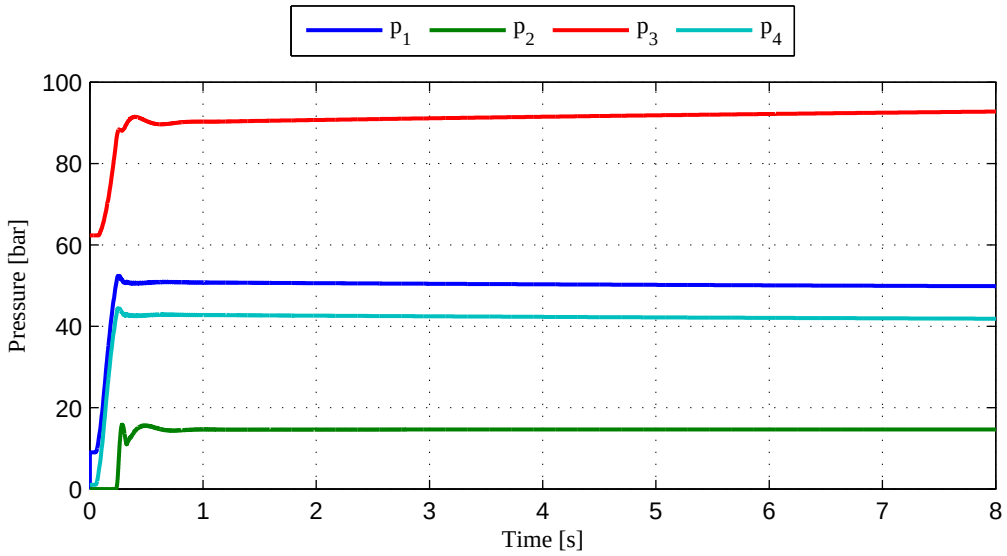

Figure 6.12: System pressures using corrected filter parameters

Chapter 7

Results

In this chapter are parameters and results from experiments performed on the physical test rig presented. Four sets sets of experiments have been performed:

- Experiment U: Uncompensated system
- Experiment A: Filter parameters derived in section 6.1 (stiff system parameters)
- Experiment B: Filter factors derived in section 6.1 combined with estimated/simulated system parameters
- Experiment C: Manually tuned filter parameters based on results from experiment B and C.

All experiments are performed under the following conditions:

- The cylinder stroke is initially set to 480 mm
- A small step input is given to the valve (5-10 %)

The piston side cylinder pressure, p_3, and the cylinder velocity, v_c, are logged during the experiments. Due to the number of individual experiments performed in experiment C only a selection of the results are shown in this chapter. All results from experiment C are found in appendix C.1. Unfortunately the cylinder velocity signals were noisy, and had to be filtered numerically from the log files. This had to be done in order to obtain any reason from the velocity plots, but because of this filtration, the results may be arguable. The numerical filtering was performed by a moving average filter.

7.1 Experiment U: Uncompensated System

The valve of the uncompensated system is given a step input equal to 0.10. The resulting piston side cylinder pressure and cylinder velocity are shown in Figure 7.1.

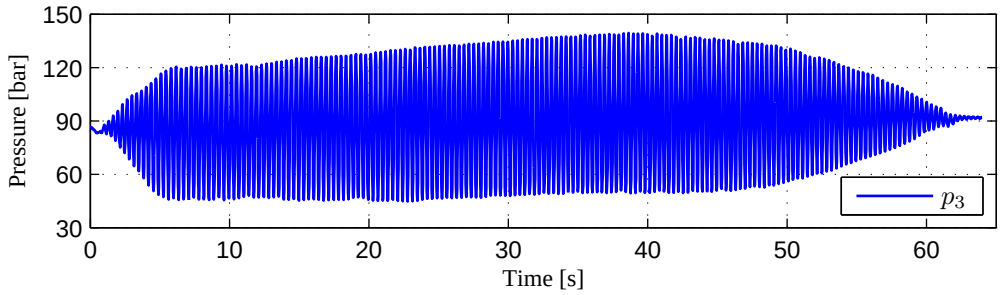

(a) Piston side cylinder chamber pressure

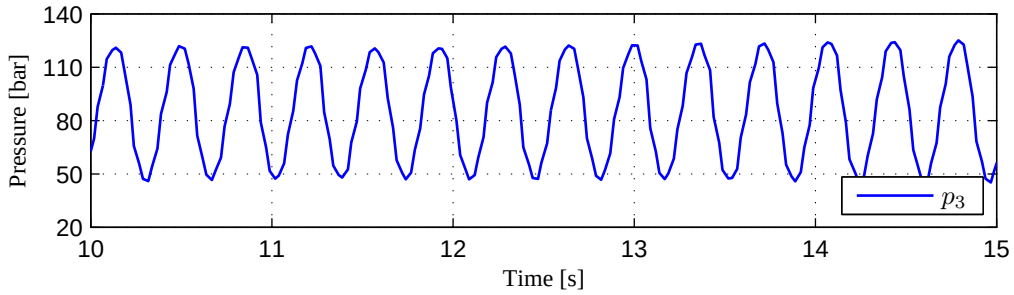

(b) Piston side cylinder chamber pressure from 10 s to 15 s

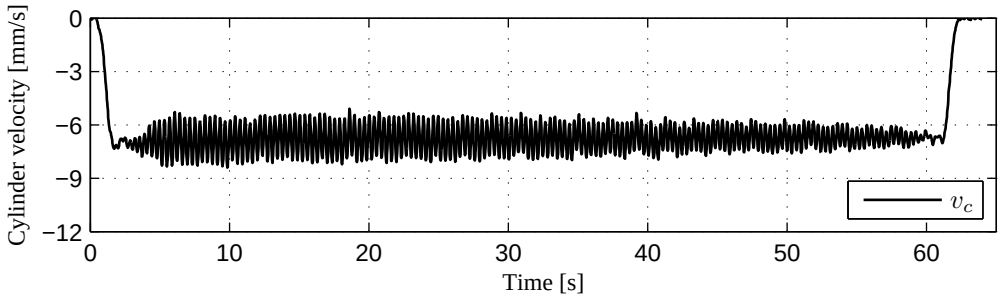

(c) Cylinder velocity

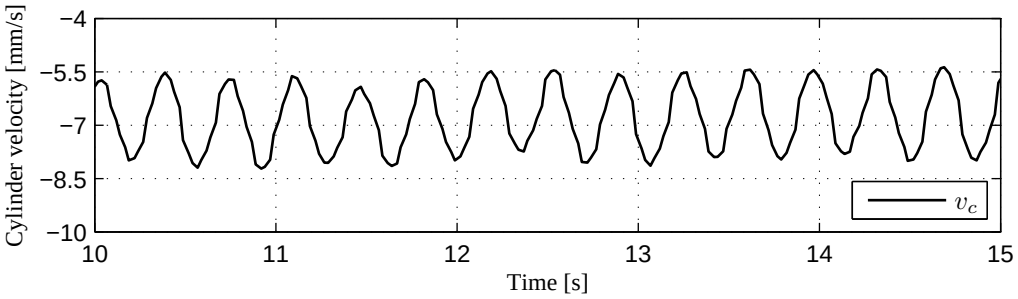

(d) Cylinder velocity from 10 s to 15 s

Figure 7.1: Piston side cylinder chamber pressure and cylinder velocity during uncompensated experiment

7.2 Experiment A: Rigid System Parameters

In this experiment the parameters for the stiff system found in section 6.1 are tested. The derivations in the section yields the use of a gain factor, n_K equal to 3 and a frequency factor, n_ω equal to 2, equation (6.6) and (6.7). For the stiff system an eigenfrequency of 84 $\frac{\text{rad}}{\text{s}}$ (13.4 Hz) is found. The filter parameters used in the experiment are found in Table 7.1.

Table 7.1: Parameters of experiment A

Experiment	**Valve input**	**Filter frequency**		**Filter gain**
	u, $[-]$	ω_f, $\left[\frac{\text{rad}}{\text{s}}\right]$	f_f, [Hz]	K_f, $\left[\frac{\text{m}^4\text{s}^2}{\text{kg}}\right]$
A	0.10, step	168	26.7	4.08e-12

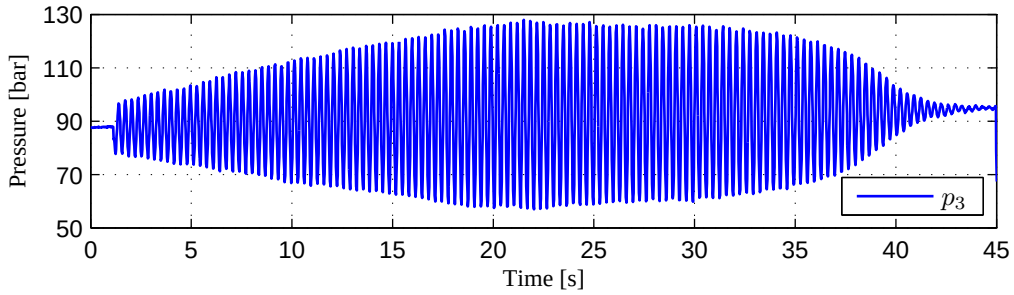

(a) Piston side cylinder chamber pressure

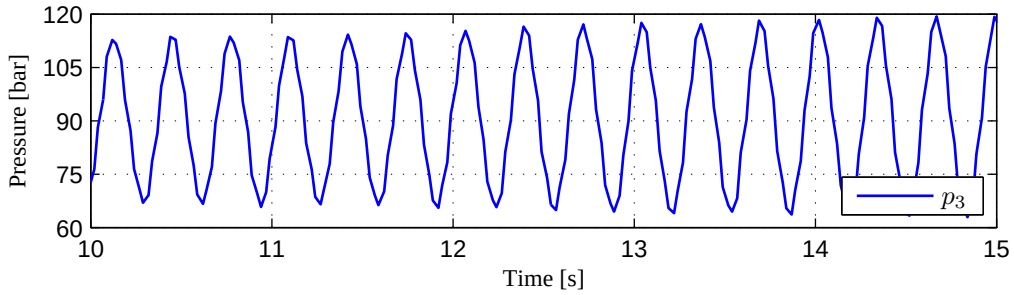

(b) Piston side cylinder chamber pressure from 10 s to 15 s

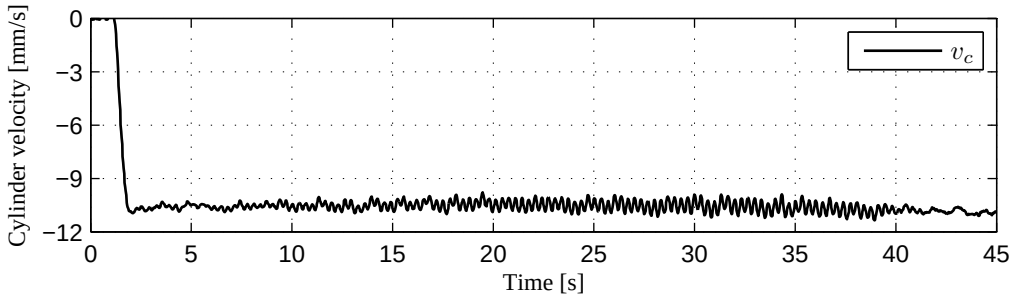

(c) Cylinder velocity

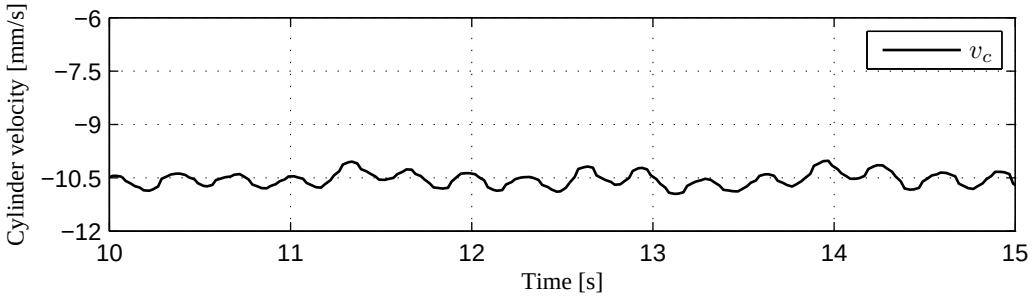

(d) Cylinder velocity from 10 s to 15 s

Figure 7.2: Piston side cylinder chamber pressure and cylinder velocity during experiment A

7.3 Experiment B: Simulated System Parameters

In this experiment the filter parameters yielding the best results from the simulations in section 6.2 is tested. The filter paramters are shown in Table 7.2.

7.3.1 Experiment B

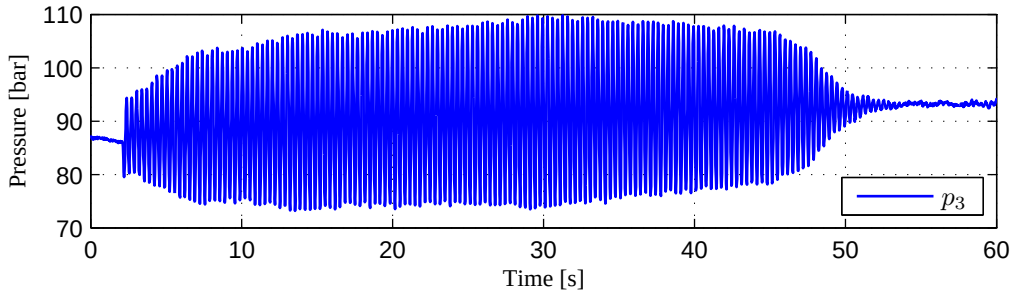

(a) Piston side cylinder chamber pressure

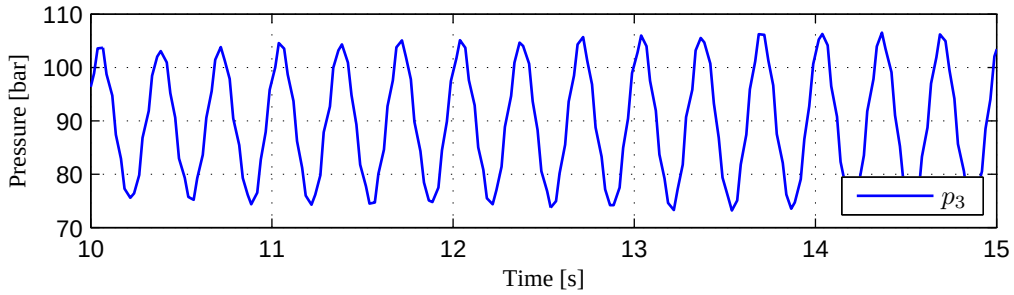

(b) Piston side cylinder chamber pressure from 10 s to 15 s

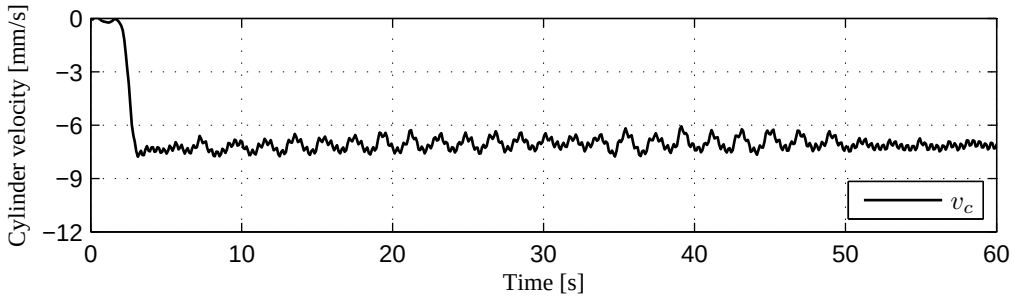

(c) Cylinder velocity

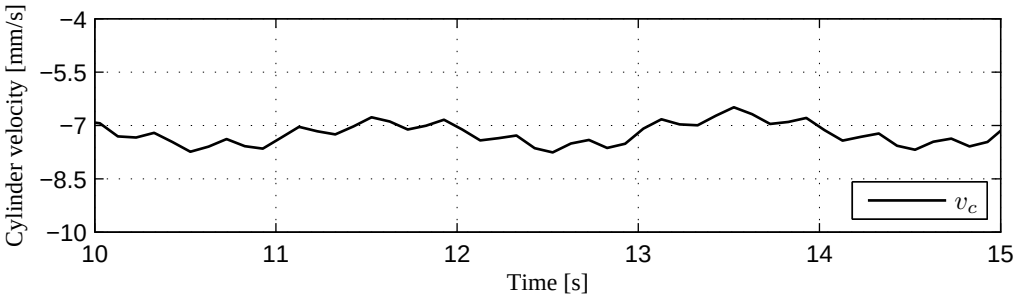

(d) Cylinder velocity from 10 s to 15 s

Figure 7.3: Piston side cylinder chamber pressure and cylinder velocity during experiment B

Table 7.2: Parameters of experiment B

Experiment	**Valve input**	**Filter frequency**		**Filter gain**
	u, $[-]$	ω_f, $\left[\frac{\text{rad}}{\text{s}}\right]$	f_f, [Hz]	K_f, $\left[\frac{\text{m}^4\text{s}^2}{\text{kg}}\right]$
B	0.05, step	35.8	5.7	1.24e-11

7.4 Experiment C: Manually Tuned Parameters

Based on the results from experiment A and B, the filter parameters are manually tuned to improve the compensation system's performance. The estimated system eigenfrequency, $f_n = 2.85$ Hz estimated in subsection 5.1.3 is used in combination with frequency factors, n_ω. The experiment is divided into 3 subgroups; C1, C2 and C3. In C1 is a frequency factor of 0.5 used, in C2 is a frequency factor of 1 used and in C3 are a frequency factor of 2 used. The resulting filter frequencies and the manually tuned filter gains for the performed experiments are shown in Table C.1. Due to the number of experiments performed is only a selection of the results presented in this chapter. All results can be found in appendix C.1.

Table 7.3: Parameters of experiment C

Experiment	**Valve input**	**Filter frequency**		**Filter gain**
	u, $[-]$	ω_f, $\left[\frac{\text{rad}}{\text{s}}\right]$	f_f, [Hz]	K_f, $\left[\frac{\text{m}^4\text{s}^2}{\text{kg}}\right]$
C1.1	0.05, step	8.95	1.425	2.00e-11
C1.2	0.05, step	8.95	1.425	3.00e-11
C1.3	0.05, step	8.95	1.425	5.00e-11
C2.1	0.05, step	17.91	2.85	2.00e-11
C2.2	0.05, step	17.91	2.85	3.00e-11
C2.3	0.05, step	17.91	2.85	5.00e-11
C3.1	0.05, step	35.81	5.7	2.00e-11
C3.2	0.05, step	35.81	5.7	4.00e-11
C3.3	0.05, step	35.81	5.7	7.00e-11

7.4.1 Experiment C3.1

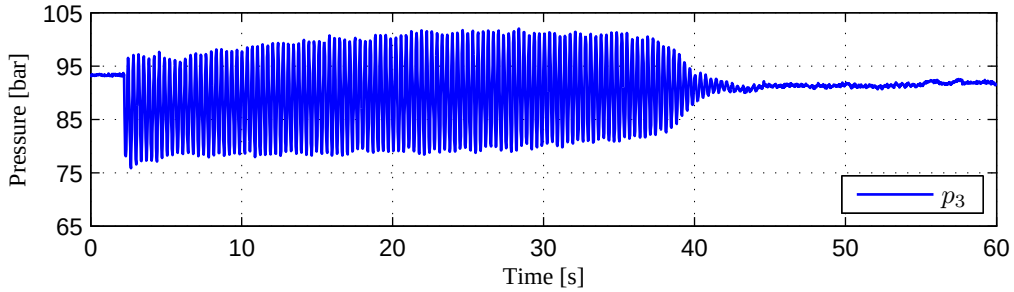

(a) Piston side cylinder chamber pressure

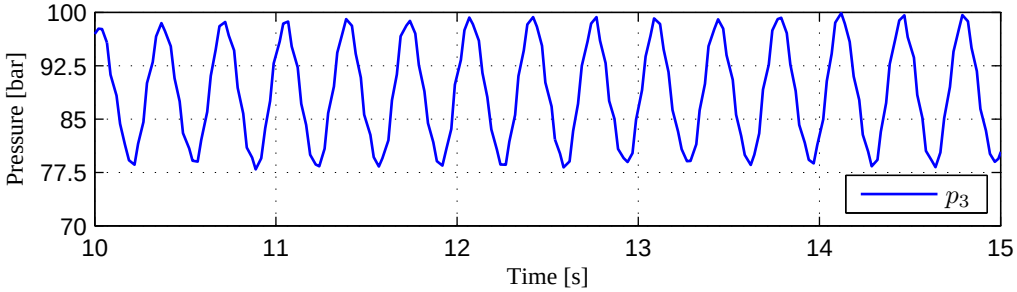

(b) Piston side cylinder chamber pressure from 10 s to 15 s

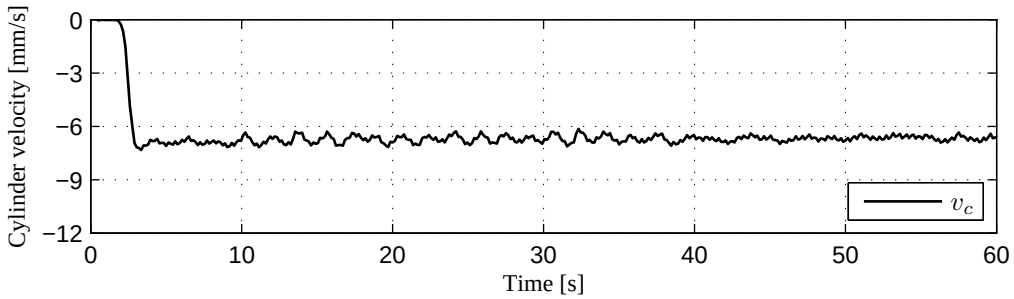

(c) Cylinder velocity

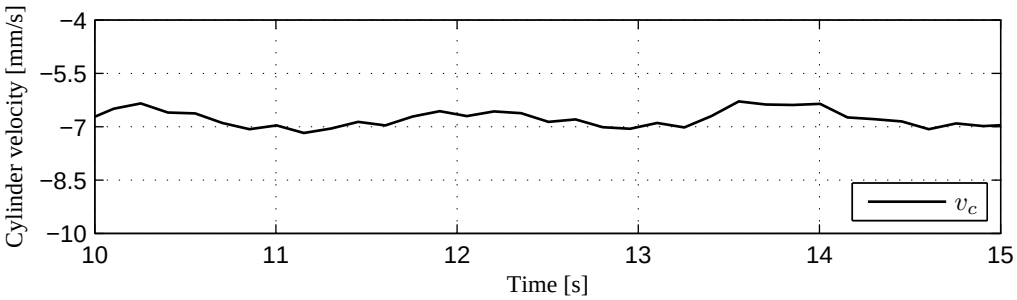

(d) Cylinder velocity from 10 s to 15 s

Figure 7.4: Piston side cylinder chamber pressure and cylinder velocity during experiment C3.1

7.4.2 Experiment C3.2

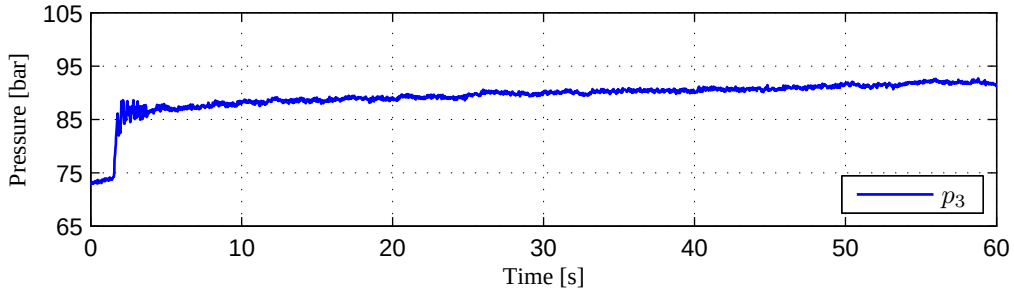

(a) Piston side cylinder chamber pressure

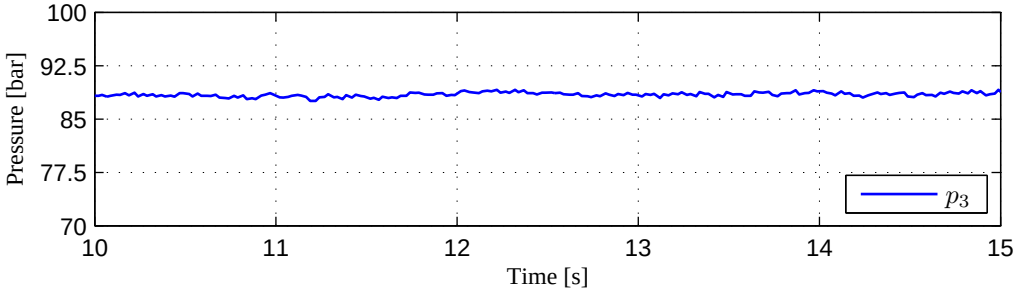

(b) Piston side cylinder chamber pressure from 10 s to 15 s

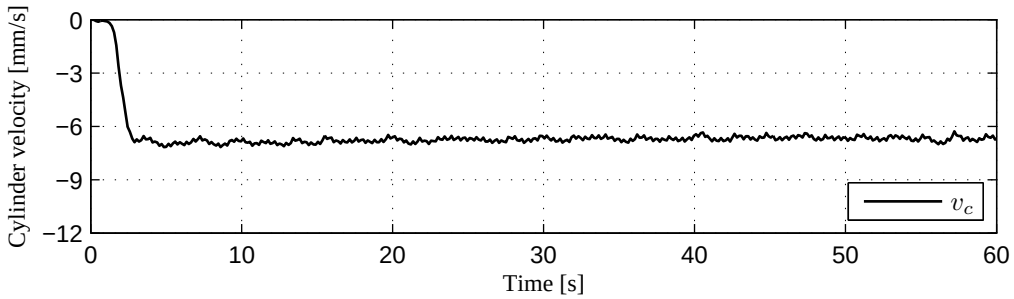

(c) Cylinder velocity

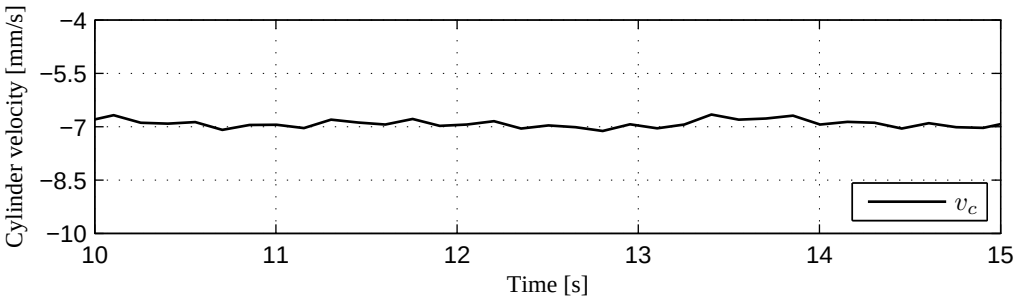

(d) Cylinder velocity from 10 s to 15 s

Figure 7.5: Piston side cylinder chamber pressure and cylinder velocity during experiment C3.2

7.4.3 Experiment C3.3

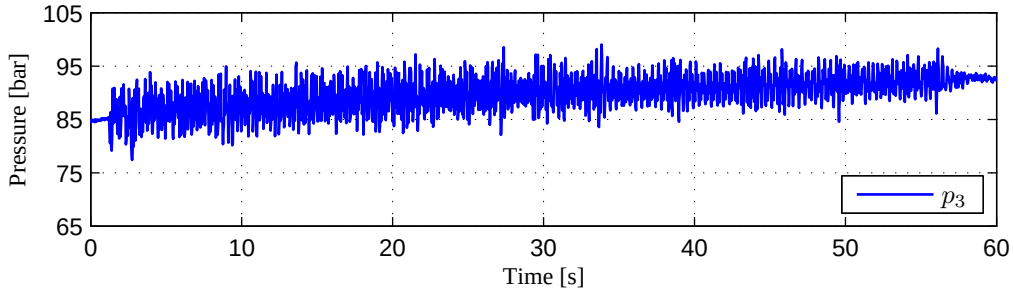

(a) Piston side cylinder chamber pressure

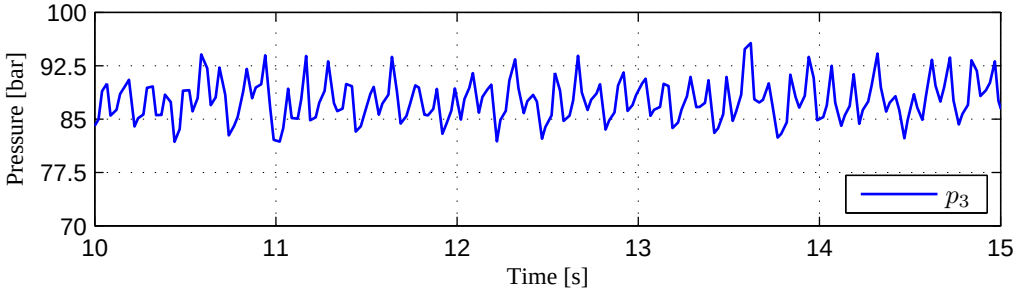

(b) Piston side cylinder chamber pressure from 10 s to 15 s

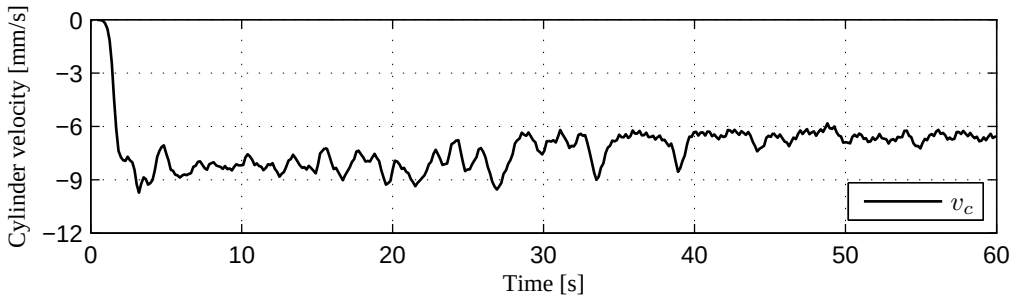

(c) Cylinder velocity

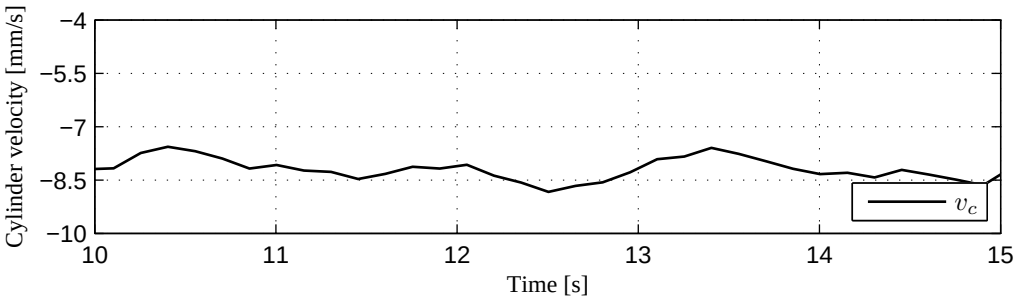

(d) Cylinder velocity from 10 s to 15 s

Figure 7.6: Piston side cylinder chamber pressure and cylinder velocity during experiment C3.3

Chapter 8

Discussion

8.1 General Result Discussion

In section 7.1 is the uncompensated system given a step input in order to show the fluctuations in the system.

Based on the performed experiments, the performance of the compensation system seems to depend more on the filter gain than the filter frequency in the range tested, which is 0.5 to 2 times the estimated eigenfrequency of the system. A gain set too low results in a compensation system not able to compensate for the fluctuations, and a gain set too high yields instability due to over-compensation. In some of the experiments performed it can be seen that the pressures are stabilized after an amount of time. The reason for this is that the cylinder stroke is decreasing. This phenomena is expected according to the stability analysis in section 2.3.

8.2 Comparison of Experiment C1.1, C2.1 and C3.2

By evaluating the pressures in the results presented in chapter 7 and appendix C.1, it can be seen that the most stable pressures are obtained in experiment C1.1, C2.1 and C3.2. The parameters of these experiments are shown in Table 8.1. Figure 8.1 and Figure 8.2 shows a comparison of the three experiments from 0 s to 5 s and 5 s to 10 s respectively. Plots of both numerical filtered and unfiltered cylinder velocities are shown due to the uncertainties of the numerical filtering.

The pressures of the three compared experiments in Figure 8.1a shows that the initial pressures prior to the step input to the valve is given are different. It is reasonable to expect less pressure oscillations the closer the initial pressure is to the steady state pressure, but this is not the case for the experiments performed. For experiment C1.1 and C3.2 the initial pressures are both less than the steady state pressure while for experiment C2.1 the initial pressure is approximately equal to the steady state pressure. It can be seen that the pressure in experiment C2.1 oscillates the most and also has the largest settling time. Experiment C1.1 and C3.2 are similar to each other, but two periods of oscillations are observed in C3.2 for every oscillation in C1.1. For the two experiments are both the oscillations and settling time less than in C2.1.

Evaluating the numerical filtered and unfiltered cylinder velocities in Figure 8.1b and Figure 8.1c reveals, as expected, that information is lost when system variations are rapid. Still, the large oscillations observed in the unfiltered velocity plots when the pressures are steady, e.g. in Figure 8.3c, are not valid. The oscillations are neither observed by visual observations during the experiments nor reasonable because of the approximately constant pressures. Based on this it is observed by the filtered velocity plots that the compensation system has very little impact on the velocity of the cylinder. This can also be validated by investigation of the compensation signal sent to the valve. In Figure 8.3 are the compensation signals for the three experiments shown. As it can be seen the compensation signals are small when the pressures are steady.

The gain in experiment C3.2 is twice of the gain in the other two compared experiments. The reason for this is that a higher filter frequency demands a higher gain because a smaller, only rapid, part of the

pressure changes are taken into account by the filter. If the filter frequency is set too low, the system may compensate for wanted pressure changes, and if set to high is may not compensate at all. The results of experiment group C3 presented in section 7.4 shows too low, appropriate and too high gains. C3.1 has a too low gain, and thereby not compensating. In C3.2 is an appropriate gain used, thus compensating. In C3.3 is a too high gain used. The gain results in a compensation to some extent, but the compensation is poor.

The gains used in the best performing experiments are relatively high compared to the parameters found for both the stiff and the simulated system. A possible reason for this is that the assumed bulk modulus, equal to 1300 MPa, is too high. The bulk modulus depends multiple factors; oil type, air solubility, temperature and pressure. Assuming a lower bulk modulus would yield higher gains.

Table 8.1: Parameters of experiment C

Experiment	**Valve input**	**Filter frequency**		**Filter gain**
	u, $[-]$	ω_f, $\left[\frac{\text{rad}}{\text{s}}\right]$	f_f, [Hz]	K_f, $\left[\frac{\text{m}^4\text{s}^2}{\text{kg}}\right]$
C1.1	0.05, step	8.95	1.425	2.00e-11
C2.1	0.05, step	17.91	2.85	2.00e-11
C3.2	0.05, step	35.81	5.7	4.00e-11

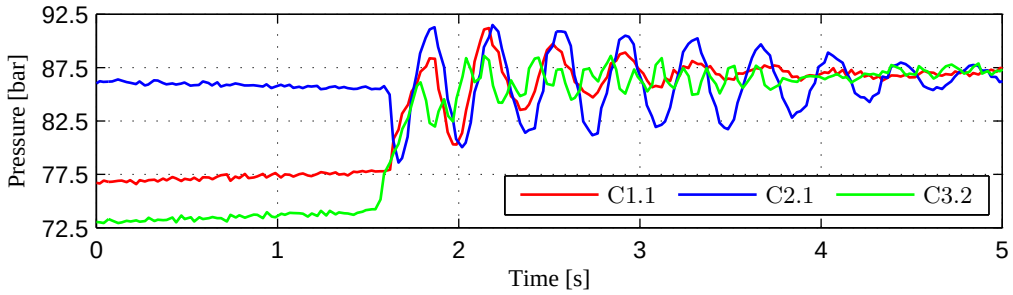

(a) Piston side cylinder chamber pressures from 0 s to 5 s

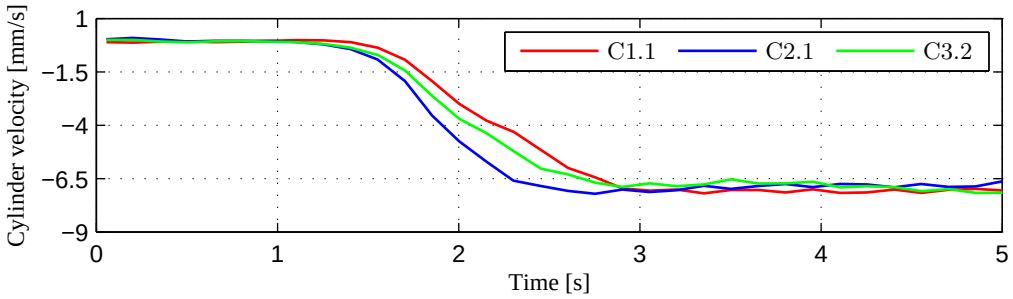

(b) Numerical filtered cylinder velocities from 0 s to 5 s

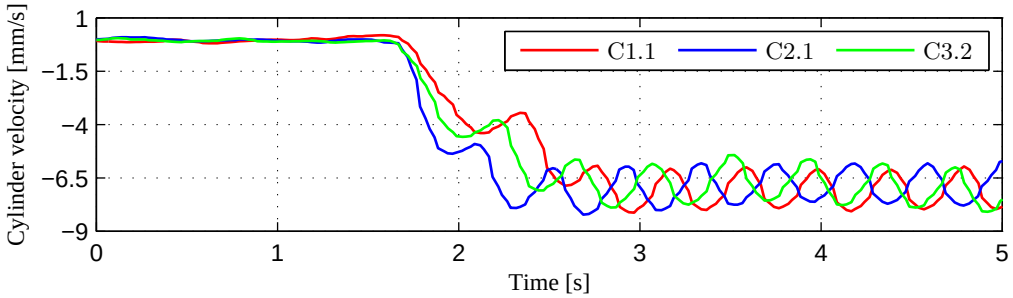

(c) Unfiltered cylinder velocities from 0 s to 5 s

Figure 8.1: Comparison of piston side cylinder chamber pressure and cylinder velocity of experiments C1.1, C2.1 and C3.2 from 0 s to 5 s

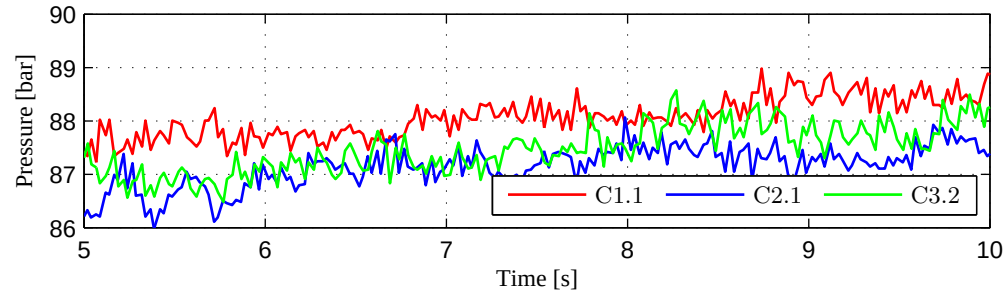

(a) Piston side cylinder chamber pressures from 5 s to 10 s

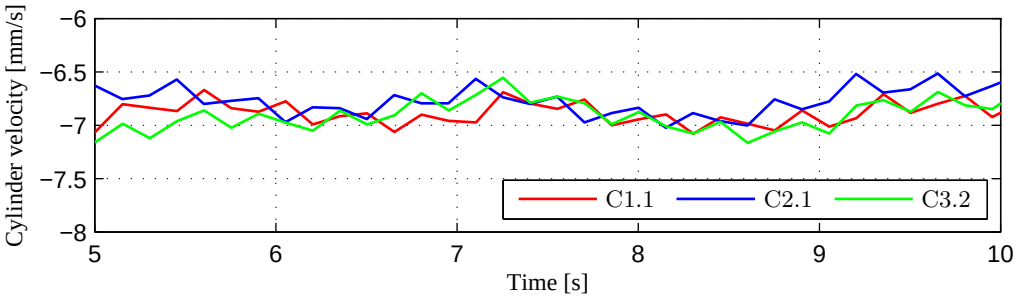

(b) Filtered cylinder velocities from 5 s to 10 s

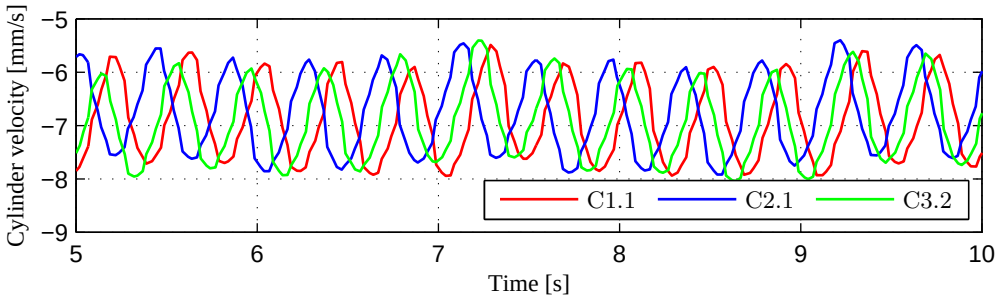

(c) Unfiltered cylinder velocities from 5 s to 10 s

Figure 8.2: Comparison of piston side cylinder chamber pressure and cylinder velocity of experiments C1.1, C2.1 and C3.2 from 5 s to 10 s

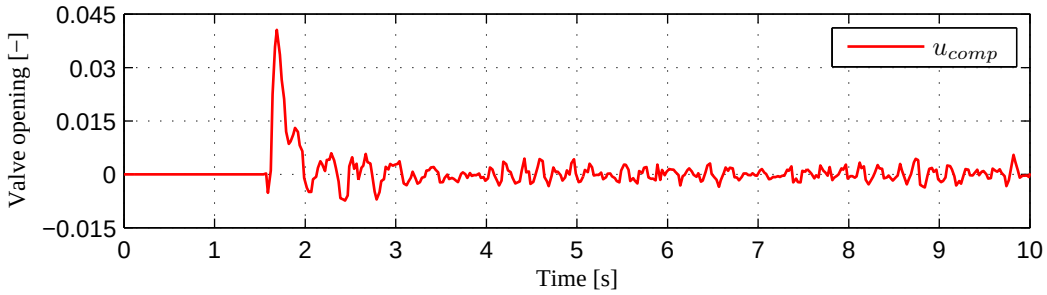

(a) Compensation signal to valve for experiment C1.1

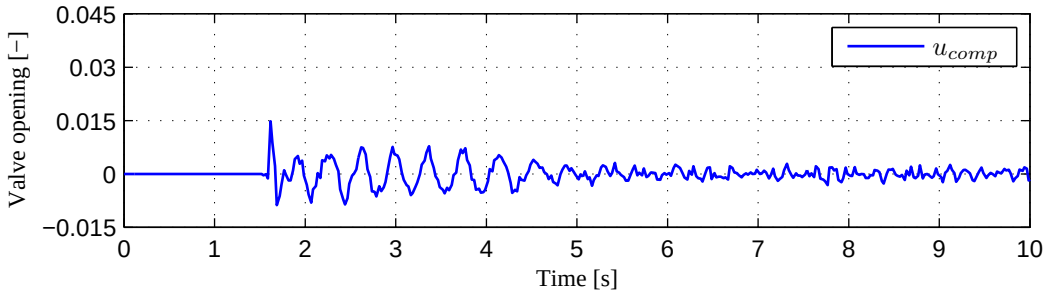

(b) Compensation signal to valve for experiment C2.1

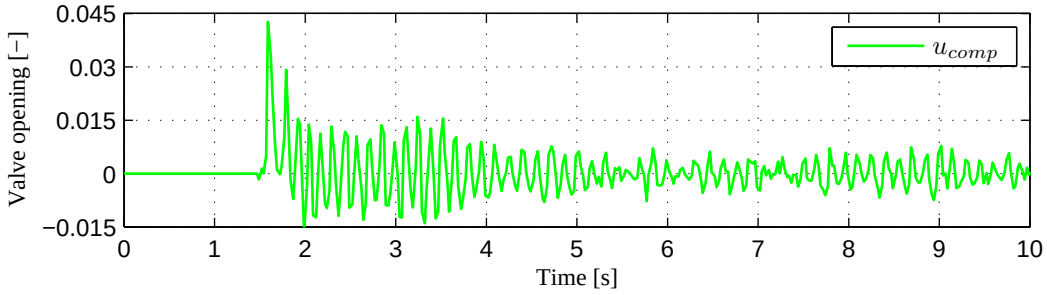

(c) Compensation signal to valve for experiment C3.2

Figure 8.3: Compensation signal to valve for experiment C1.1, C2.1 and C3.2 from 0 s to 10 s

Chapter 9

Conclusion

In this thesis a theoretical and experimental investigation of instability in a hydraulically actuated boom has been performed. Physical experiments have been performed on a test rig designed by the project supervisors. The instability, which is caused by the combination of a pressure compensated directional control valve and a counterbalance valve, has been stabilized by the use of an electronic control system. The control system uses a highpass filtered pressure feedback to control the directional control valve.

In order to obtain the parameters of the highpass filter, a stability analysis of the system has been performed. The hydraulically actuated boom has been modeled in a commercial simulation software. The simulated model has been verified by both analytical derivations and experiments performed on the experimental setup.

Parameters found theoretically and by simulations have been tested on the test rig. The performance of the control system was improved by tuning the parameters manually based on the previous mentioned experiments.

9.1 Contributions

An electronic control system which compensates for the instability caused by the combination of counterbalance valves and pressure compensated flow control has been investigated, tested and verified by physical experiments. The control system is using pressure feedback from a single sensor, which means that the implementation of the system is simple from a physical perspective and cost effective. The pressure feedback is highpass filtered so that the control system do not compensate for pressure changes that are wanted. From the experiments performed the controls system's influence on the system flow is found to be negligible.

The control system is suitable for use in many applications. Often a pressure compensated flow is desired because it eases the control of the system. Counterbalance valves are used for load holding in case of hose rupture etc. Cranes are good examples of applications where the combination is desired. The control system presented in this thesis enables this combination.

9.2 Outlook

In further work, the empahsis should be on the filter gain. Best results were performed by manual tuning of the filter gain based on experiments. The experiments performed shows that filter frequencies in the range from 0.5 to 2 times the system's eigenfrequency are appropriate. In future work investigation of the control system's robustness should also be performed.

Bibliography

[1] Michael Rygaard Hansen and Torben Ole Andersen. Controlling a negative loaded hydraulic cylinder using pressure feedback. In *29th IASTED International Conference on Modelling, Identification and Control, MIC 2010*, pages 242–248.

[2] James M. Gere and Barry J. Goodno. *Mechanics of Materials*. Cengage Learning, 7th edition, 2009.

[3] Carl M. Larsen. *Marin dynamikk*. 2009. In Norwegian.

[4] Morten Ottestad, Nicolai Nilsen, and Michael Rygaard Hansen. Reducing the static friction in hydraulic cylinders by maintaining relative velocity between piston and cylinder. In *12th International Conference on Control, Automation and Systems (ICCAS)*, 2012.

[5] Morten K. Bak and Michael R. Hansen. Analysis of offshore knuckle boom crane - part one: Modeling and parameter identification. *Modeling, Identification and Control*, 34(4):157–174, 2013.

[6] Roland S. Burns. *Advaced Control Engineering*. Butterworth-Heinemann, 2001.

List of Figures

List of Tables

Appendices

Appendix A

Project Description

11. Experimental and Theoretical Investigation of Instability in Hydraulically Actuated Boom

Background

In load carrying applications, counterbalance valves play an important safety role; among the properties are leak tight holding, load holding at pipe burst, and to ensure no drop occurs before lift. It is, however, well known that they tend to introduce instability in a system, especially when the flow supply is pressure compensated. This is the case when the directional control valve that supplies flow to the actuator suspended by the counterbalance valve is equipped with an internal compensator in series with the main spool; a so-called flow control valve or pressure compensated valve. One of the major challenges within hydraulics is to design pressure compensated systems containing counterbalance valves that offer stable handling of negative loads without unnecessarily compromising system efficiency and response.

An experimental arm has been designed and is equipped with a hydraulic system that will introduce instability, see figure.

Goals

The main goal of the project is to investigate a novel method of stabilizing pressure compensated systems containing counterbalance valves and, simultaneously, to develop and investigate alternative methods based on closed loop control.

Content:

The project includes:

- The test rig instrumentation in such a way that all relevant properties can be measured.
- Measurement program development in Labview, so that the test rig can be controlled and data can be logged using an NI CompactRIO.
- Theoretical study of instability in investigated system.
- Test rig should be modeling using SimX and experimental verification.
- Implementation and testing of the proposed method for dealing with instability.

- Development, implementation and testing of alternative methods for dealing with instability using experimental setup and developed SimX model.

Disciplines
Instrumentation of a hydraulic experimental rig, experimental work; control of hydraulic valves and data logging (Labview), mechanical and hydraulic system modeling (SimX), system stability, and closed loop control.

Contact persons:
Michael R. Hansen, michael.r.hansen@uia.no
Jesper K. Sørensen, jesper.k.sorensen@uia.no

Appendix B

Analytical and Simulated Results

B.1 Comparison of Analytically Derived and Simulated Kinematics and Kinetics

The following figures shows comparisons of the analytic and simulated kinematics and kinetics. As seen in the figures are there no deviations between the analytic and the simulated model.

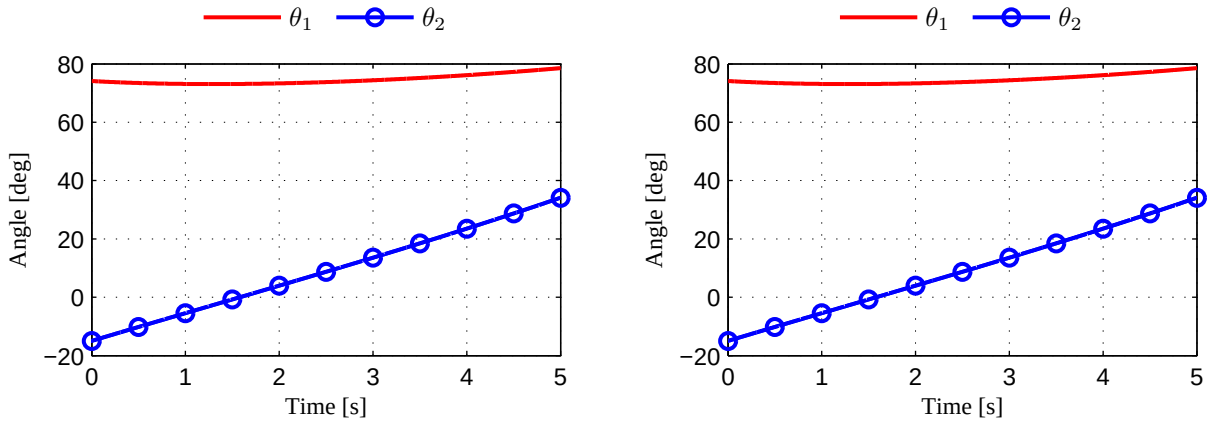

(a) Analytically derived (b) Simulated

Figure B.1: Plots of analytically derived and simulated angles

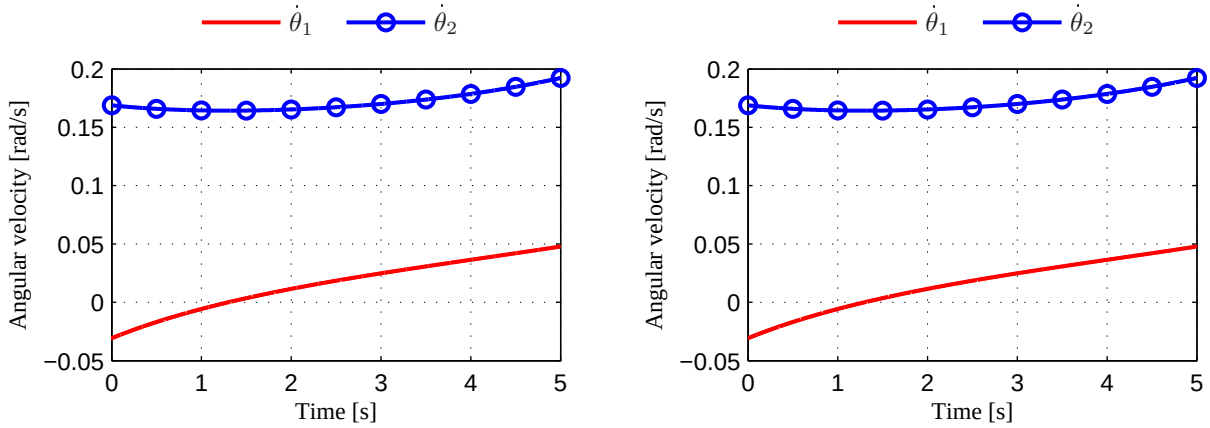

(a) Analytically derived (b) Simulated

Figure B.2: Plots of analytically derived and simulated angular velocities

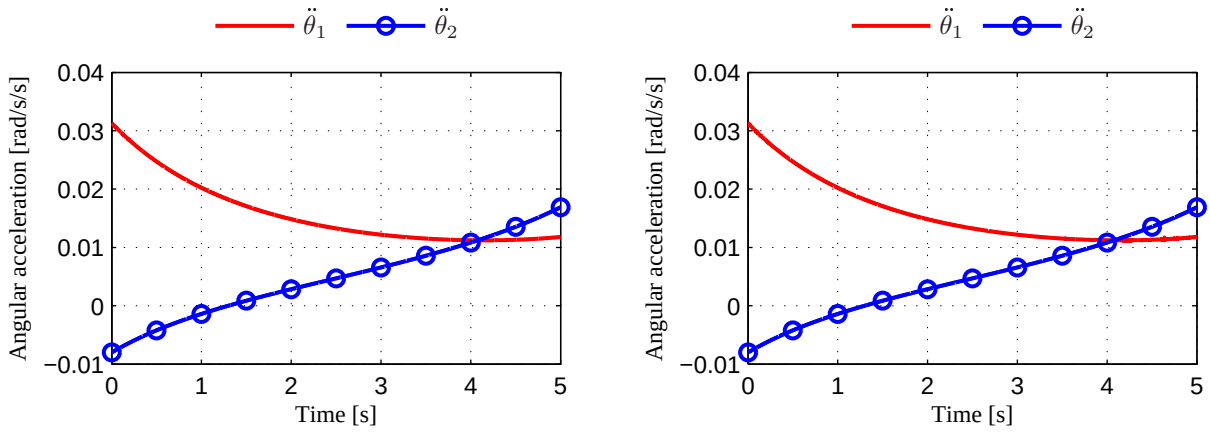

(a) Analytically derived (b) Simulated

Figure B.3: Plots of analytically derived and simulated angular acceleration

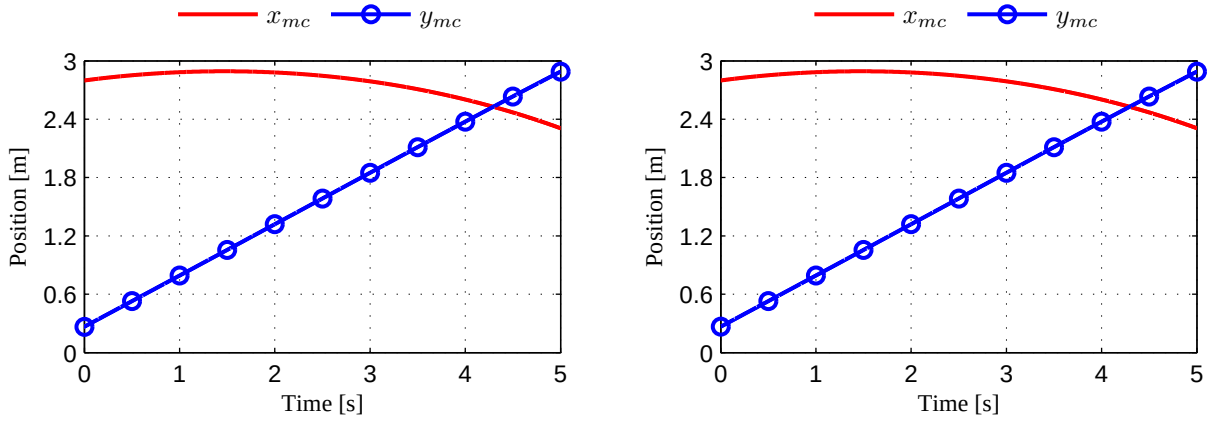

(a) Analytically derived (b) Simulated

Figure B.4: Plots of analytically derived and simulated mass center position

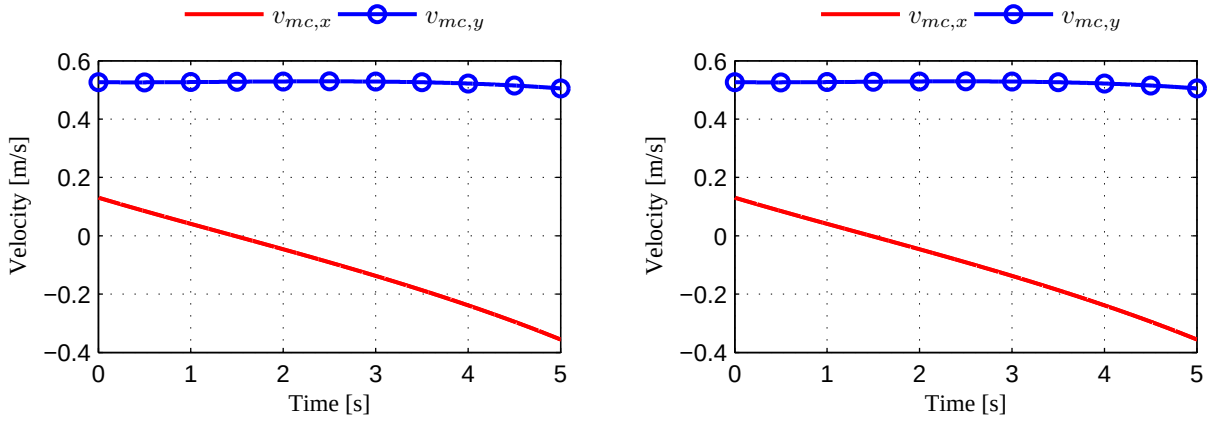

(a) Analytically derived (b) Simulated

Figure B.5: Plots of analytically derived and simulated mass center velocity

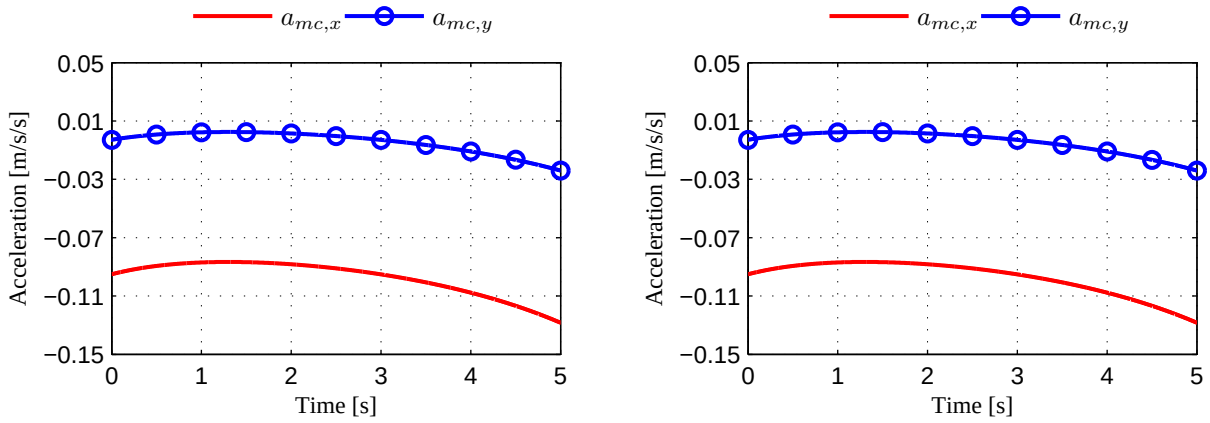

(a) Analytically derived (b) Simulated

Figure B.6: Plots of analytically derived and simulated mass center acceleration

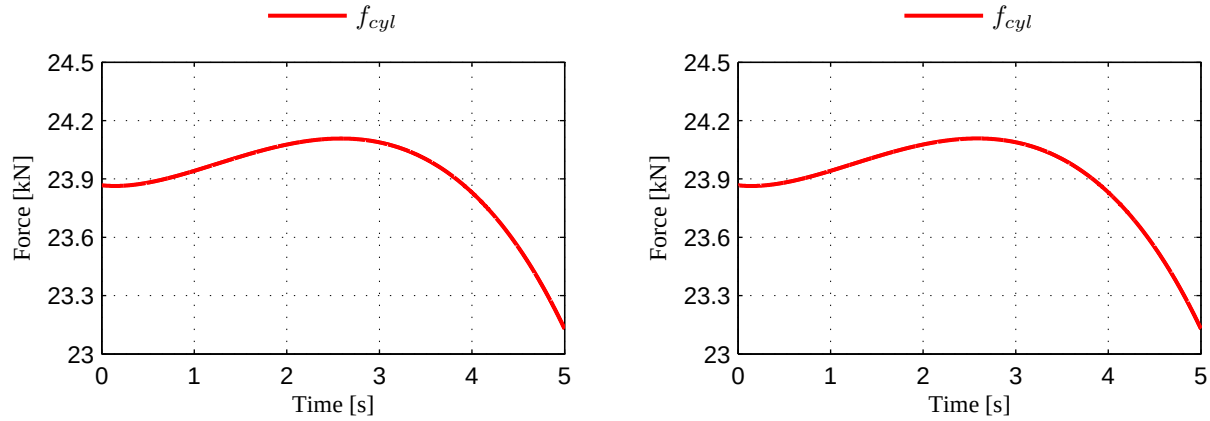

(a) Analytically derived (b) Simulated

Figure B.7: Plots of analytically derived and simulated cylinder force

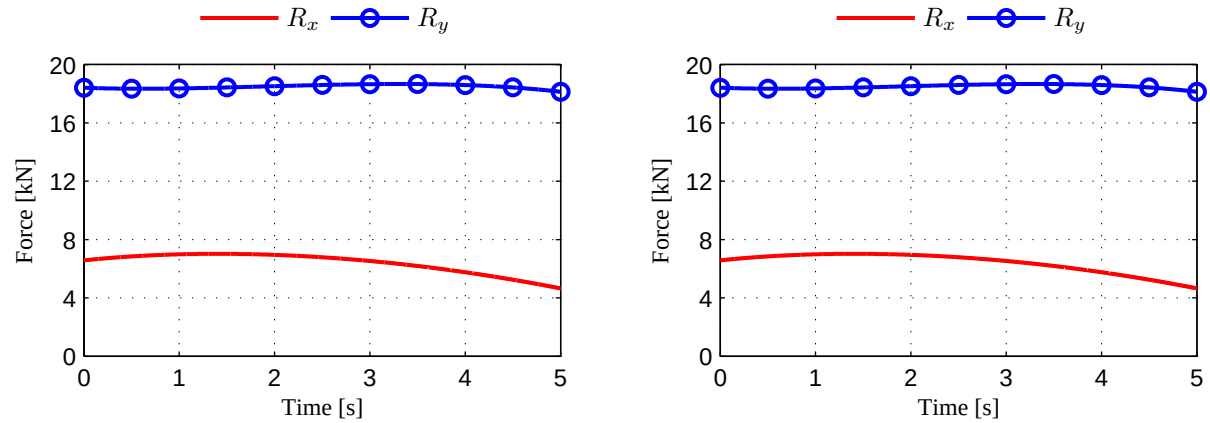

(a) Analytically derived (b) Simulated

Figure B.8: Plots of analytically derived and simulated main joint reaction forces

Appendix C

Experimental Results

C.1 Expt. C: Manually Tuned Parameters

C.1.1 Experiment C parameters

Table C.1: Parameters of experiment C

Experiment	**Valve input**	**Filter frequency**		**Filter gain**
	u, $[-]$	ω_f, $\left[\frac{\text{rad}}{\text{s}}\right]$	f_f, [Hz]	K_f, $\left[\frac{\text{m}^4\text{s}^2}{\text{kg}}\right]$
C1.1	0.05, step	8.95	1.425	2.00e-11
C1.2	0.05, step	8.95	1.425	3.00e-11
C1.3	0.05, step	8.95	1.425	5.00e-11
C2.1	0.05, step	17.91	2.85	2.00e-11
C2.2	0.05, step	17.91	2.85	3.00e-11
C2.3	0.05, step	17.91	2.85	5.00e-11
C3.1	0.05, step	35.81	5.7	2.00e-11
C3.2	0.05, step	35.81	5.7	4.00e-11
C3.3	0.05, step	35.81	5.7	7.00e-11

C.1.2 Experiment C1.1

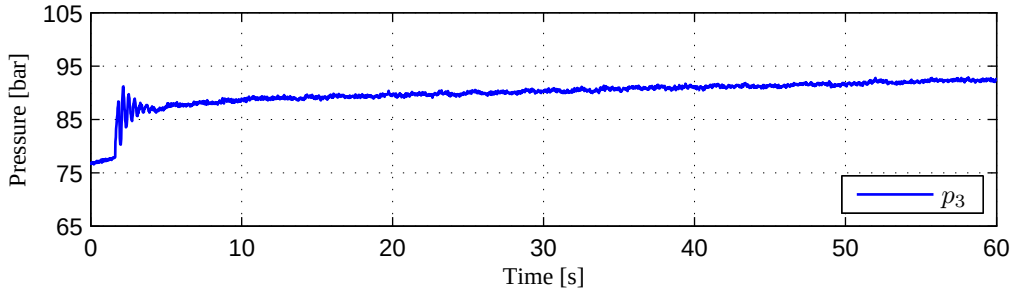

(a) Piston side cylinder chamber pressure

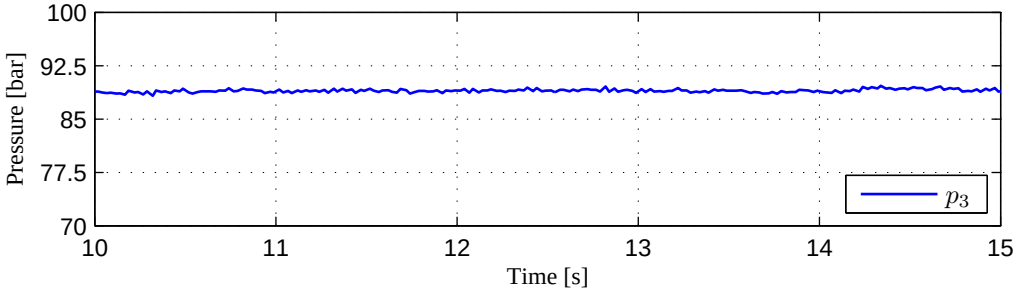

(b) Piston side cylinder chamber pressure from 10 s to 15 s

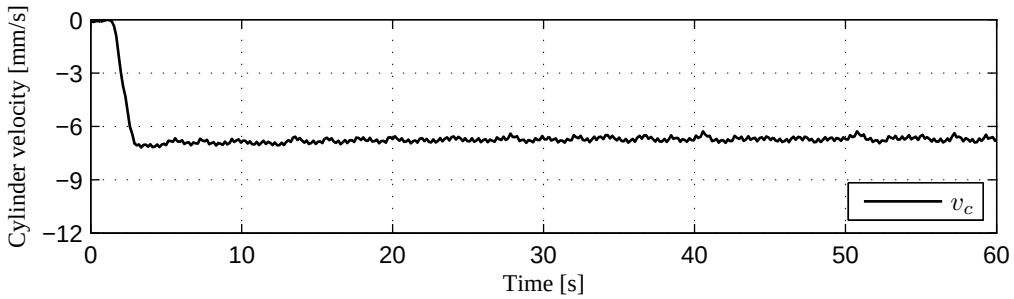

(c) Cylinder velocity

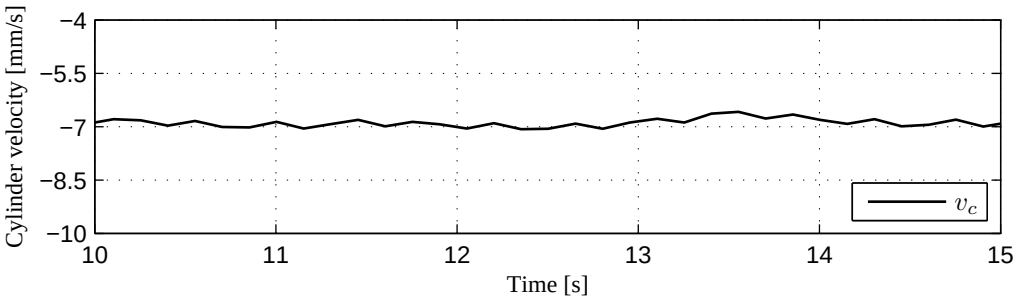

(d) Cylinder velocity from 10 s to 15 s

Figure C.1: Piston side cylinder chamber pressure and cylinder velocity during experiment C1.1

C.1.3 Experiment C1.2

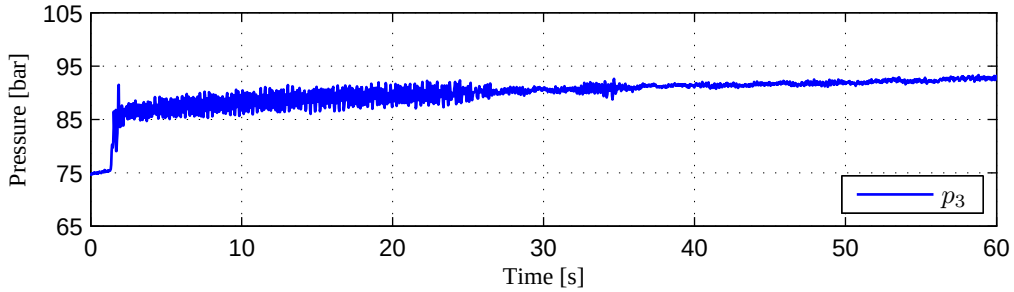

(a) Piston side cylinder chamber pressure

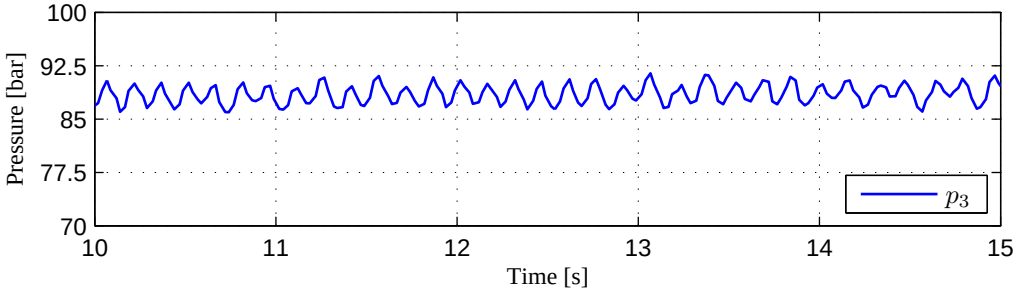

(b) Piston side cylinder chamber pressure from 10 s to 15 s

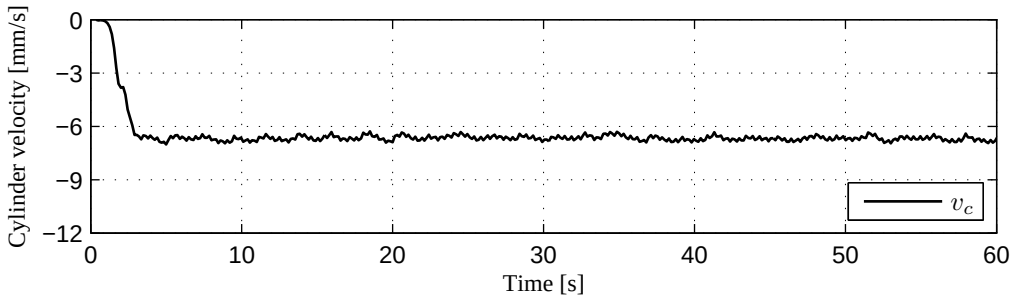

(c) Cylinder velocity

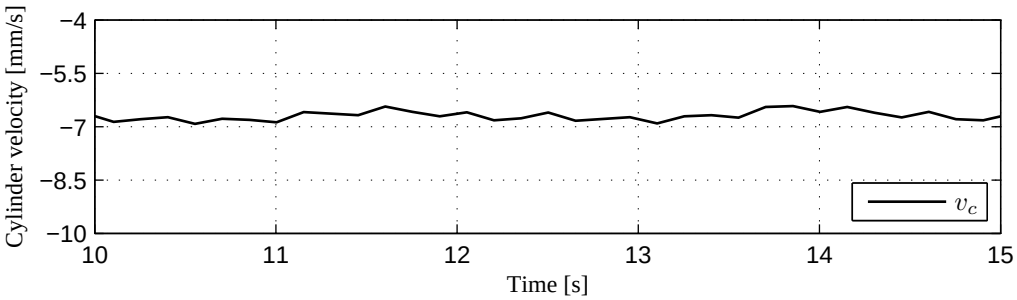

(d) Cylinder velocity from 10 s to 15 s

Figure C.2: Piston side cylinder chamber pressure and cylinder velocity during experiment C1.2

C.1.4 Experiment C1.3

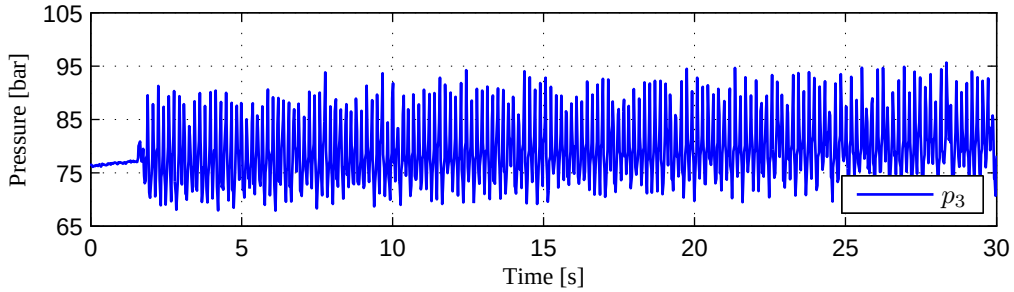

(a) Piston side cylinder chamber pressure

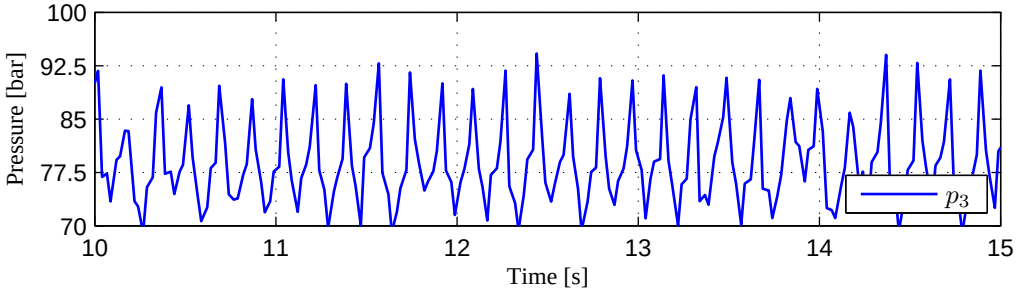

(b) Piston side cylinder chamber pressure from 10 s to 15 s

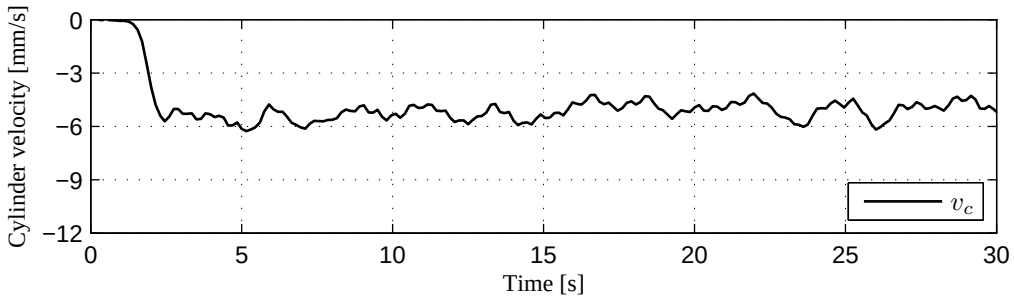

(c) Cylinder velocity

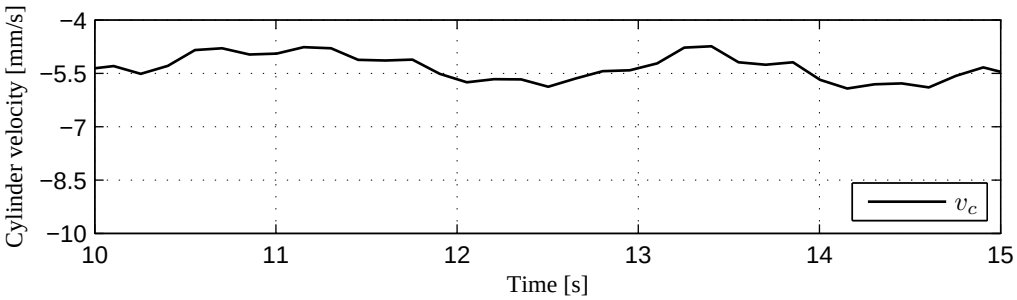

(d) Cylinder velocity from 10 s to 15 s

Figure C.3: Piston side cylinder chamber pressure and cylinder velocity during experiment C1.3

C.1.5 Experiment C2.1

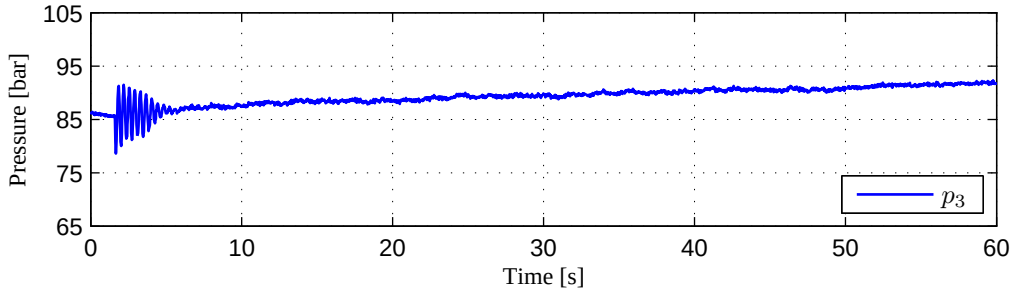

(a) Piston side cylinder chamber pressure

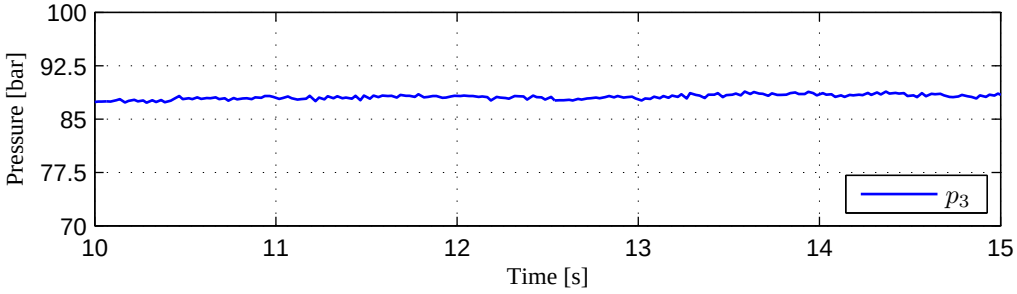

(b) Piston side cylinder chamber pressure from 10 s to 15 s

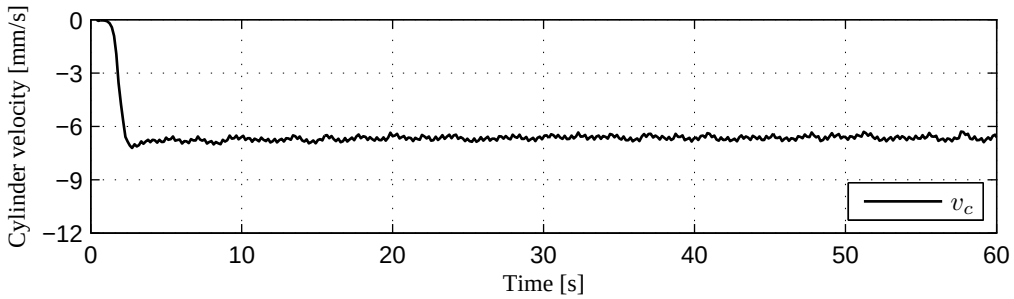

(c) Cylinder velocity

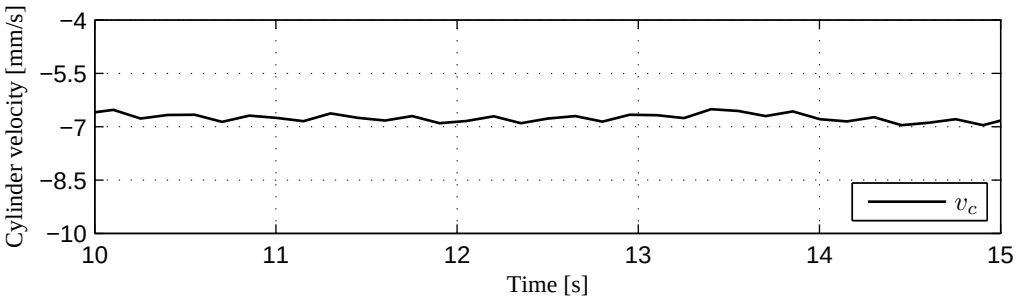

(d) Cylinder velocity from 10 s to 15 s

Figure C.4: Piston side cylinder chamber pressure and cylinder velocity during experiment C2.1

C.1.6 Experiment C2.2

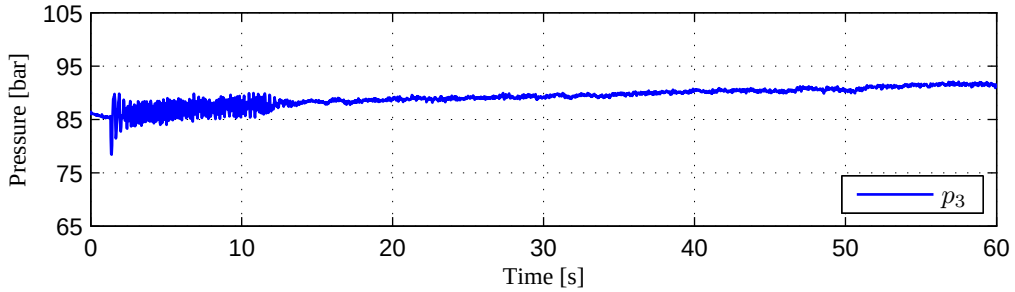

(a) Piston side cylinder chamber pressure

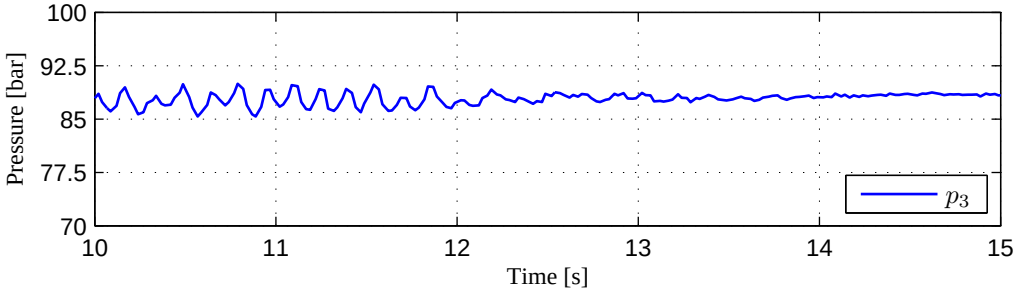

(b) Piston side cylinder chamber pressure from 10 s to 15 s

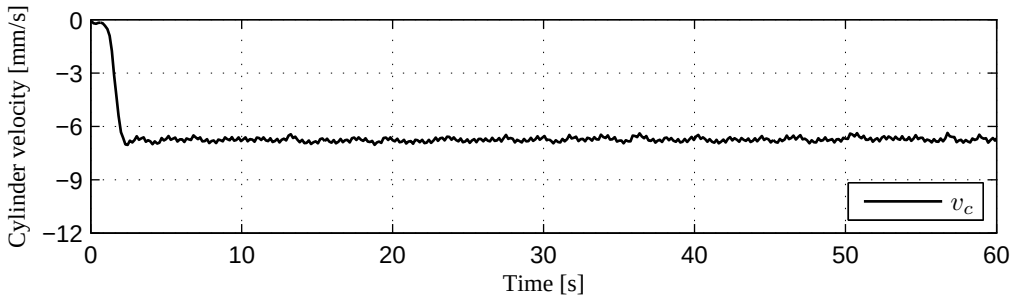

(c) Cylinder velocity

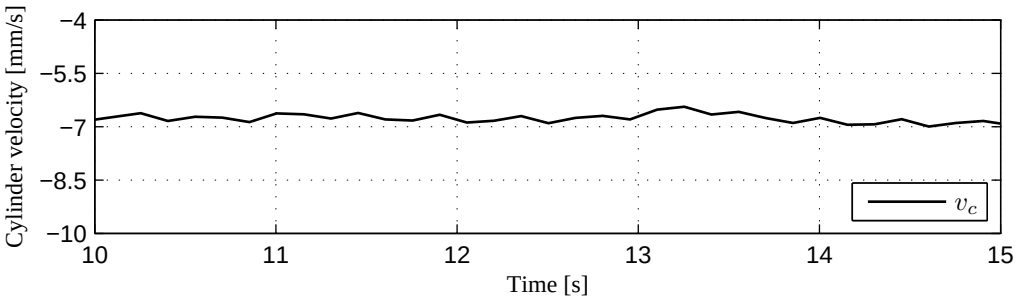

(d) Cylinder velocity from 10 s to 15 s

Figure C.5: Piston side cylinder chamber pressure and cylinder velocity during experiment C2.2

C.1.7 Experiment C2.3

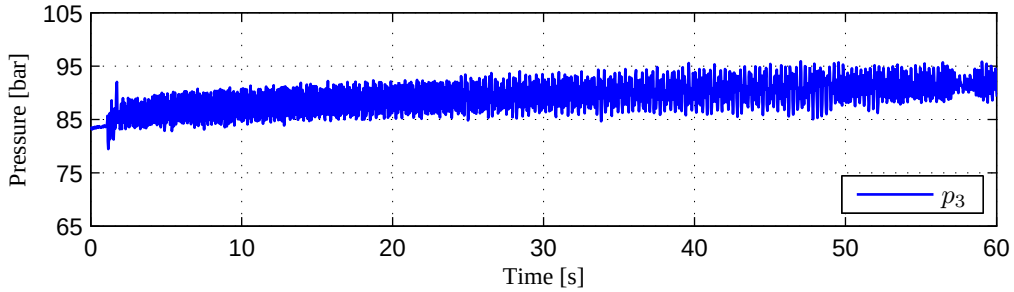

(a) Piston side cylinder chamber pressure

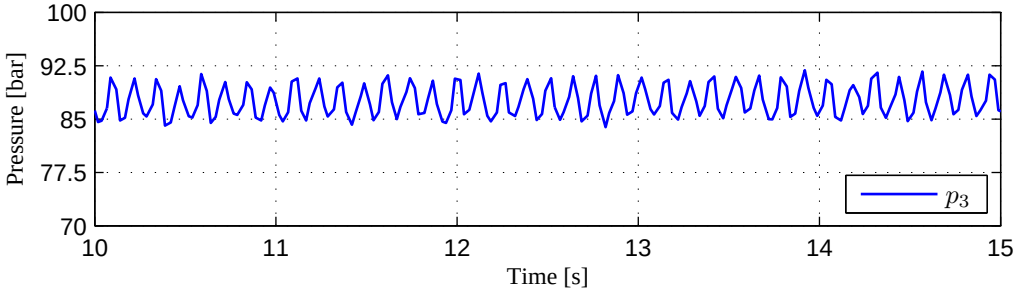

(b) Piston side cylinder chamber pressure from 10 s to 15 s

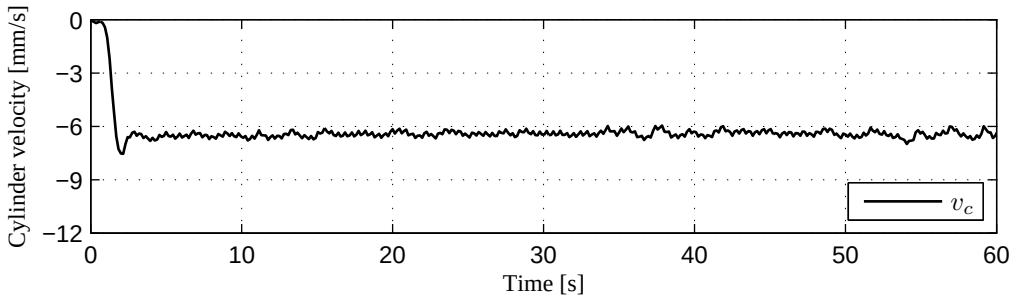

(c) Cylinder velocity

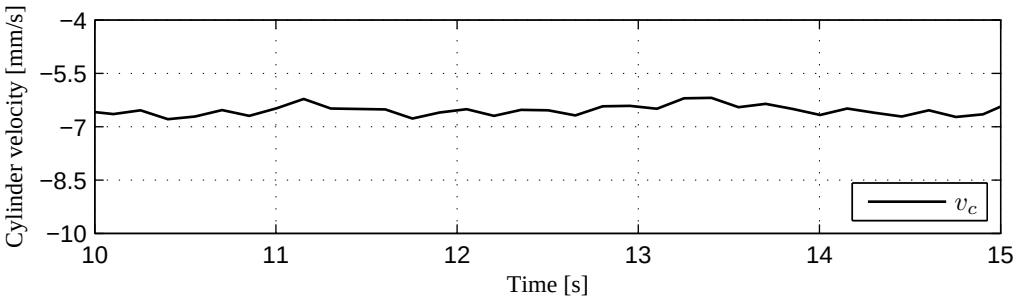

(d) Cylinder velocity from 10 s to 15 s

Figure C.6: Piston side cylinder chamber pressure and cylinder velocity during experiment C2.3

C.1.8 Experiment C3.1

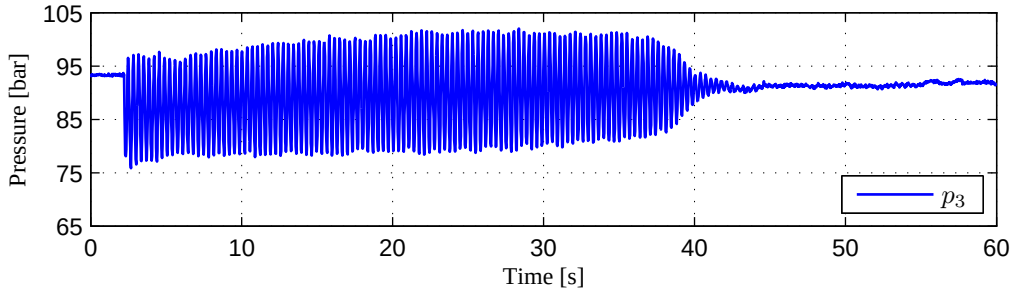

(a) Piston side cylinder chamber pressure

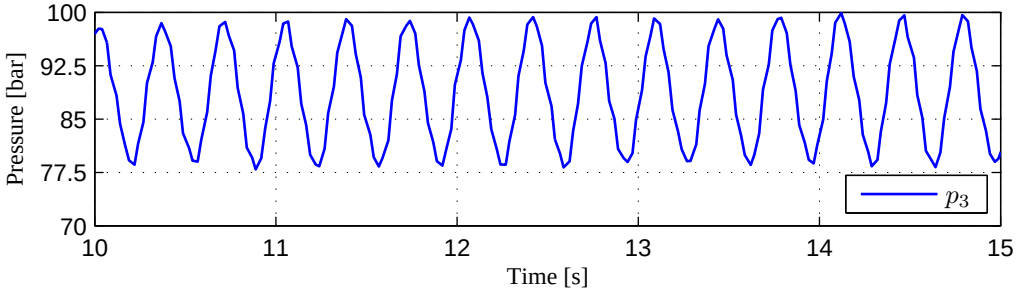

(b) Piston side cylinder chamber pressure from 10 s to 15 s

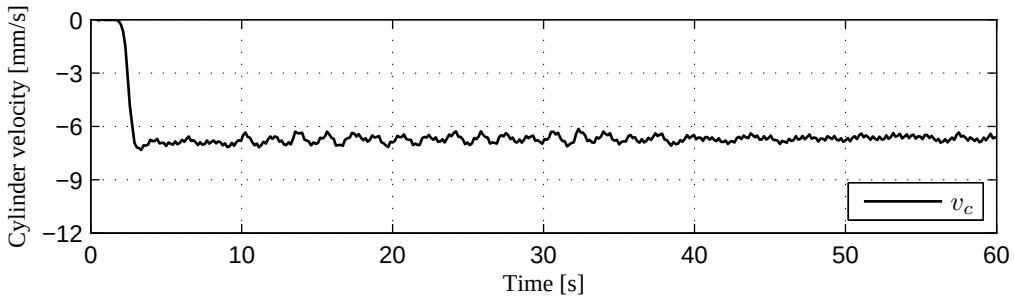

(c) Cylinder velocity

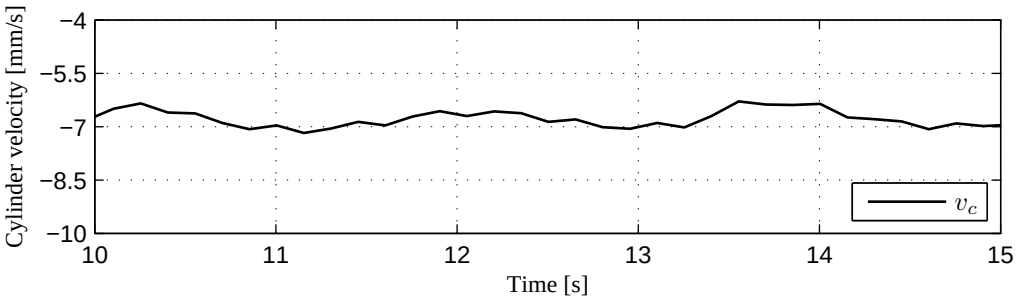

(d) Cylinder velocity from 10 s to 15 s

Figure C.7: Piston side cylinder chamber pressure and cylinder velocity during experiment C3.1

C.1.9 Experiment C3.2

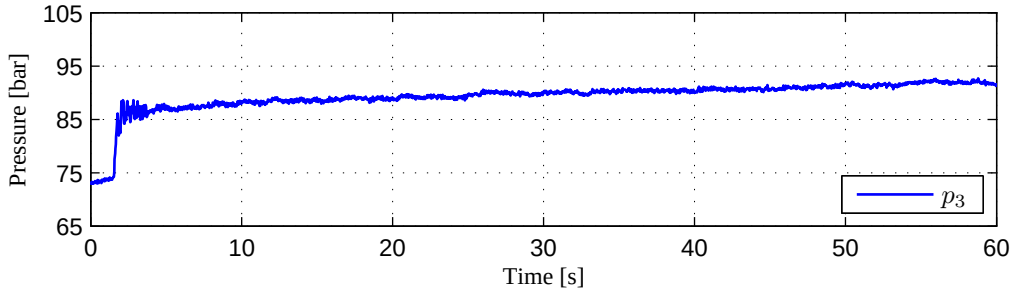

(a) Piston side cylinder chamber pressure

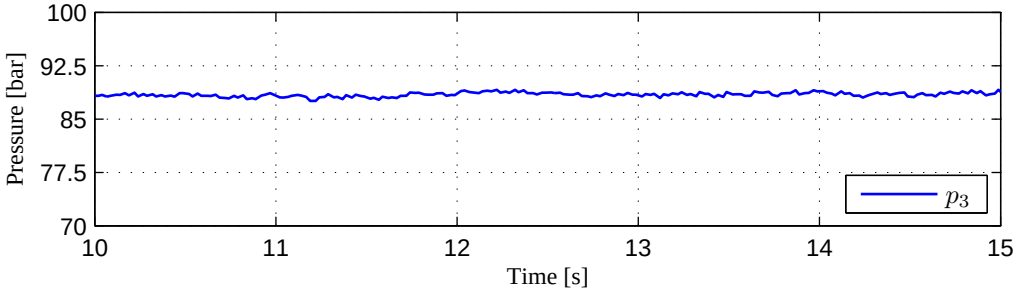

(b) Piston side cylinder chamber pressure from 10 s to 15 s

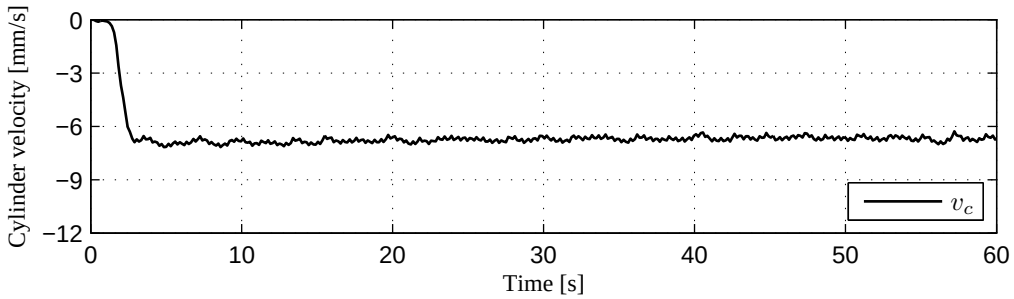

(c) Cylinder velocity

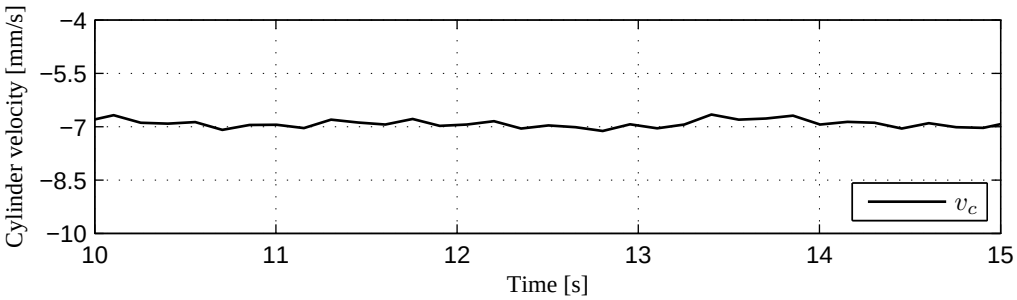

(d) Cylinder velocity from 10 s to 15 s

Figure C.8: Piston side cylinder chamber pressure and cylinder velocity during experiment C3.2

C.1.10 Experiment C3.3

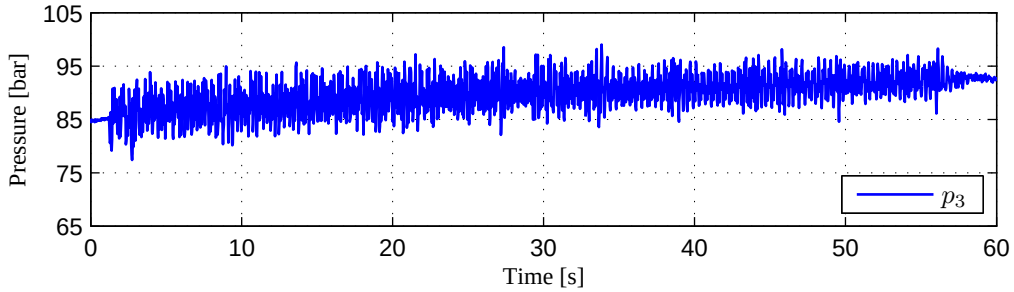

(a) Piston side cylinder chamber pressure

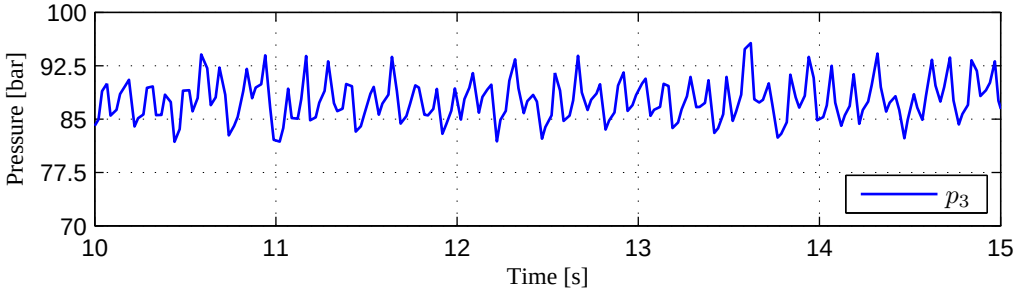

(b) Piston side cylinder chamber pressure from 10 s to 15 s

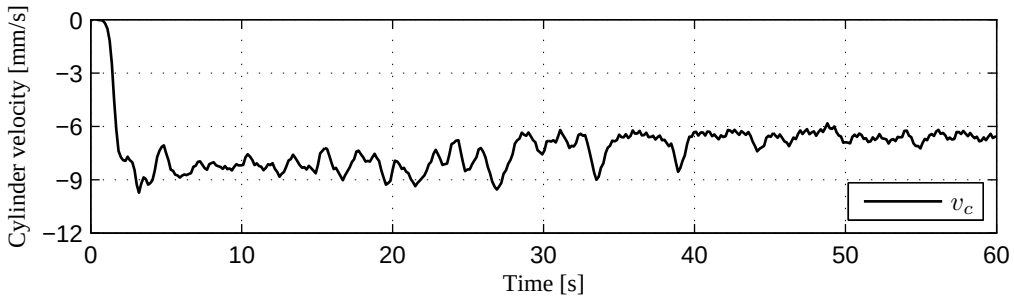

(c) Cylinder velocity

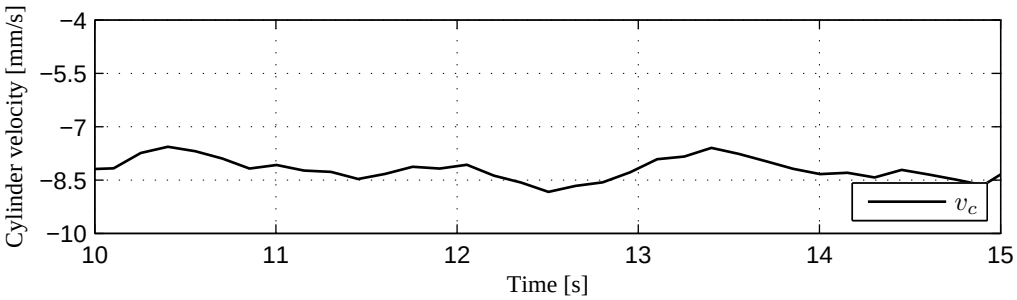

(d) Cylinder velocity from 10 s to 15 s

Figure C.9: Piston side cylinder chamber pressure and cylinder velocity during experiment C3.3

Appendix D

Components

D.1 Data Sheets

Table D.1 lists the URLs to the datasheets for the components used in the project. In appendix D.2 is the complete order list for the DCVs shown.

Table D.1: URLs to datasheets for components used

Component	Manufactor	Type
DCV	Danfoss	PVG32
http://files.danfoss.com/documents/520l0344.pdf		
PVE	Danfoss	PVES
http://files.danfoss.com/documents/520l0553.pdf		
CBV	Sun Hydraulics	CWCK LHN 1:1
http://www.sunhydraulics.com/model/CWCK/LHN		
CBV	Sun Hydraulics	CWCL LFN 2:1
http://www.sunhydraulics.com/model/CWCL/LFN		
CBV	Sun Hydraulics	CWCA LHN 3:1
http://www.sunhydraulics.com/model/CWCA/LHN		
CBV	Sun Hydraulics	CWCG LFN 5:1
http://www.sunhydraulics.com/model/CWCG/LFN		
Hose	Manuli Hydraulics	ROCKMASTER/2SN
http://www.manuli-hydraulics.com/multimedia/literature/product-guide.pdf		
Cylinder	PMC Cylinders	25CA
http://www.pmcgroup.se/PageFiles/6093/25CA_Broschyr_20_sid.pdf?epslanguage=ru		
Cylinder position sensor	Regal	PS6310
http://regal.se/data/prodfile/PS6300_en.pdf		
Pressure sensor	Parker	SCP-400-44-07
http://www.parker.com/literature/Tube%20Fittings%20Division%20Europe/New/CAT-4054-3-UK.pdf		
Flow meter	Parker	SCQ-150
http://www.parker.com/literature/Tube%20Fittings%20Division%20Europe/New/CAT-4054-3-UK.pdf		
Strain gauge	TML	FLA-10-11
http://www.tml.jp/e/product/strain_gauge/gauge_list/f_list.html		

D.2 Directional Control Valve Order List

,

SAUER DANFOSS

PVG 32 Proportional Valve Group
Technical Information
Order Specification

Order Specification Forms

Subsidiary/Dealer					PVG No.				
Customer					Customer Part No.				
Application					Revision No.				
Section v	Function	A-Port v						B-Port v	
0			157B	157B 5011 p = 250	bar	157B			
1		a 157B 3171 b 157B 2265		157B 6130 LS_A	bar	157B 9751 LS_B	16 bar	11108994 157B 2265	c b
2		a 157B 3171 b 157B 2265		157B 6233 LS_A 200	bar	157B 9771 LS_B 200	16 bar	11108994 157B 2265	c b
3		a 157B 3171 b 157B 2265		157B 6233 LS_A 200	bar	157B 9781 LS_B 200	16 bar	11108994 157B 2265	c b
4		a 157B 3171 b 157B 2265		157B 6233 LS_A 200	bar	157B 7031 LS_B 200	16 bar	11108994 157B 2265	c b
5		a 157B b 157B		157B LS_A	bar	157B LS_B	16 bar	157B 157B	c b
6		a 157B b 157B		157B LS_A	bar	157B LS_B	16 bar	157B 157B	c b
7		a 157B b 157B		157B LS_A	bar	157B LS_B	16 bar	157B 157B	c b
8		a 157B b 157B		157B LS_A	bar	157B LS_B	16 bar	157B 157B	c b
9		a 157B b 157B		157B LS_A	bar	157B LS_B	16 bar	157B 157B	c b
10		a 157B b 157B		157B LS_A	bar	157B LS_B	16 bar	157B 157B	c b
11		a 157B b 157B		157B LS_A	bar	157B LS_B	16 bar	157B 157B	c b
12		a 157B b 157B 157B		157B LS_A	bar	157B LS_B	16 bar	157B 157B 157B	c b
13		a 157B b 157B		157B LS_A	bar	157B LS_B	16 bar	157B 157B	c b
14	End section			157B 2000					
15	PVAS section			157B 8004					
	"Reserved for Painting"			157B					
	Comments:								
	Filled in by:							Date:	

Separate specification pads are available under the literature no. **520L0515**.

D.3 Electric Diagram

,